Application of Bioimage Informatics to Quantification of Focal Adhesions and Invadopodia

Matthew E. Berginski

A dissertation submitted to the faculty of the University of North Carolina at Chapel Hill in partial fulfillment of the requirements for the degree of Doctor of Philosophy in the Department of Biomedical Engineering.

Chapel Hill
2013

Approved by:

Shawn M. Gomez, Eng.Sc.D.

James E. Bear, Ph.D.

Anne M. Taylor, Ph.D.

Glenn M. Walker, Ph.D.

Marc Niethammer, Ph.D.

Abstract

MATTHEW E. BERGINSKI: Application of Bioimage Informatics to Quantification of Focal Adhesions and Invadopodia.
(Under the direction of Shawn M. Gomez, Eng.Sc.D..)

The development of the ability to fluorescently label functional proteins and visualize their subcellular localization using microscopy in living cells, has made it possible to study a wide range of single cell phenomena. To understand the results of imaging assays, cell biologists have used manual methods for determining the quantitative properties of the cellular structures visualized fluorescent microscopy. As the quantity and complexity of the images that can be collected using fluorescence microscopy has increased, a new subfield of Bioinformatics has developed, named Bioimage Informatics, which specializes in adapting and developing new methods to quantify the image sets resulting from biological assays.

In this thesis, I describe the application and development of Bioimage Informatic methods to the analysis of Focal Adhesions and Invadopodia. Focal Adhesions are subcellular protein complexes, whose role include acting as the points of contact for cellular motility and sensing the outside environment. Focal Adhesions have traditionally been analyzed using manual methods, which has limited the number of Focal Adhesions that could be analyzed and the depth of properties that could be collected. I have developed a set of methods which can identify, track and quantify Focal Adhesion properties from live cell image sets. This Focal Adhesion analysis framework has been expanded to include spatial and global methods for describing Focal Adhesion morphology. I have also developed a system for quantifying Invadopodia properties. Invadopodia are subcellular protein complexes present in metastatic cancer cells, which actively degrade the extracellular matrix, allowing migration of cancer cells away from primary tumors. This analysis system has two parts, one which can follow single Invadopodia and assess their properties and a complementary component which assesses degradation behavior in cell populations.

Acknowledgments

This work would not have been possible without the support of my adviser, Shawn Gomez. His door has always been open when I needed to discuss this work and he has always provided advice when I've needed it. I can also thank Shawn for introducing me to Eric Vitriol and Klaus Hahn who saw the need for methods quantify Focal Adhesions. I can also thank Eric for introducing my work to Jim Bear, who provided me the opportunity to continue to develop the Focal Adhesion analysis methods and work in his lab. I am would also like to thank the rest of my committee, Anne Taylor, Glenn Walker and Marc Niethammer, for their feedback and advice. I would also like to acknowledge the Bioinformatics training grant, the UCRF fund and the NSF Graduate Research Fellows Program for providing funding.

I would also like to thank the members of the Gomez lab, Kwangbom Choi, Jen Staab, Alicia Midland, Janet Doolittle, Ke Xu, Dan Oreper and Kyla Lutz who have provided valuable feedback about my work. The members of the Bear lab, David Roadcap, Sarah Creed, Shelly Cochran, Keefe Chan, Emma Wu and Sreeja Asokan, also provided many hours of training and feedback in the lab. My fellow students in the Bioinformatics training program have also played an important role in my development as a scientist.

Finally, I am grateful to my family and friends who have supported me throughout my graduate career. My mom, dad and sister have always had belief in me and supported my academic goals. The friends I've made at UNC have helped me through the difficult times and helped me celebrate the victories. To my wife Alli, I am incredibly thankful for her continuous support and love. To my daughter Madeleine, you have brightened my days and I look forward to watching you grow up.

Table of Contents

List of Figures

Chapter 1

Introduction

Visualizating the location of proteins in living cells, through fluorescence microscopy, has become a critical method for investigating the function and activity of individual proteins and protein complexes at the single cell level [1, 2]. The development of these methods and the related advancements in imaging hardware has expanded the type of imaging studies that can be conducted, but has raised problems related to drawing conclusions from the image sets produced. Traditionally, quantitative properties have been extracted manually from cellular biology image sets, but manually analyzing images is time-consuming and prone to potential bias in the selection of which events or structures will be manually assessed. These problems and the continued expansion of imaging assays has encouraged the adaption and development of novel methods to use computer vision methods to automatically assess the results of imaging assays. The development and application of computer vision methods to biological images sets is a nascent subfield of Bioinformatics named Bioimage Informatics [3].

Focal adhesions and Invadopodia are two cellular structures whose properties have traditionally been assessed using manual methods. While these protein complexes carry out different roles, with focal adhesions actings as cellular movement anchors and Invadopodia degrading the extracellular matrix, the image sets produced from studying them *in vitro* present quantification challenges which Bioimage Informatics methods can help solve.

1.1 Bioimage Informatics

The analysis of the images resulting from a biological assay shares many components with several closely aligned fields, including Medical Image Processing and Computer Vision [4]. The goals of Medical Image Processing is to develop methods to analyze the results of image collected in a medical context, such as X-Rays or MRIs. While the images analyzed in Medical Image Processing are produced using image modalities drastically different from fluorescence microscopy, many of the same methods are applicable to images produced for a biological experiment. Another overlapping field, Computer Vision, develops methods for teaching computers understanding images. Typically, these images have come from scenes taken using standard cameras, where the set of goals might include identifying the people in the scene and tracking their movements. These type of scenes are very different from the results of fluorescence imaging, but the problems of identifying and tracking objects are shared by both fields. Although Bioimage Informatics, Medical Image Processing and Computer Vision all focus on different goals, the methods developed in for one purpose can often be reused in other fields.

We can divide Bioimage Informatics into two classes. The first, high-throughput image analysis, is concerned with processing a large number of images to extract common cellular properties such as cell size or number [5]. High-throughput analysis methods are often used to analyzed images that have been fixed, thus removing the ability to study the dynamics of cellular processes. The second class, high-content image analysis, is concerned with processing an often smaller number of images to extract the properties of subcellular structures over time [6]. High-content analysis methods are mostly used to quantify dynamic processes at the subcellular level. Regardless of the goals or image sources, both high-throughput and high-content image analysis share many basic methods.

1.1.1 Methods Overview

The methods used in a Bioimage Informatics pipeline vary based on the specific type of images being studied and what type of data needs to be extracted from the images. In general though, each image analysis pipeline must address issues of image registration, segmentation, tracking, data extraction and visualization.

One of the first steps in most image analysis pipelines is registration. The goal of registration is to adjust the raw images collected by the microscope so that the field of view is held constant. In cellular microscopy, registration is often needed to compensate for inexact re-positioning of the objective during multiple field acquisition experiments. In these simple contexts, registration can often be accomplished using translation adjustments and gradient descent. There is also a great deal of overlap in registration methods with other related fields, such as image registration in a Medical Image Processing context [7]. The final result of image registration is a set of transformations which can be applied to the raw images to bring the image set into alignment.

Another stage of a typical Bioimage Informatics pipeline is segmentation. This stage of a typical pipeline analyzes the images and finds all the objects of interest in the image. In fluorescence cellular imaging, the identification of discrete objects of interest is complicated by irregular labeling of the components or low signal-to-noise ratios. Thus, many object segmentation pipelines involve a filtering step where background noise is minimized [8, 9]. After filtering the original images, thresholding selection methods, such as Otsu's [10] or the unimodal [11], are used to identify potential objects in the image. The resulting set of potential objects may then be matched against a template [9] if the type of object being segmented can be described by a standardized grayscale image. After the segmentation steps have been completed, the result is a list of the pixel locations of each object in the field of view.

Many of the questions concerning subcellular phenotypes deal with how objects change over time, so after segmentation, the objects in the images must be tracked [12]. Several tracking methods have been proposed for tracking segmented objects from biological image

sets. One proposed method uses global analysis to optimize the assignment of objects between frames and then uses these inter-frame assignments to build full tracking sequences [13]. Another proposed method uses Kalman filtering to predict the motion of objects moving in a controlled fashion [14]. This type of tracking methodology is most applicable to situations where the biological structure is moving in a very controlled fashion, such as in the case of microtubule tips. All of the proposed tracking methods produce a set of tracks which link the objects segmented in one image of a time-lapse set to another.

Finally, the results of the analysis must be visualized to ensure that the analysis methods have properly identified the structures of interest and new hypotheses can be formed. Several toolkits and software packages exist for visualizing the raw imaging data or the results of the image processing steps. The visualization toolkit (VTK, www.vtk.org) is an open source package which provides a range of methods for both 2D and 3D visualization. Imaris, produced by Bitplane Software (http://www.bitplane.com/go/products/imaris), is an integrated visualization and quantification system optimized for 3D and 4D image sets. The visualization steps act as a portion of an important feedback loop between finding a method to quantify a phenotype of interest and verifying that the phenotype is being property quantified by the analysis system.

1.1.2 High-throughput Image Analysis in Screening

Using modern robotics, it is now possible to test the effect of knocking down every known human gene or the effect of thousands chemical compounds on cell lines. Early screening efforts focused on properties which could be quantified without the use of imaging methods, such as percentages of cells living after treatment. These simpler screening methods are now complemented by methods which allow a representative sample of images to be gathered from the cells exposed to the knockdown construct or chemical. Typically, high-throughput imaging assays involve the culture of cells in a 384 well plate format, followed by addition of the compounds or siRNA vectors in seperate wells [15]. After some incubation time, cells are

fixed, stained and imaged. The volume of images that result from the screens are impossible to assess manually; image processing methods are necessary to determine the effect of the screen.

One popular open source software for analyzing screening experiments is CellProfiler [5]. This software, originally implemented in MATLAB, but now written in Python, provides a pipeline-based user interface. The user interface presents the most common steps needed to automatically find cells and extract the relevant properties from those cells. The software has been extended to include supervised machine learning methods to automate the learning of cellular phenotypes [16], the ability to analyze the results within the same interface[17] and analyze the images from C. Elegans screens [18].

Image analysis of screening results has been used to study a range of biological phenomena. The effect on overall cell morphology was assessed in *Drosophila* BG-2 cells using an siRNA screen of 250 genes [19]. Using both human and drosophila cells, siRNA was used to search for actin interacting proteins and regulators [20]. Two screens of focal adhesion morphology in fixed cells have been conducted. The first screen used a natural products library and identified 15 different components that perturbed focal adhesion morphology [21]. The second screen used an siRNA library covering human kinases, phosphatases and FA-related genes [22]. This screen found seven clusters of genes that affected FA morphology in terms of FA length, area, intensity and other properties. One screen of Invadopodia activity has also been reported [23]. This natural products library screen used the LOPAC 1280 collection to determine the effect of these products on invadopodia formation. The number of Invadpodia measured by identifying Invadopodia from fixed Src-transformed NIH3T3 cells stained for actin. Invadpodia were assigned to individual cells by first identifying nuclei after DAPI staining and then assigning Invadopodia to the nearest identified nuclei. The screen ultimately identified seven active compounds.

1.1.3 High-content Image Analysis in Cell Biology

In contrast with high-throughput Bioimage Informatic analysis, high-content image analysis focuses on extracting new properties from biological image assays, typically from time-lapse image sets. These biological experiments are designed to monitor highly dynamic structures, typically in single cells, which are too complicated to be readily quantified via manual methods. Although many microscopy heavy field of cell biology have benefited from high-content image analysis, I will highlight the study of cell edge, microtubules and clathrin-coated pits as applications of high-content analysis methods.

One area of cell dynamics that has been extensively quantified using Bioimage Informatics is the cell edge of migrating cells. The edge of migrating cells is highly dynamic with protrusions and retractions occurring in response to intra- and extra-cellular cues. To quantify the intracellular cues thought to play a role in driving edge movement, a series of biosensors were developed in Klaus Hahn's lab, including sensors for Rac [24], RhoA [25] and CDC42 [26]. These biosensors allow realtime activity levels of the monitored proteins to be observed using fluorescence microscopy. Early methods of quantifying the biosensor activity levels involved taking line scans radially through the cell edge during specific protrusion or retraction events to quantify RhoA activation during cell edge movement. This line-scan-based method was time-consuming and did not capture the subtleties of cell edge movement. To improve upon these manual analysis methods, Gaudenz Danuser and colleagues developed a set of image analysis methods to automatically determine the local speed of the cell edge [27]. They developed two methods to quantify cell edge movement. The first used the level set method to track the evolution of the cell edge, while the second simpler method used a spring model to follow edge movement. The biosensor signals for RhoA, Rac and CDC42 were then correlated with the cell edge movement to determine the proteins order of activation in time and space [28]. By integrating sophisticated imaging methodologies with quantitative image analysis, the relative ordering of intracellular signalling pathways could be dissected in living cells.

Microtubule dynamics are another area of cell dynamics that has benefited from high-

content image analysis. Microtubules are highly dynamic components of the cytoskeleton which are involved in cellular activities ranging from separating sister chromatids at mitosis to protein trafficking [29, 30]. Microtubules go through cycles of extension and retraction over the course of minutes and are densely packed within the cytoplasm. To analyze microtubule dynamics, fluorescent markers of the growing microtubule tip have been developed and used to observe microtubule development in cells. The density and quantify of tips in cells greatly complicated the process of quantifying the dynamics of these structures. Image analysis methods have been developed to segment, track and analyze the time-lapse images of microtubules [9]. This automated approach provided for a comprehensive characterization of microtubule behavior in living cells and a platform for developing new microtubule quantification metrics.

Clathrin-coated pits are another class of cellular structures with complicated dynamics [31]. These structures form on the outer edge of cells and allow cells to internalize extracellular factors and recycle the cell membrane. One experimental setup to study clathrin-coated pits labels the developing pit with a ph sensitive dye, allowing hundreds of these structures to be visualized in a single cell. Prior methods for studying these structures used manual tracking and analysis, but the application of automated segmentation and tracking methods allowed the number of quantifiable pits to be greatly expanded [32]. This expansion in the number of quantifiable pits allowed subtle differences in pit lifetime and the effect of an siRNA knockdown of dynamin-2.

1.2 Thesis Contributions

This thesis describes a set of analysis methods which fit into the framework of Bioimage Informatics. Specifically, this thesis details methods for analyzing Focal Adhesions (Chapters 2 and 3) and Invadopodia (Chapter 4). Both of these structures have been extensively studied using fluorescent microscopy methods. Prior methods have been developed to automatically segment Focal Adhesions structures from fixed images and measure properties such as area, shape and fluorescence intensity. In contrast, Focal Adhesion dynamics have typically been

assessed using time-consuming manual analysis methods, which has limited the quantity and type of results that could be collected from fluorescence imaging. In Chapter 2, a framework for segmenting, tracking and quantifying standard Focal Adhesion properties is described. This framework is expanded in Chapter 3 to spatial and global analysis of FA cellular location and alignment. Much like Focal Adhesions, Invadopodia are often quantified using manual methods. Chapter 4 describes a system for analyzing Invadopodia using Bioimage Informatic techniques. This system has two parts, which can automatically identify, track and classify Invadopodia in single cells. The second part of the system can follow the degradation activities of single cells through time. Both of these systems provide automated methods for the quantification of Focal Adhesions and Invadopodia, which improve upon the current manual analysis methods.

Chapter 2

High-resolution Quantification of Focal Adhesion Dynamics in Living Cells

2.1 Introduction

Focal adhesions (FAs) are dynamic, multi-component protein complexes that serve as points of integration for both mechanical and chemical signaling, while playing a central role in a variety of processes including cancer metastasis, atherosclerosis and wound healing [33, 34, 35]. Characterizing how these structures dynamically change is essential for understanding cell migration, which requires that adhesions are continuously remodeled as the cell moves forward. During motility, new adhesions are born at the leading edge of a protruding lamellipodia. They then enlarge and are either disassembled at the base of the protrusion in a process known as adhesion turnover, or become longer-lived structures that are eventually dismantled in the retracting tail at the rear of the cell [36, 37, 38]. In this cycle as well as other FA-mediated processes, FA dynamics are highly regulated by structural and signaling molecules [39, 40, 41]. Alterations in the balance of these regulating factors plays a key role in adhesion turnover and thus in adhesion signaling and normal cell function.

Microscope imaging of FAs underlies a significant portion of our current understanding of adhesion dynamics, with methods such as total internal reflection fluorescence microscopy (TIRF) providing high-resolution images suitable for quantitative analysis [42]. However, challenges in image capture and downstream analysis have generally led to the characterization of only a relatively small number of hand-picked adhesions within any given cell [39, 40, 43, 44, 45]. Recent technical and methodological improvements have allowed for

the automated detection and characterization of focal adhesions for high-throughput screening studies. For instance, Paran and colleagues [21] have reported on the use of a high-throughput high-resolution imaging system to screen a plant extract library for effects on adhesion morphology and distribution. The same high-throughput imaging system was used to perform multicolor analysis on various adhesion components [46] and this system was used in an siRNA screen against adhesion related genes [22]. In these studies, researchers were able to obtain molecular signatures of protein components within focal adhesions, resolve subdomains within adhesions, and identify clusters of genes that had similar effects on focal adhesion morphology and placement. These studies demonstrate the power of identifying and characterizing large numbers of adhesions within a cell. However, as the approaches used in these studies relied on cell fixation, critical aspects of focal adhesion biology, including their spatiotemporal dynamics, were lost.

Here, we describe a novel system for the quantification of focal adhesion dynamics. This approach utilizes high-resolution (60x oil-immersion) time-series images of living cells generated with TIRF. Image sequences are processed through an analysis system that identifies individual adhesions based on user-defined criteria, tracks their movement through time and collects associated properties concerning their location, shape, size and intensity. As adhesion properties throughout the lifetime of each adhesion are quantified in this approach, a thorough picture of global adhesion spatiotemporal behavior is captured.

To demonstrate the capabilities of this computational approach, we focus on characterizing adhesions via the molecular scaffold protein Paxillin, a core constituent of focal adhesions commonly used in adhesion imaging [47]. Specifically, in this study we use our image analysis system to characterize FAs labeled with EGFP-Paxillin, generating high-resolution data sets of adhesion distribution, morphology, and turnover in migrating NIH 3T3 fibroblasts. The results demonstrate that we can analyze adhesions in an unbiased manner, with 10^3–10^4 adhesions analyzed per cell. With wild-type Paxillin as a baseline for comparison, we use our system to detect alterations in adhesion spatiotemporal properties in response to the S178A mutation on

Paxillin. Through this analysis we show that the loss of this single phosphorylation site affects adhesion site formation, size and assembly rates. We also verify the broad applicability of the analysis system by also applying the methods to examine time-lapse movies of EGFP-FAK. We are also making the analysis system available under an open source license, to allow the community to use our methods to analyze new experimental systems. These results illustrate the benefit of automated large-scale characterization of adhesion properties and behaviors, allowing both large and subtle differences to be readily detected.

2.2 Results

2.2.1 Quantitative Analysis of Focal Adhesion TIRF Images

To quantify aspects of focal adhesion spatiotemporal dynamic behavior, we generated an NIH 3T3 fibroblast cell line expressing both EGFP-Paxillin, to label FAs, and a myristoylated-Red Fluorescent Protein (myr-RFP), to identify the cell edge. Cells were plated on fibronectin and imaged with TIRF for 14 hours. We then quantified FA dynamics through a multistage image analysis pipeline (Figure 2.1). Briefly, after high-pass filtering, FAs were identified and segmented with a watershed-based algorithm (see Methods). Characteristics of adhesions identified and quantified at each timepoint included properties such as area, position and fluorescent Paxillin intensity. Dynamic properties of adhesions, such as velocities and changes in fluorescent intensity, were also determined by tracking and measuring adhesion properties across time steps/images. At each consecutive time step the appearance of new adhesions, called birth events, and the disappearance of adhesions, called death events, were similarly identified and recorded by the software.

An example of the segmentation results and characteristic properties are shown in Figure 2.2. The segmentation methods successfully identify the adhesions in each image regardless of the background Paxillin fluorescence intensity (Figure 2.2A, B). The dynamic nature of the adhesions during this experiment is clear when all the adhesions identified are shown superimposed in a single image (Figure 2.2C). The results also show several general properties

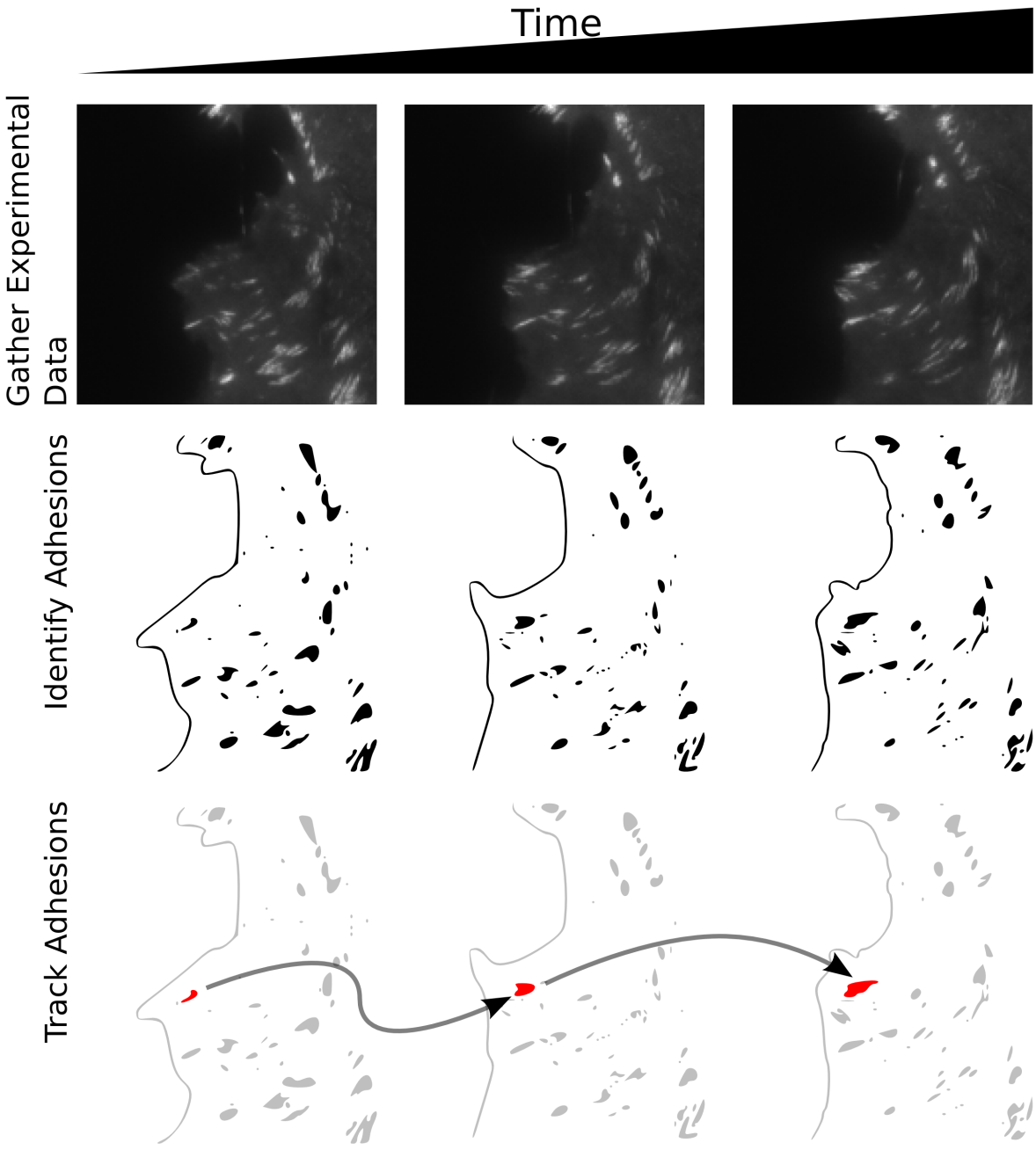

Figure 2.1: Automating the analysis of focal adhesion images requires a multi-stage pipeline. The first row shows several representative images of fluorescently labeled Paxillin using TIRF microscopy. In the second row, a cartoon depiction of the segmented adhesions and the cell edge are shown. Identification of the adhesions in each image allows a set of characteristic morphological and fluorescence intensity-based features to be extracted. The third row shows a single adhesion (highlighted in red) being tracked through the short sample time course. The properties of each adhesion are tracked over time, allowing the large scale dynamics of FA to be determined.

of the adhesions in wild-type cells (Figure 2.2D). In general, adhesions are less than 0.2 μm^2 in size, have axial ratios less than 3 and exist for less than ten minutes, although there are many adhesions that live longer. Both Paxillin fluorescence intensity and the position of the adhesion centroids with respect to the cell edge have skewed distributions. These results demonstrate the capabilities of our system to provide high-resolution and unbiased assessment of FA behavior.

2.2.2 Kinetics of FA Assembly and Disassembly

Of particular importance for understanding FA functions is the assessment of adhesion behavior through time. Figure 2.3A-D shows the methods used in determining FA assembly and disassembly rates for individual adhesions. Figure 2.3A depicts an image series of a single adhesion (highlighted in green) from birth, through maturation and stability, and on to death. Using time series information, we quantified the normalized intensity of each adhesion over its lifespan (Figure 2.3B). Readily apparent are the log-linear assembly and disassembly phases, which are automatically fit to a log-linear model (see Methods for details). Our results are consistent with previous work showing that adhesions assemble and disassemble with log-linear progression [39]. Specifically, we found that the log-linear fits for most of the adhesions produced R^2 values above 0.7 (Figure 2.4). Note that the smaller number of adhesions analyzed relative to Figure 2.2 is due to the need for a minimum adhesion lifetime ($>$20 minutes) as well as other requirements needed for the accurate quantification of assembly and disassembly rates (see Methods). In the example shown in Figure 2.3, a log-linear approximation describes 90.5% and 96.1% of the variance in the rates of intensity increase and decrease, respectively (Figure 2.3C, D). In between these two phases we define a stationary/mature phase where intensity remains relatively stable (Figure 2.3B).

We used our system to characterize the rates of FA assembly and disassembly by repeating the analysis detailed in Figure 2.3AD on all adhesions identified in the EGFP-Paxillin data set by our software (n = 21 cells). Results were focused on FAs having lifetimes of at least 20

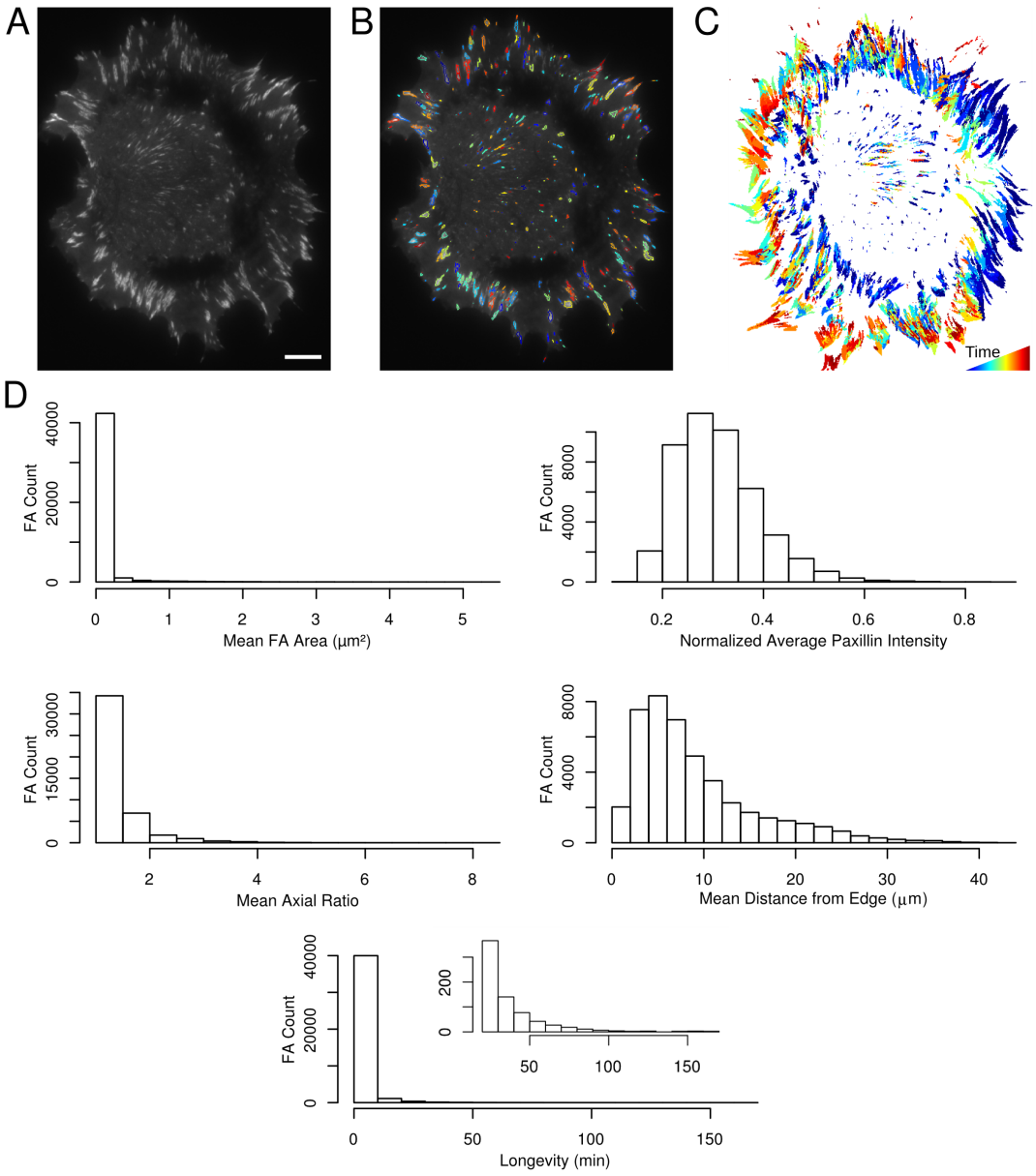

Figure 2.2: Applying quantitative image processing methods to FA images allows comprehensive characterization of FA properties. (A) One frame from a 200 minute movie of NIH 3T3 cells expressing GFP-Paxillin (the scale bar represents 10 μm). (B) The same cell as in (A), with each adhesion outlined in a different color. (C) The entire set of adhesions in an experiment can be visualized by overlaying the adhesions from each microscopy image using a different color for the set of adhesions at each time point. This example includes the adhesions from 198 images. (D) A range of properties can be extracted from the segmented FA. Five samples are provided. The area histogram was filtered to only include adhesions with areas less than 5 μm^2. The axial ratio histogram was filtered to only include adhesions with an axial ratio of 8 or less. The longevity histogram includes all adhesions, while the inset only includes adhesions with longevity greater than 20. The histograms include data from 21 cells.

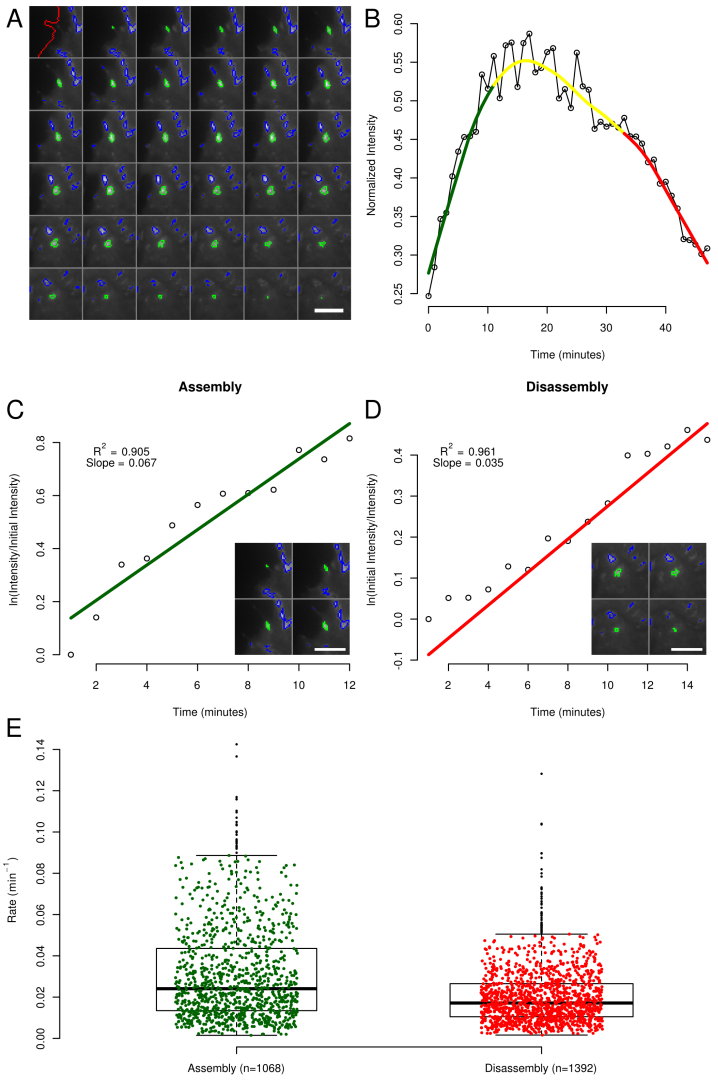

Figure 2.3: Automated measurement of focal adhesion dynamics. (A) Each of the adhesions in the cells is tracked, allowing the position and properties of single adhesions and populations to be assessed. Here a single adhesion (in green), the surrounding adhesions (in blue) and the cell edge (in red) are followed for 49 minutes. The cell edge is only outlined in the first frame. The scale bar is 10 μm. (B) The intensity of EGFP-Paxillin in the tracked adhesion in (A) through time. The green, yellow and red lines are smoothed using the Lowess algorithm and correspond to the assembly, stable and disassembly phases, respectively. (C) The normalized log-linear fit of the Paxillin intensity through time during the assembly phase of the adhesion in part (B). The inset depicts several of the images from which the Paxillin intensity was gathered. (D) The normalized log-linear fit of the Paxillin intensity through time during the disassembly phase of the adhesion in part (B). The inset depicts several of the images from which the Paxillin intensity was gathered. (E) The assembly and disassembly rates for adhesions whose Paxillin intensity curve fits have R^2 values of 0.9 or greater. The top and bottom lines of the boxes indicate the 3rd and 1st quartiles respectively, while the bold central lines indicate the median values. The whiskers extend up to 1.5 times the interquartile range.

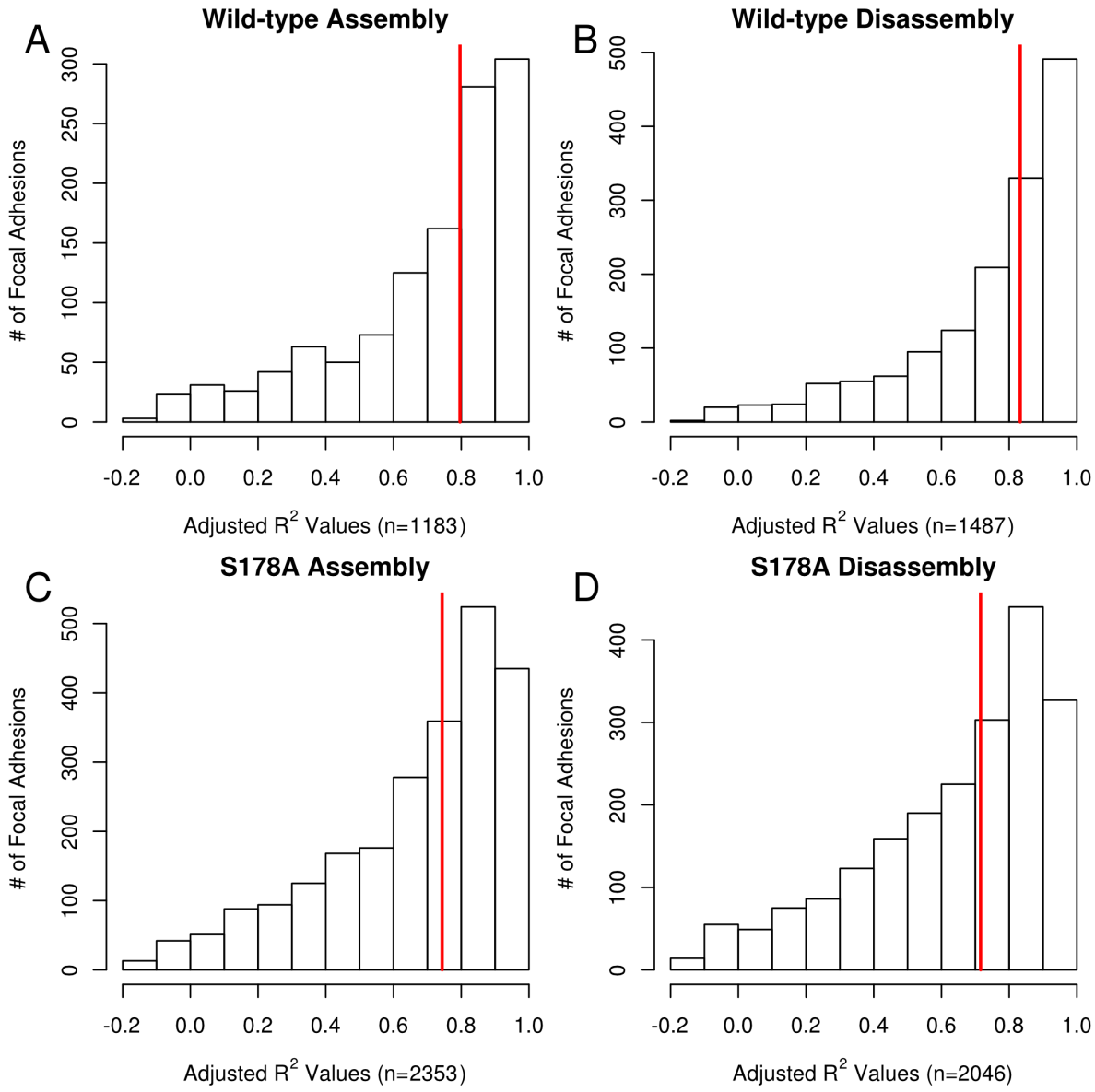

Figure 2.4: The assembly and disassembly log-linear models fit the Paxillin intensity time courses with high R^2 values. The red lines indicate the median length-adjusted R^2 values.

minutes, where the detected assembly or disassembly rate is positive and the p-value of the rate model is below 0.05 (Figure 2.3E). The mean rate of assembly of 0.031 ± 0.023 min^{-1} is 55% greater than that of disassembly (0.020 ± 0.014 min^{-1}). While these average rates are slower than earlier published reports, the values determined in previous studies were estimated from far fewer measurements (typically dozens of adhesions) and can be found within the variance of our data set. Thus, this automated computational approach provides a comprehensive picture of the breadth of adhesion assembly and disassembly dynamics without biasing analysis toward any particular subset of adhesions.

2.2.3 Spatial Properties of FA Assembly and Disassembly

In addition to estimation of assembly and disassembly rates, the analysis pipeline also collects spatial properties of FAs, allowing spatial aspects of FA behavior and dynamics to be similarly studied. Using the same set of experiments used to determine the kinetics of assembly and disassembly, we asked where, relative to the cell edge, adhesions tend to be born/die (Figure 2.5). The majority (63%) of adhesions are born less than 5 μm from the cell edge, with a mean distance from the edge at birth of 6.34 μm (Figure 2.5A). In contrast, adhesions tend to die further from the edge with only 27% of adhesions dying within 5 μm of the edge (Figure 2.5B). The mean distance from the edge at death was 9.5 μm. This suggests the existence of two distinct, but partially overlapping zones within which preferential birth or death of FAs occurs. When looking at both FA birth/death location and assembly/disassembly rate simultaneously, we find that higher assembly rates are observed in births that occur near the edge while no obvious effect of spatial location on the rate of disassembly is apparent (Figure 2.5).

2.2.4 Analysis of EGFP-labeled FAK adhesions

To support the use of these methods in the study other FA proteins, we expressed FAK labeled with EGFP. After gathering time-lapse movies of 10 cells tracking the position of FAK

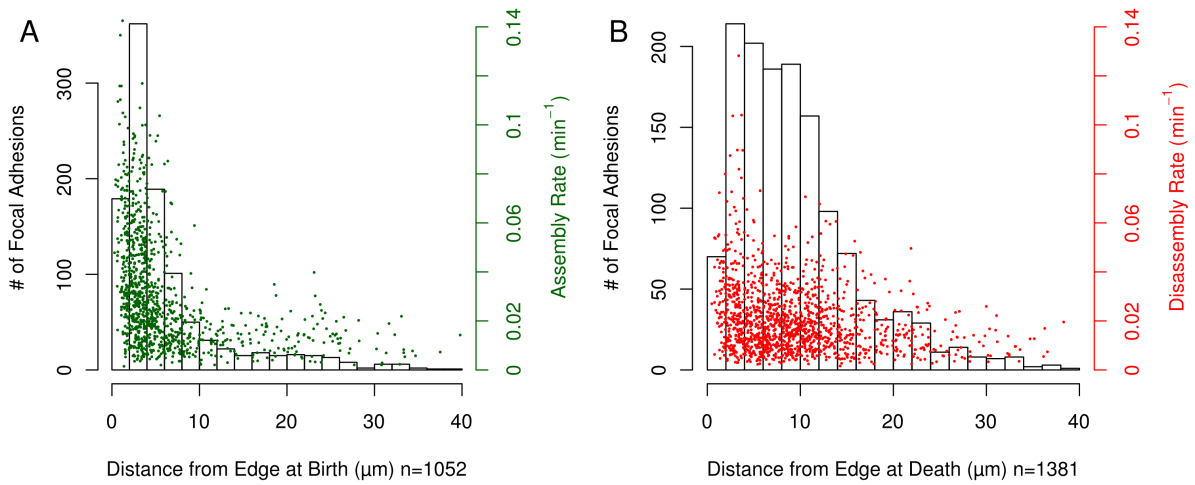

Figure 2.5: Spatial properties of FA positions at birth and death. (A) The majority of adhesions are born within 5 μm of the cell edge and the greatest variance in assembly rates are also observed in this 5 μm band. (B) The distribution of the distance of death location from the cell edge indicates that adhesion disassembly typically occurs along a broader band from the cell edge as compared to the position at adhesion birth. Also, the variance in disassembly rate is roughly the same regardless of the position at adhesion death. This data was collected from 21 EGFP-Paxillin cells.

in NIH 3T3s using TIRFM, we applied the same set of algorithms to determine the assembly and disassembly rate of the FAs. The rates of assembly and disassembly of FAs were found to be statistically indistinguishable when comparing labeled Paxillin to labeled FAK in live cells (Figure 2.6). In contrast, subtle but statistically significant differences in adhesion areas and axial size were found when comparing EGFP-Paxillin vs EGFP-FAK labeled adhesions (Figure 2.7). This result is not unexpected as different spatial and/or stoichiometric relationships are expected for both Paxillin and FAK within FAs [48, 49]. These results further indicate the capability of this system to be generally applicable to the measurement of other adhesion components besides Paxillin.

Paxillin S178A Mutant Perturbation

The previous results establish the ability of our approach to quantify various adhesion properties and behaviors. Furthermore, the ability to identify and characterize very large numbers of adhesions provides the potential to detect changes in adhesion phenotype that are difficult or impossible to characterize manually and/or with small numbers of measurements.

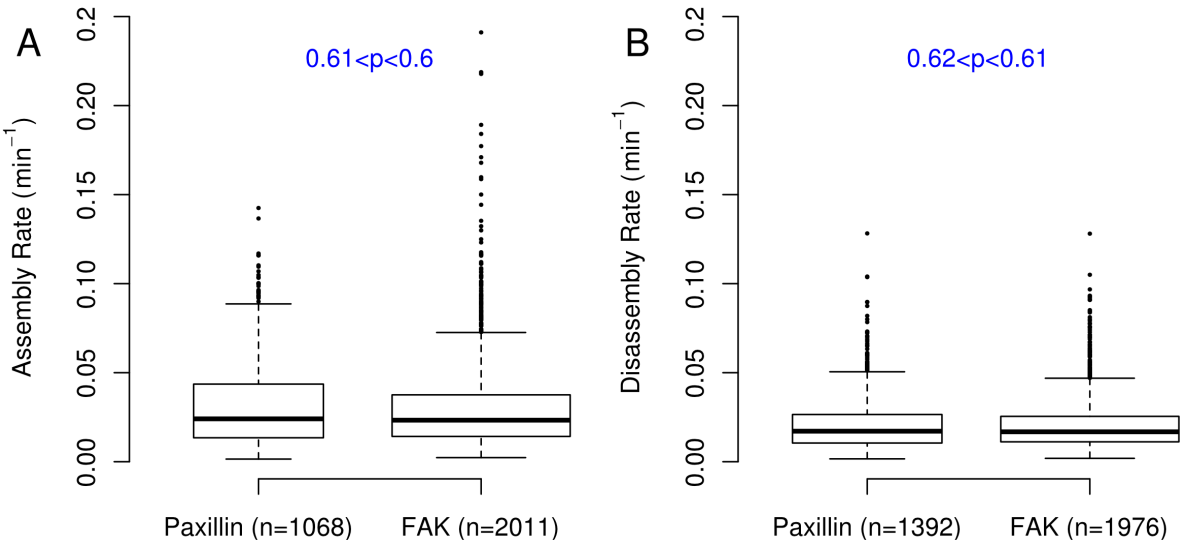

Figure 2.6: The assembly and disassembly rates of EGFP-Paxillin and EGFP-FAK adhesions are the same. The blue numbers in each plot are the p-values of the difference in median values between the EGFP-Paxillin and EGFP-FAK adhesions. P-values were calculated using the bootstrapped confidence intervals with 50000 replicates. Data from 10 cells are included.

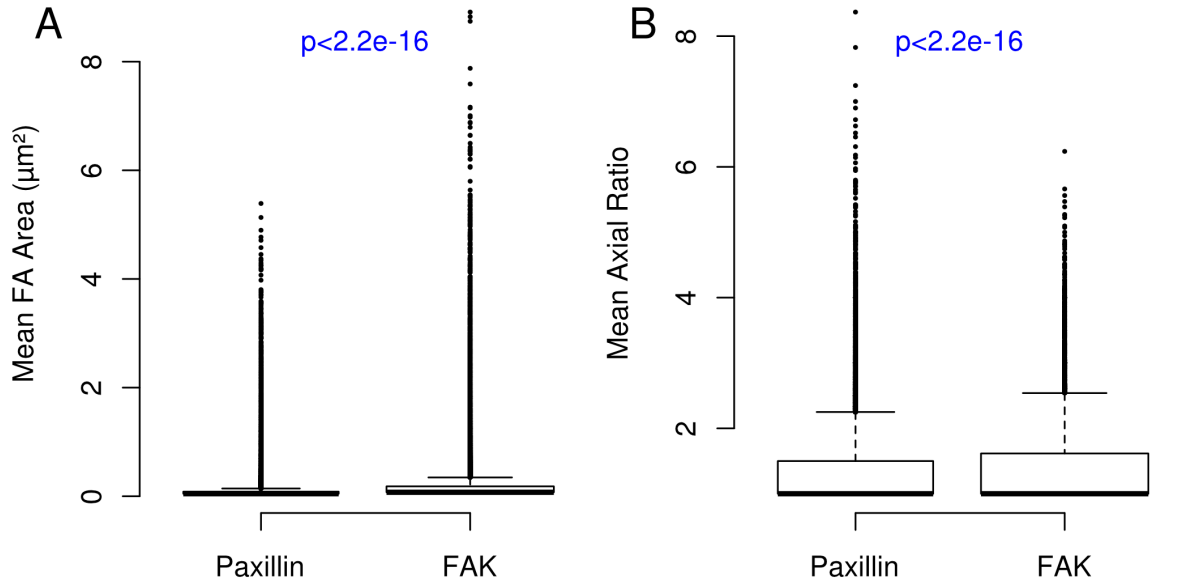

Figure 2.7: Adhesions labeled with EGFP-FAK are larger in mean area and have a larger axial ratio than those labeled EGFP-Paxillin. There are 51836 adhesions in the FAK data set and 44685 adhesions in the Paxillin data set. The p-values were calculated using the same methods as Figure 2.6.

As a proof-of-principle, we utilized our system to investigate the effect of a Paxillin mutation (Serine 178 to Alanine) on several aspects of FA behavior. Specifically, a principal regulatory mechanism of Paxillin is phosphorylation, with over 40 sites of phosphorylation currently identified [41]. The roles of many of these phosphorylation sites have yet to be characterized, but many of those that have been studied demonstrate strong effects on cell migration. Of particular interest is the c-Jun N-terminal kinase (JNK) phosphorylation site Serine 178 (S178). Preventing JNK phosphorylation through mutation of this Serine to Alanine, or by inhibition of JNK signaling, inhibits cell motility [50, 51]. More recently, it has been shown that phosphorylation of S178 enhances Paxillin's interaction with FAK, resulting in tyrosine phosphorylation at residues 31 and 118 [52]. Furthermore, expression of the phosphomimetic Y31D/Y118D Paxillin can rescue the S178A mutant phenotype. This and related work suggests that JNK phosphorylation of Paxillin may be an important early step in adhesion formation. However, the effects of this mutation on adhesion dynamics have not been well characterized.

Using our analysis system we found that the S178A mutation induced a number of significant effects on the morphological, dynamic and spatial properties of adhesions. The mean area of the S178A mutant adhesions decreased by 23%, while the mean axial ratio decreased by 5% in the S178A mutants (Figure 2.8). Perhaps most relevant to the observed alterations in cell motility, there is an approximately 42% reduction in the median rate of adhesion assembly (Figure 2.9A). We also observe a smaller (30%) but statistically significant decrease in median disassembly rate (Figure 2.9B). Thus, the kinetics of FA assembly and disassembly are strongly affected by this mutation, but in a non-symmetric manner.

We previously observed that adhesions in wild-type cells have different distributions of birth and death positions relative to the cell edge. In comparison to WT cells, we find that the median distance from the edge at birth is greater by 30% in S178A mutants (Figure 2.6C). There is no significant difference between WT and mutant cells with regard to where an adhesion dies, suggesting that spatial aspects of the disassembly process (i.e. where disassembly

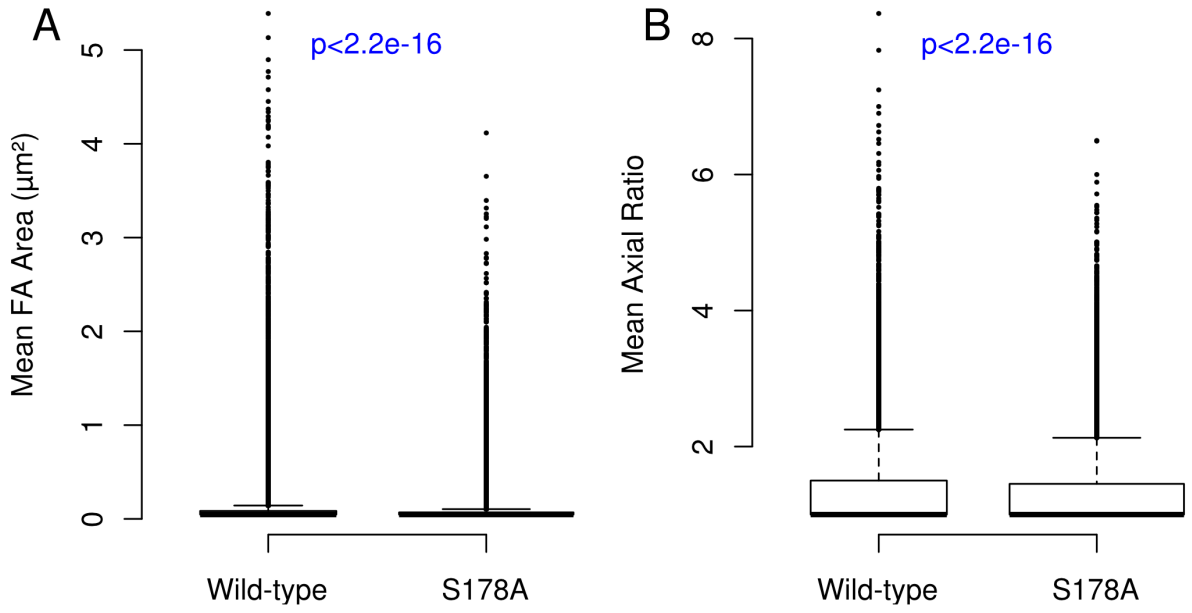

Figure 2.8: The S178A mutation in Paxillin decreases adhesion size and axial ratio. There are 44685 adhesions in the wild-type and 73305 adhesions in the S178A data sets. The p-values were calculated using the Wilcox Rank Sum test. Data from 9 cells are included in the S178A data set.

occurs) is not dependent and/or sensitive to JNK phosphorylation (Figure 2.6D).

Finally, we compared the length of time spent in the assembly, stationary, and disassembly phases for cells expressing either WT or S178A EGFP-Paxillin. Results suggest that the S178A mutation causes adhesions to be longer-lived, spending a greater amount of time in the assembly phase than WT cells and lesser time in the disassembly phase (Figure 2.10). There is no difference in time spent in the stability phase. As a whole, our results demonstrate the most pronounced effects of the S178A mutation occur in the assembly phase: position at birth, assembly rate, and time spent assembling.

2.3 Methods

2.3.1 Cell Culture

NIH 3T3 fibroblasts and 293 LinXE ecotropic packaging cells were cultured in 5% CO^2 at 37 °C in Dulbecco's modified Eagle's medium (DMEM, Mediatech) supplemented with 10%

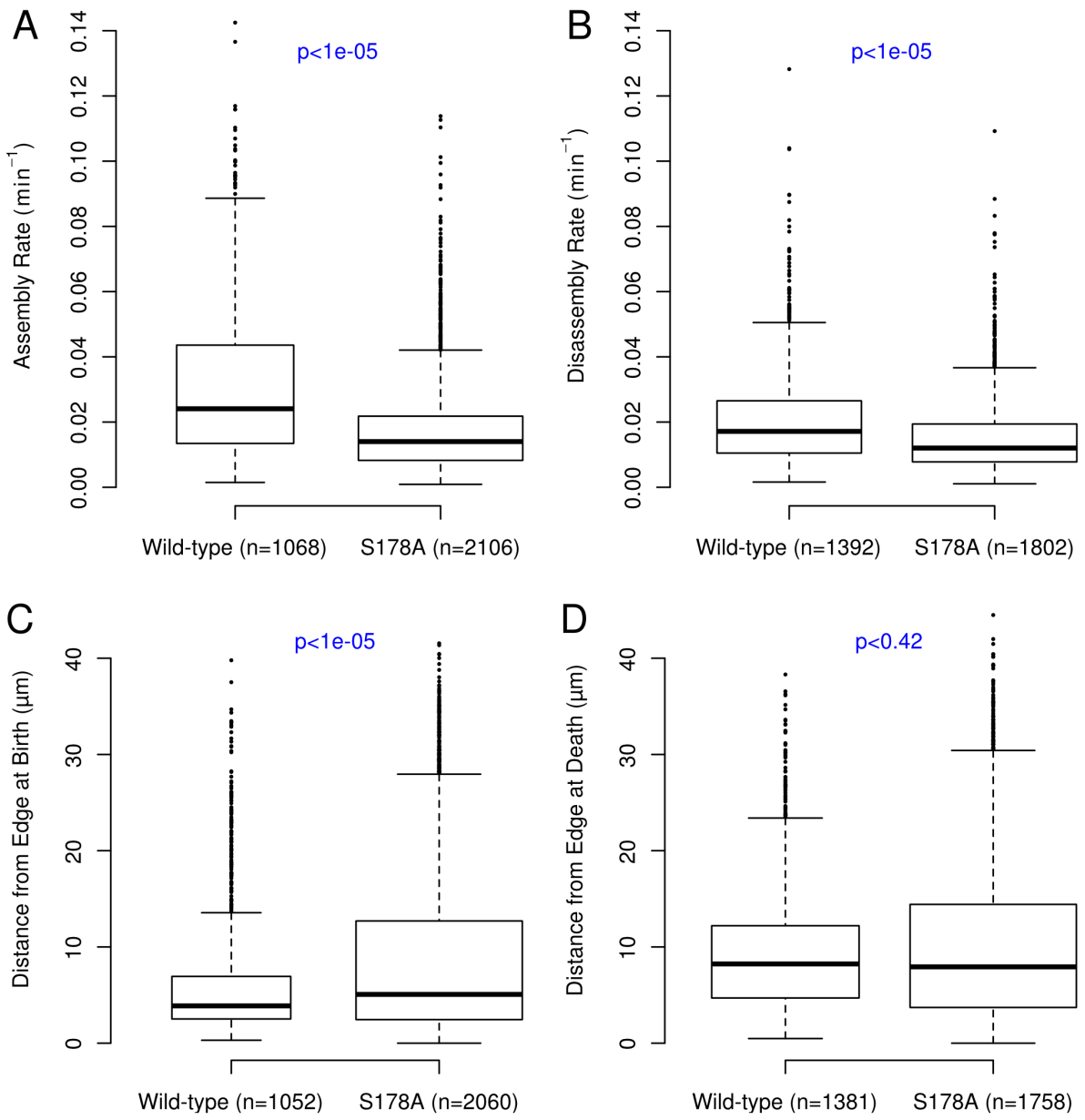

Figure 2.9: The S178A mutation in Paxillin alters adhesion assembly and disassembly. (A and B) The rate of adhesion assembly and disassembly are significantly decreased by the S178A mutation. The S178A median FA assembly rate is decreased by 42% compared to the wild-type cells, while the median disassembly rate is decreased by 36%. (C and D) The S178A mutation shifts the median adhesion birth location away from the cell edge, but has no effect on the location of cell death. The S178A median adhesion birth position is 31% greater than wild-type median birth position. The median position at adhesion death is decreased by 4% between the S178A and wild-type cells. P-values were calculated in the same manner as in Figure 2.6.

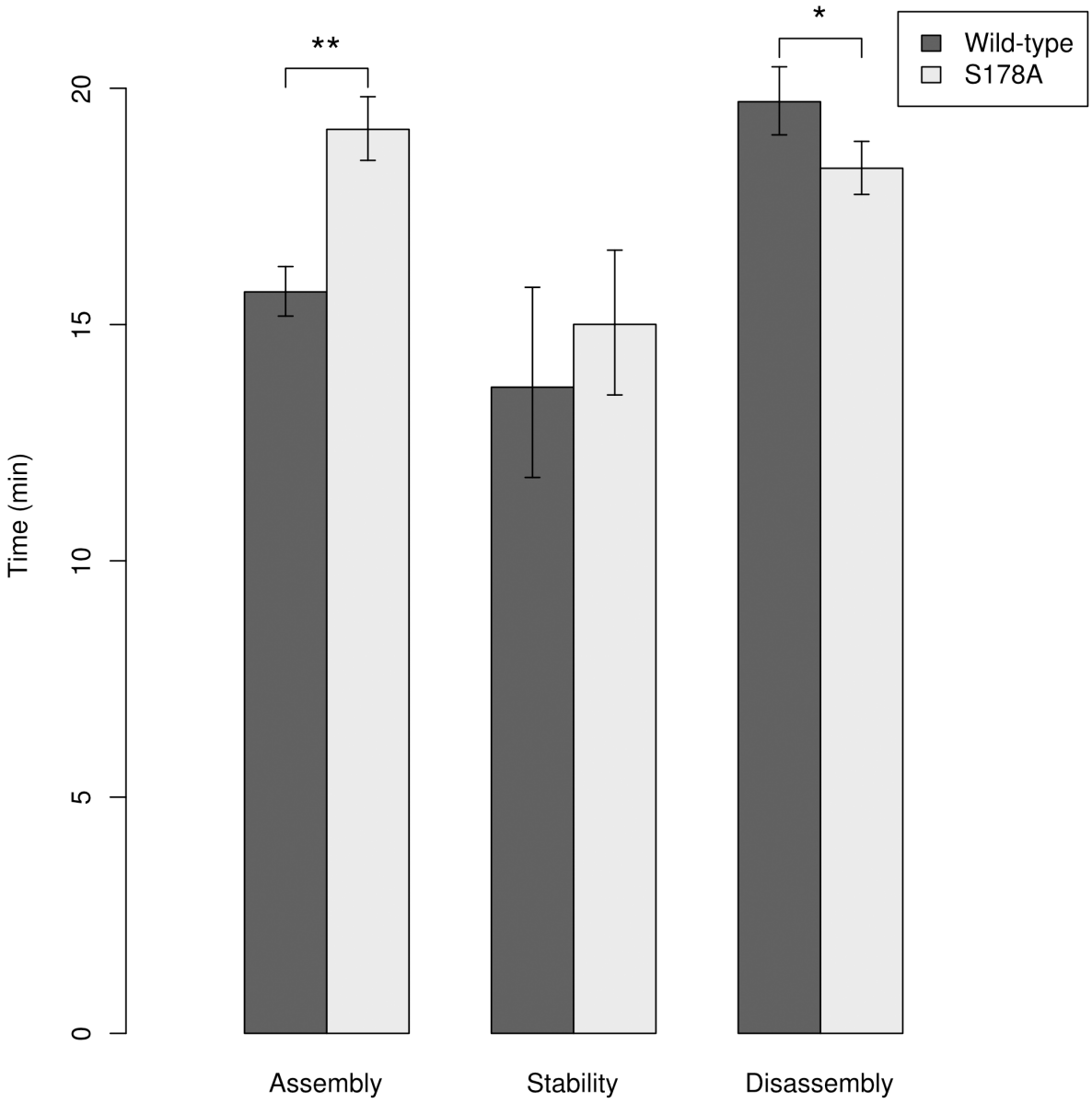

Figure 2.10: The lengths of the assembly and disassembly phases in S178A mutant FAs are significantly different from those in the wild-type, while the stability phase lengths are unaffected. The phase length values include all adhesions where the log-linear models fit with a p-value of 0.05 or less. Error bars indicate 99% confidence intervals on the mean phase length as determined through 50,000 bootstrap samples. A double asterisk (**) indicates p¡105 and single asterisk (*) indicates p¡0.05. Wild-type N Values: Assembly (1068), Stability (465), Disassembly (1392); S178A N Values: Assembly (2106), Stability (870), Disassembly (1802).

fetal calf serum, 1% L-Glutamine, and 1% penicillin-streptomycin. Fibroblasts were imaged in Ham's F-12K medium without phenol red (SAFC Biosciences) with 2% fetal bovine serum, 15 mM HEPES, 1% L-Glutamine, and 1% penicillin-streptomycin.

To make stable cell lines, retroviral vectors were transfected into 293 LinXE cells plated in 6 cm dishes with Fugene 6 (Roche) according to the manufacturer's protocol (using 18 μL of Fugene 6 and 4.5 μg of DNA). The media was replaced after 12 hours. Viral supernatant was harvested 48 hours after media replacement, passed through a .45 μm syringe filter and then added to NIH 3T3s plated at subconfluent densities at a ratio of 1:3 (viral supernatant/normal media). Cells were infected for several rounds until they reached expression levels sufficient for live cell imaging. All of the constructs used in this study have been verified to colocalize with endogenous proteins [50, 53, 54]. No differences were detectable in the expression levels of the EGFP-Paxillin and EGFP-PaxillinS178A constructs (Figure 2.11).

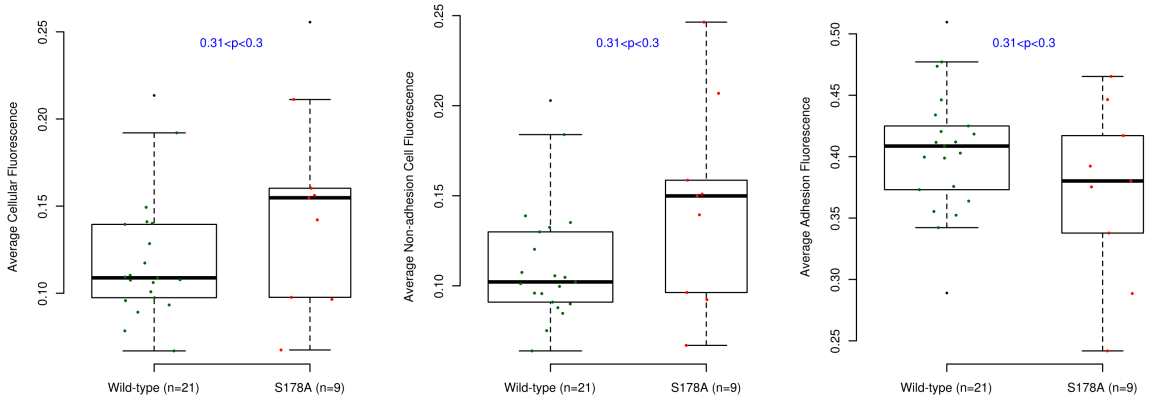

Figure 2.11: There are no significant differences between the expression levels in the EGFP-Paxillin and EGFP-PaxillinS178A cell lines. The average intensity of fluorescence inside the cell is shown in three different ways: the overall cell intensity (A), inside the cell not including the adhesions (B) and only the adhesions (C). The error bars are 95% confidence intervals determined using 50,000 bootstrap samples on the mean value.

2.3.2 Microscopy

Prior to imaging, NIH 3T3s were plated onto coverslips coated with 5 μg/mL Fibronectin (Sigma) for 30 min. Fibroblasts expressing EGFP-PaxS187A required 23 hours to adhere to the coverslips due to a spreading defect. Immediately before being transferred to a sealed

imaging chamber, complete culture media was replaced with imaging media. Imaging experiments for all cells used in this study were conducted within the first 8 hours after plating.

Imaging was performed on an Olympus IX81 motorized inverted microscope equipped with a ZDC focus drift compensator and a TIRFM illuminator, a 60X 1.45 NA PlanApoN TIRFM objective, a cooled digital 12-bit CCD camera (CoolSnap, Roper Scientific), a 100 W Mercury arc lamp, and MetaMorph imaging software. The 488 nm laser line from a Krypton-Argon ion laser (Series 43, Omnichrome) was controlled with a custom laser launch/AOTF (LSM Technologies). Imaging of the cells expressing EGFP-FAK was performed on a Nikon Eclipse Ti inverted microscope equipped with the Perfect Focus System, a TIRF illuminator, a 60X 1.45NA PlanApoN TIRF objective, a a cooled digital 16-bit EMCCD camera (QuantEM: 512SC, Photometrics), an Argon ion laser (Melles Griot) controlled with a custom laser launch/AOTF, and Nikon Elements imaging software. Images were acquired with 22 binning, except for images of EGFP-FAK expressing cells, which were acquired with 11 binning. Images were gathered once every minute. Illumination intensity was controlled with either the AOTF (TIRF excitation) or neutral density filters (epifluorescence excitation). Simultaneous TIRF images of EGFP and epifluorescence images of RFP were acquired using an 80/20 (TIRF/Epifluorescence) splitter mirror, a custom dichroic mirror (Chroma) and the following band-pass filters: EGFP (HQ 525/50); RFP (HQ580/30, HQ 630/40). In total, 21 EGFP-Paxillin, 9 EGFP-PaxillinS178A and 10 EGFP-FAK cells were included in this study. The EGFP-Paxillin experiments were conducted over four days, while the EGFP-PaxillinS178A experiments were conducted over three days and the EGFP-FAK experiments were conducted over three days.

2.3.3 Image Processing

Methods to identify individual FAs were adapted from [8], with some modification. Briefly, each image taken during an experiment was high pass filtered, using a round averaging filter with a radius of 11 pixels (4.95 m diameter). The high pass filtered images were threshholded

by an empirically determined value set to identify adhesion pixels. The water segmentation method was used as described, but with the following modifications. When a pixel acts as bridge between two large adhesions, where large is defined as 40 or more pixels (1.85 m2), the bridge pixel is assigned to the adhesion whose centroid is closest to the bridge pixel. Also, holes in any single adhesion were filled using the same water segmentation algorithm. Between 200 and 600 adhesions were found in each image from the experimental data. The average signal-to-noise ratio was 6.04 as calculated by dividing the mean of the adhesion intensity by the standard deviation of the backgound pixels [55]. After each focal adhesion has been identified, characteristic adhesion properties, such as those in Figure 2, are then collected.

Cell edges were found by analyzing the myr-RFP images using a method similar to that described in a prior publication [27]. This method automatically identifies a single threshold which splits the myr-RFP images into cell body and background regions. Briefly, a histogram of all the intensity values for a single image was collected and split into 1000 equal sized bins. The counts of each bin were then smoothed with the loess algorithm (Polynomial order 2, 5% of data included in each fit). This smoothed histogram has two peaks corresponding to the background region and the cell body. The local minima and maxima in the smoothed histogram are found and the two maxima at the lowest pixel intensity bins identified. The threshold for image segmentation is set to the minima between the set of maxima found in the prior step. After thresholding the image, the connected regions are identified and the regions less than 10 pixels in area are discarded. The cell edge is defined by the border pixels of the connected regions.

2.3.4 FA Tracking

With the focal adhesions identified in each image of the experimental data set, another series of algorithms were designed to track the focal adhesions through each sequential image. The tracking algorithm is based on a birth-death model of a FA lifetime (Figure 2.12). In

each sequential image a FA can either be born, continue into the next time step, merge or die. The birth-death-merge processes are detected by examining the properties extracted from the segmented adhesions. The results of this tracking algorithm are assignments of the FAs identified in each image into lineages that track the development of the FAs during the course of the experiment.

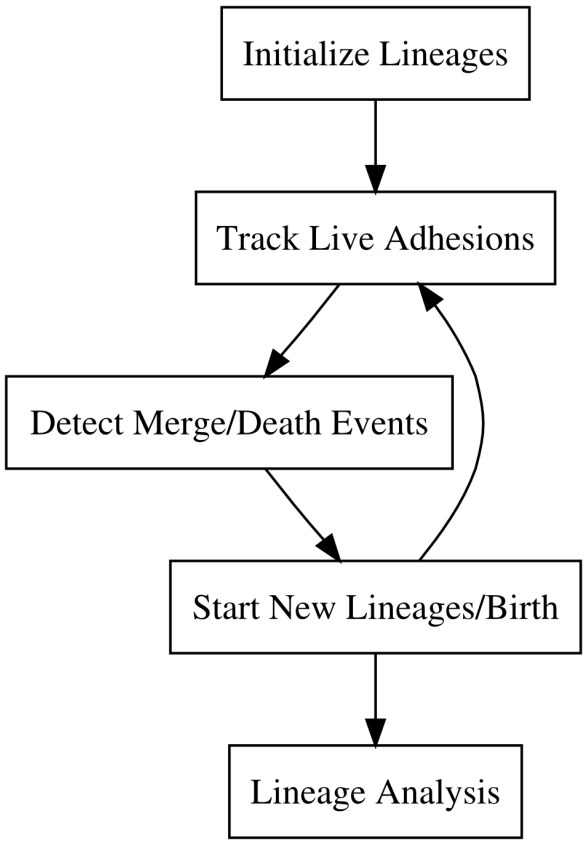

Figure 2.12: Flow chart for the tracking software adhesion following algorithm.

The tracking algorithm is initialized with all the adhesions detected in the first frame of the image sequence. The first step of the tracking algorithm attempts to locate FAs that correspond to one another in the next time step of the experimental data (Figure 2.12). This first step assumes that if a focal adhesion in the first frame overlaps with a focal adhesion in the subsequent frame, these overlapping adhesions correspond to one another. When an adhesion overlaps with more than one adhesion in the following frame, the adhesion with the greatest percentage of overlap is assigned as the match. If a FA does not overlap with any of the FAs

in the following image, the FA closest to that adhesion in terms of the Euclidean distance between each adhesion's centroid is assigned as a match. Adhesions in the next frame that are not selected via either of these methods, but still overlap with an adhesion in the current frame are marked as being created via a split birth event. Adhesion births that are the result of split events are dealt with in later filtering steps. All of the living focal adhesions are assigned a corresponding FA in the following image by these percentage overlap and centroid distance rules.

This process of assigning live adhesions in one frame to corresponding adhesions in the following frame produces sets of adhesions that are predicted to merge. Some of these merge events are true merge events where one adhesion has joined with another, while others are adhesions which die, but are erroneously assigned as merge events. When a FA does not overlap with the FA it is predicted to become, this FA is assumed to have died and its lineage is ended. These adhesions are also marked as having undergone a death, which will be used in later filtering steps. For the remaining merge events where more than one adhesion has been predicted to merge in the next frame, one of the merging FA lineages is selected to continue, while the other FA lineage is predicted to end. When the adhesions predicted to merge differ in size by at least 10%, the larger adhesion's lineage is continued. If the merging FA's sizes do not differ by at least 10%, the lineage whose current centroid is closer to the adhesion centroid in the following image is predicted to continue. By this sequence of rules, each merge event is resolved so that corresponding FAs in experimental data images are determined.

After tracking live adhesions and resolving the merge and death events, the last step involves starting lineages that correspond to newly born adhesions. New lineages are started for the adhesions that had no match in the prior frame (birth events). This process of tracking the live adhesions, resolving merge and death events and starting new lineages is repeated for each image in the experimental data sequence until adhesion data from all the images have been processed. On average 2128 adhesions were tracked for each EGFP-Paxillin cells, 8145 adhesions for each EGFP-PaxillinS178A cells and 5184 adhesions for each EGFP-FAK

cells. The differences in the average number of adhesions are due to longer experiments in the EGFP-PaxillinS178A and EGFP-FAK data sets.

2.3.5 Calculating Assembly and Disassembly Rates

With the adhesions tracked through each experiment, the characteristic properties determined for each adhesion in each frame of the time-lapse movie are collected into a set of data time series representing the properties of each adhesion through time. One type of time series follows the mean intensity of Paxillin through time, making it possible to estimate the rates of assembly and disassembly of Paxillin for each adhesion. An automated method to estimate the rates of assembly and disassembly was developed. This program automatically fits linear models to the log-transformed time series of Paxillin intensity values for both the assembly and disassembly phases of the FA life cycle.

A log-linear fitting method was adapted and extended to allow for the automated determination of assembly and disassembly phase lengths [39]. Briefly, log-linear models are fit to all the possible assembly and disassembly phases greater than or equal to a user specified minimum length. The assembly phase is assumed to occur at the beginning of the time series, whereas the disassembly phase is assumed to end with the last point in the time series. Each of the fits collected were normalized by either the first (assembly rate calculations) or last point (disassembly rate calculations) in the time series and log-transformed, as described [39].

In the second part of the algorithm, the optimum lengths of the assembly and disassembly phases were determined via a search for the maximum sum of adjusted R^2 values of the model fits. It was assumed that the assembly and disassembly phases did not overlap. In the rare cases where there are multiple combinations of assembly and disassembly phase lengths that produce the highest sum of adjusted R^2 values, the combination with the longest combined assembly and disassembly phase lengths is selected. The stability/maturity period was then defined as the length of time between the assembly and disassembly periods.

2.3.6 Results Filtering

Several filters are used to analyze the data sets collected with these analysis methods. When determining the assembly and disassembly rates, only adhesions with at least 20 Paxillin intensity time points were analyzed. This ensured that there was sufficient data available to correctly detect the assembly and disassembly rates. Adhesions whose birth was the result of a split event with another adhesion were also excluded from the assembly rate calculations, while adhesions whose lineage ended with a merge event were excluded from the disassembly rate calculation. Assembly and disassembly fits whose linear model p-values were above 0.05, indicating that the slope of the linear model was not significantly different from zero, were also excluded from the data set.

A separate set of filters was used to determine the length of each phase (assembly, stability and disassembly) in the adhesion intensity time series data. In order to estimate the length of time an adhesion spends in the stability phase, we required that both the assembly and disassembly phases be observed. In addition, the adhesion birth could not have been the result of a split event and the death of the adhesion not the result of a merge. The filter also excluded those adhesions where the p-value of either the assembly or disassembly linear model was greater than 0.05.

2.3.7 Parameter Testing

To test the sensitivity of results on parameters used for defining the threshold for adhesion detection, the minimum length of the assembly and disassembly phases and the rate of image sampling, we re-executed our analysis while varying these parameters. The threshold for adhesion detection was varied between 0.05 and 0.10, with no significant effect on the percentage change between the wild-type cells and the S178A mutant cells in either the assembly or disassembly rates (Figure 2.13 and Figure 2.14). Varying the required length for assembly and disassembly rate calculation similarly had no significant effect on percentage change between the wild-type and S178A mutant cells of the rates of assembly or disassembly

(Figure 2.15 and Figure 2.16). Finally, we tested the results of changing the image sampling rate by discarding every other collected image in the same set of experiments (Figure 2.17). Discarding half of the images did not significantly affect the assembly or disassembly rates, but did have a slight effect on the distribution of the adjusted R^2 values (Figure 2.18). From these parameter testing examples, we concluded that selection of a single set of parameters as determined by the user, provided a robust description for any of the differences between cell lines in terms of assembly and disassembly rates.

2.3.8 Software Testing

In order to test the baseline performance of the algorithms, a set of gold standard images were produced with sets of FAs having specific, predefined properties. In general, validation tests consisted of simulating a time-lapse microscope field of view that mimicked the observed properties of the adhesions (Figure 2.19A). Since our results are consistent with prior findings based on manual methods of adhesion identification, the simulated range of properties was set to be similar to those observed in the experimental data. For all simulated experiments, a Gaussian noise model (mean 0, variance of $2*10^3$) was used as a background to simulate the cell environment. These parameters were chosen as they produced distributions of short-lived adhesions that were empirically similar to those observed experimentally. Also, all simulated adhesions were circular and the same background noise model was used to perturb intensities assigned by the software to each simulated adhesion.

Three types of simulations were conducted: stationary, moving and kinetic. The stationary simulation consisted of simulating a field of view that included rows and columns of unmoving adhesions. The intensity of the adhesions were varied along the columns between mean intensities of 0.05 and 0.47 (95% of the detected adhesions in the experimental data fall between normalized average Paxillin intensities of 0.21 and 0.52). Ten different adhesion radii were simulated along the rows, varying between 0.5 and 5 pixels. The adhesions at low mean intensity values were not reliably discernible below intensity level 0.17. Adhesions above this

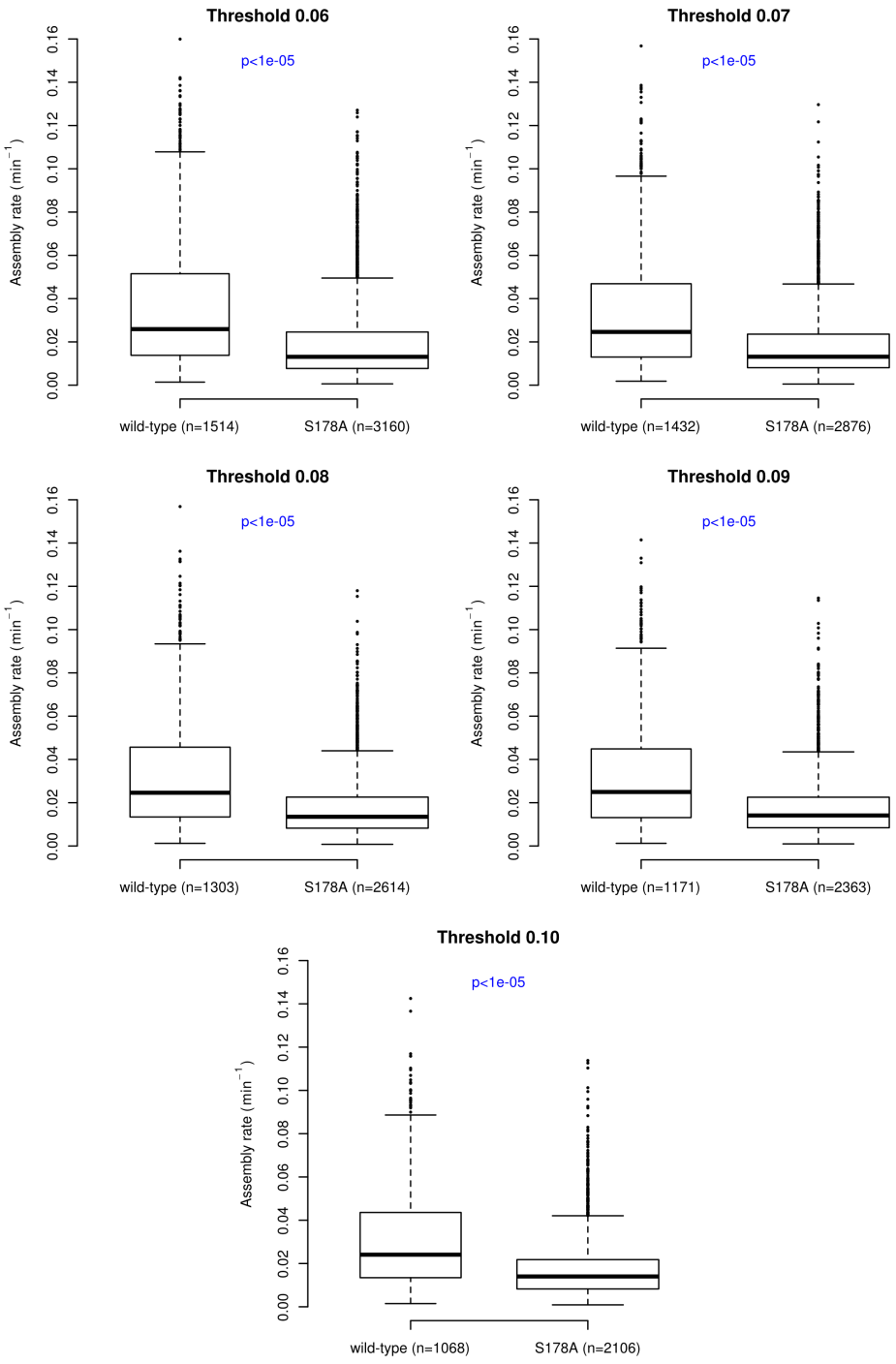

Figure 2.13: Changing the adhesion detection threshold does not affect the differences in the assembly rates between S178A mutant and wild-type cells. Each boxplot contains all the adhesions with significant linear fits (linear model p-value below 0.05). The p-values in each boxplot are for the difference in medians between the wild-type and S178A data sets in each boxplot.

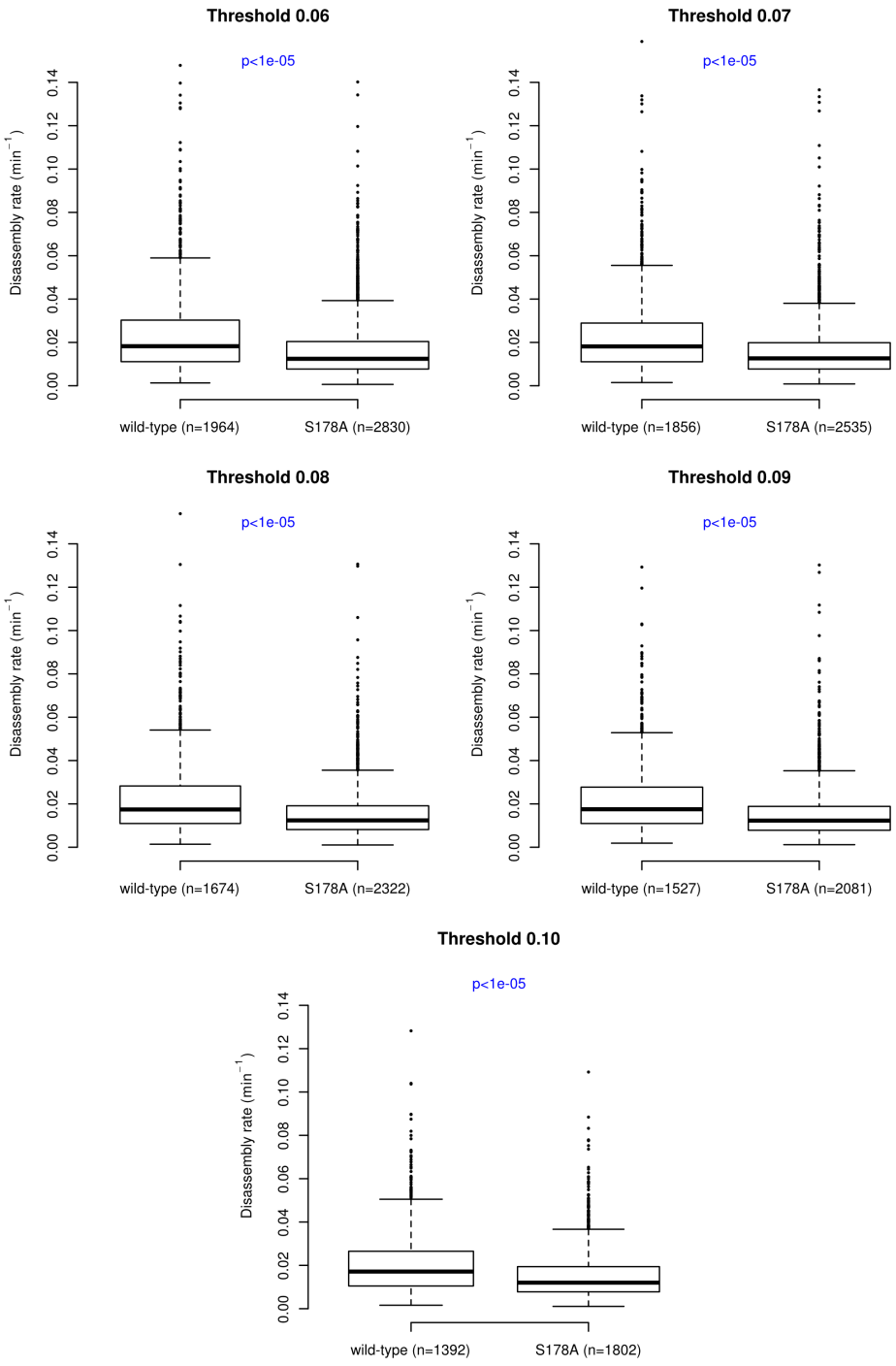

Figure 2.14: Changing the adhesion detection threshold does not affect the differences in the disassembly rates between S178A mutant and wild-type cells. Each boxplot contains all the adhesions with significant linear fits (linear model p-value below 0.05). The p-values in each boxplot are for the difference in medians between the wild-type and S178A data sets in each boxplot.

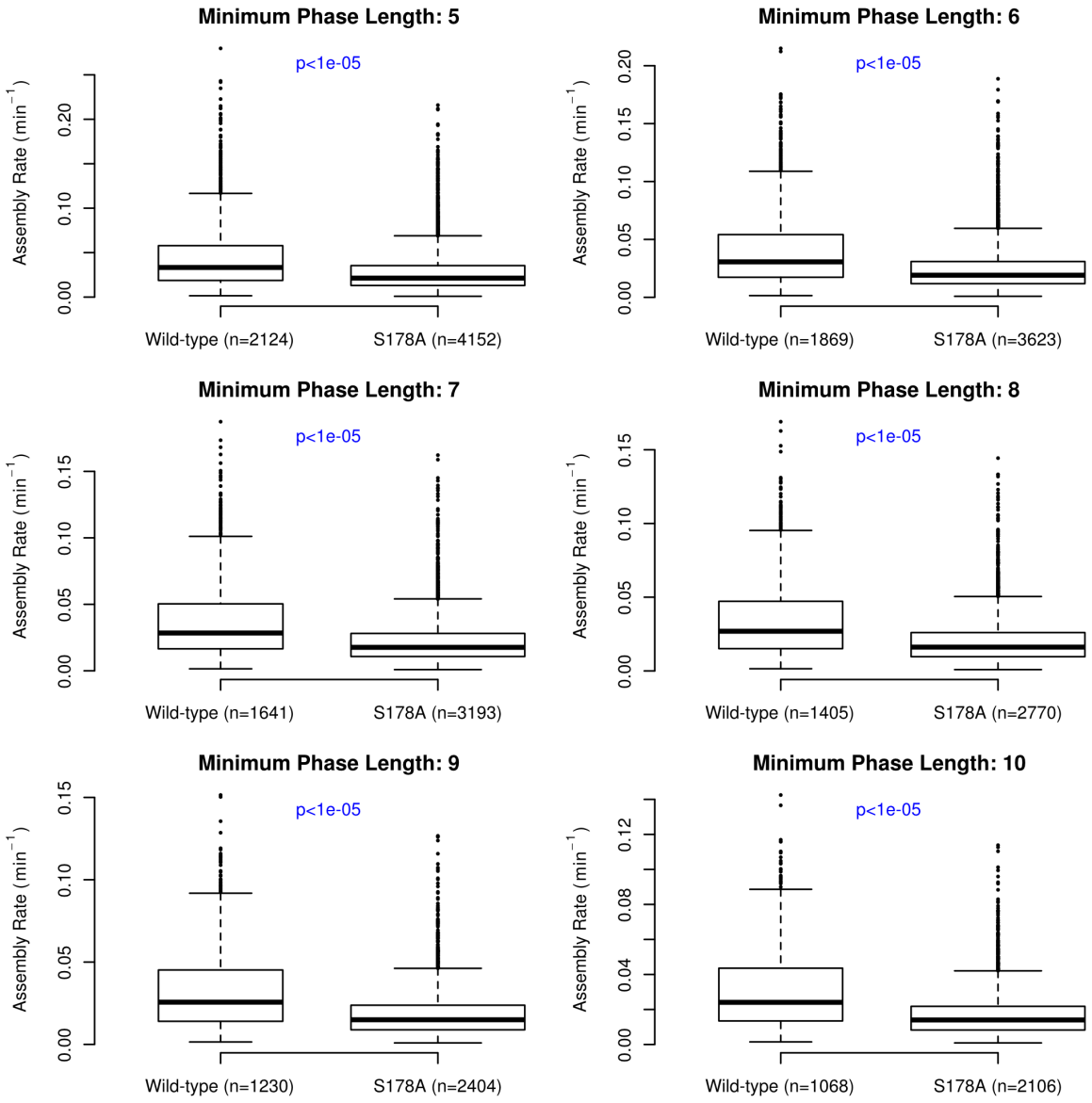

Figure 2.15: Changing the minimum length of the assembly phase does not significantly affect the differences in the assembly rate between the wild-type and S178A mutant cells. Each boxplot contains all the adhesions with significant linear fits (linear model p-value below 0.05). The p-values in each boxplot are for the difference in medians between the wild-type and S178A data sets in each boxplot.

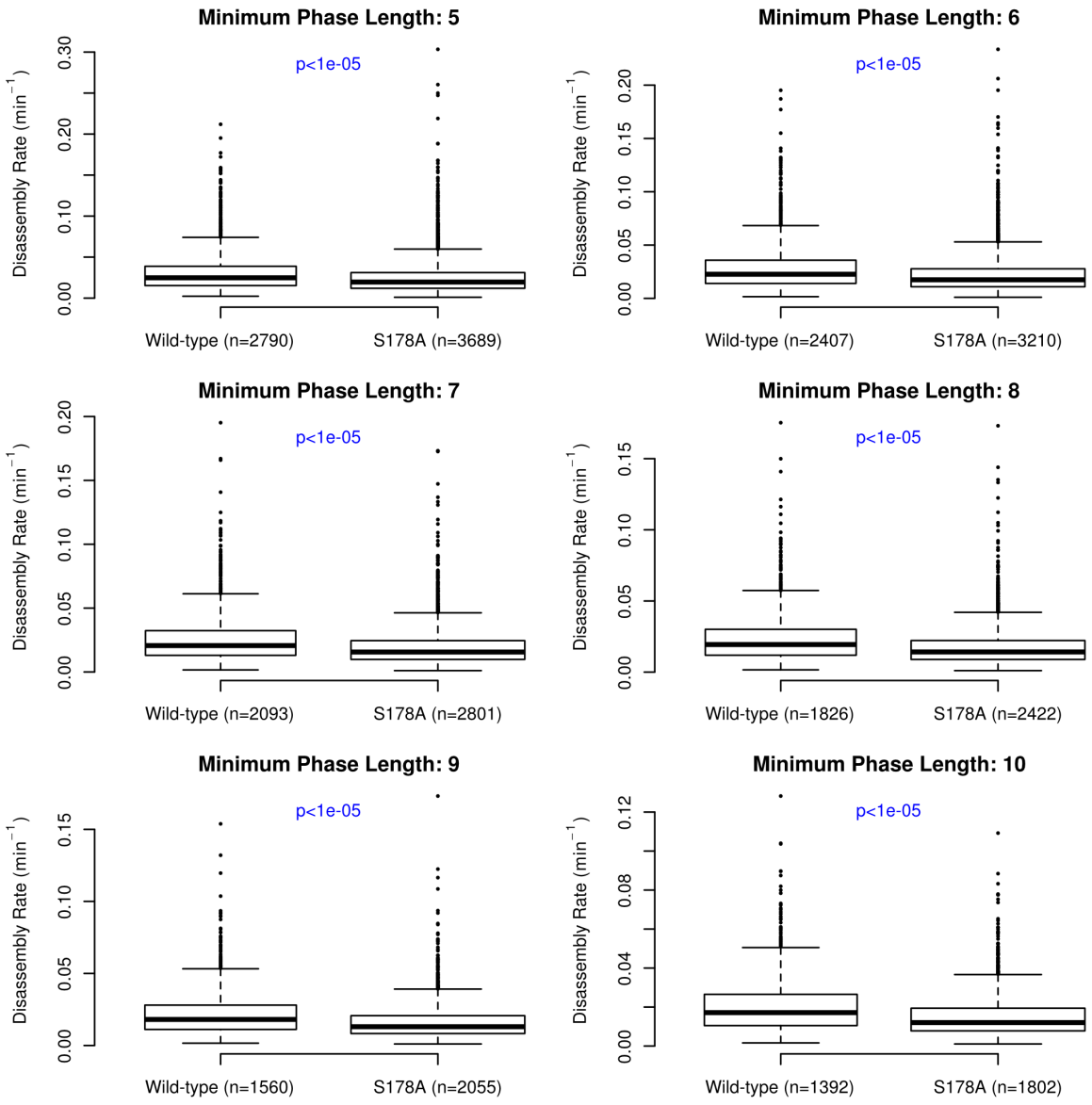

Figure 2.16: Changing the minimum length of the disassembly phase does not significantly affect the differences in the assembly rate between the wild-type and S178A mutant cells. Each boxplot contains all the adhesions with significant linear fits (linear model p-value below 0.05). The 95% confidence intervals on the percent change in the median assembly rate between the wild-type and S178A adhesions overlap in all minimum length settings. The p-values in each boxplot are for the difference in medians between the wild-type and S178A data sets in each boxplot.

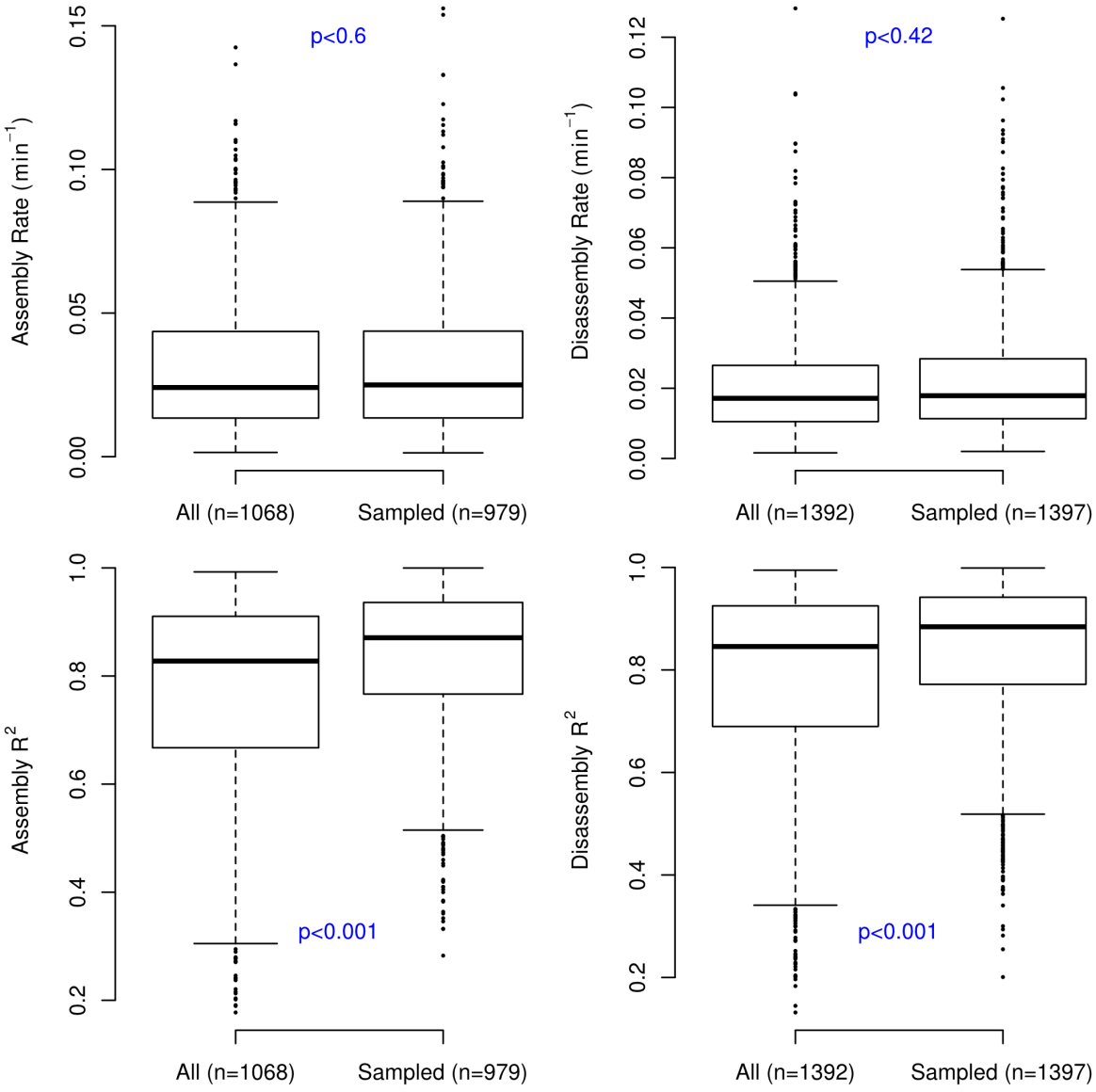

Figure 2.17: Reducing the time between each frame only has mild effects on the assembly and disassembly rates in the wild-type cells. The label "All" indicates that none of the images were excluded to estimate the rates, while "Sampled" indicates that every other image from each experiment was discarded. To compensate for the shortened experimental time, the minimum number of points needed to determine an assembly or disassembly rate was reduced to 5 for the sampled data sets. Each boxplot describes the data from all the adhesions with significant linear fits (p-value below 0.05).

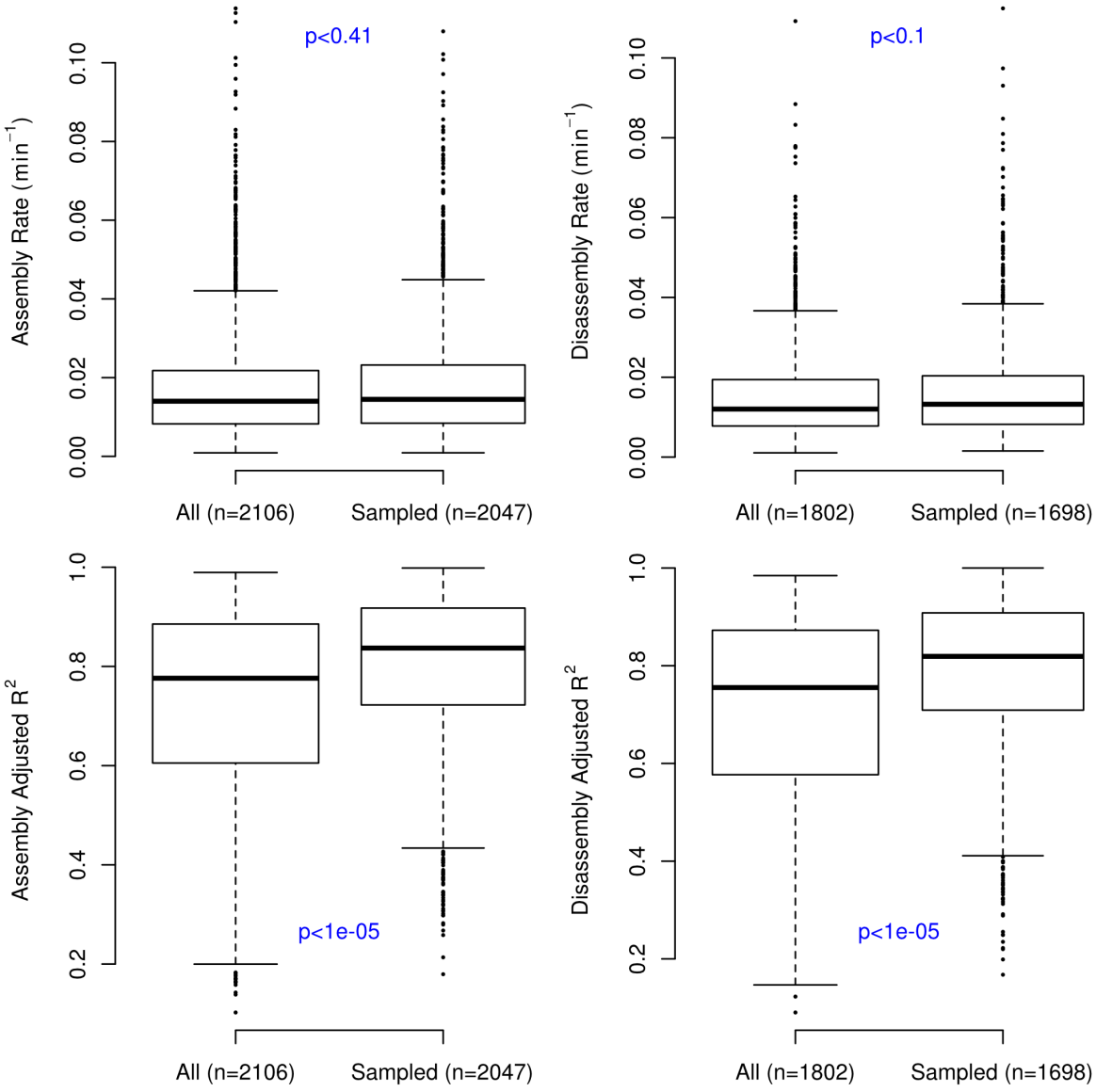

Figure 2.18: Reducing the time between each frame only has mild effects on the assembly and disassembly rates in the S178A cells. The label ”All” indicates that none of the images were excluded to estimate the rates, while ”Sampled” indicates that every other image from each experiment was discarded. To compensate for the shortened experimental time, the minimum number of points needed to determine an assembly or disassembly rate was reduced to 5 for the sampled data sets. Each boxplot describes the data from all the adhesions with significant linear fits (p-value below 0.05).

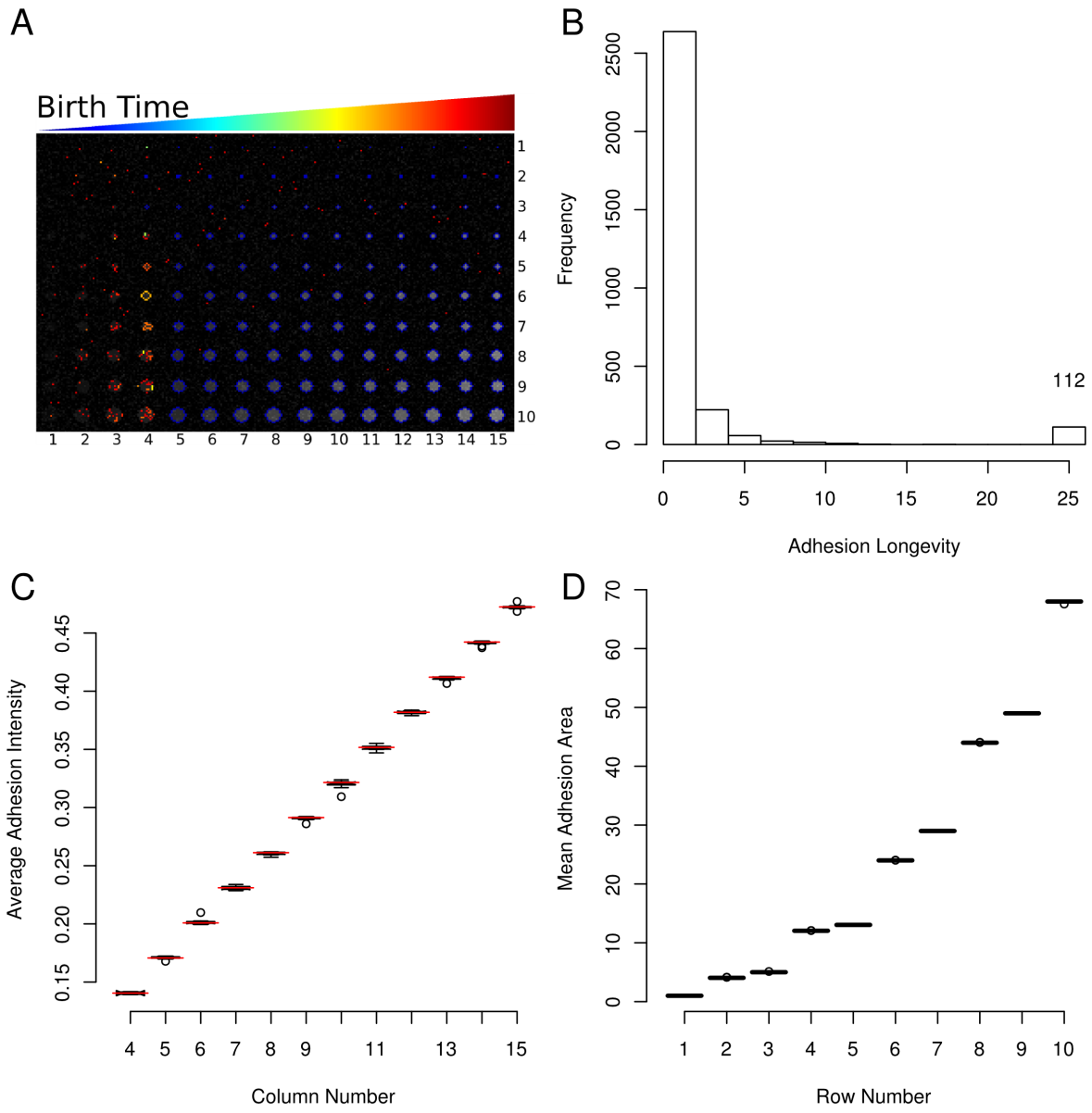

Figure 2.19: Evaluation of the analysis system's ability to extract quantitative properties from simulated stationary focal adhesions. (A) The last frame of the stationary simulation, with each adhesion outlined in a color depending on when in the movie it was born. The adhesions in blue have been detected for the longest time, while those in red and orange have been detected for the shortest amount of time. The simulated adhesions in columns 13 are all too faint to be reliably detected for the length of the simulation experiment, while those in column 4 are near the limit of detection. (B) The exponential distribution of adhesion longevity appears similar to that observed in the experimental data. The longevity of all the detected adhesions was correctly identified as 25 minutes. (C and D) The average adhesion intensity (C) and mean adhesion area (D) were correctly identified in the adhesions that were detected for their entire 25 minute lifespan. The red lines in C indicate the true values.

level were readily detected with both the predicted intensities and sizes (Figure 2.19).

The moving simulation was designed to probe the tracking algorithm's performance in following adhesions of various sizes and intensities. The simulation consisted of sliding the adhesions across the field of view at different rates (Figure 2.20A). As expected, the smaller adhesions were more difficult to track, with a nearly linear relationship between the ability to track an adhesion moving at a certain rate and its corresponding radius (Figure 2.20B). As long as the adhesion is detectable, there does not appear to be any differences in the intensity versus tracking accuracy (data not shown).

To conduct the adhesion kinetics tests, sets of adhesions were simulated that went through logarithmic assembly and disassembly phases. The assembly and disassembly rates were varied by shortening or lengthening the amount of time each adhesion spent reaching its maximum intensity. The stability period in each of these adhesions was set to five frames. Assembly and disassembly lengths between 10 and 20 were all tested. In order to avoid biasing the automated assembly and disassembly phase fitting software to higher phase lengths, the minimum phase length was set to five time points during image analysis. Overall, the software was able to reliably extract both the expected assembly and disassembly rates and length of time spent in each phase (Figure 2.21). There were several samples in the longer phase lengths that were predicted to have substantially shorter assembly and disassembly phase lengths than that specified by the software, but these simulated adhesions were in the minority and did not significantly affect the confidence intervals around the mean assembly and disassembly lengths. These simulations further support the accuracy of results derived from applying the same sets of algorithms to the analysis of adhesions in living cells.

2.3.9 Statistical Tests

Two different types of tests were used to determine the statistical significance of the differences between the adhesions in the wild-type, S178A and labeled-FAK adhesions. To compare datasets with ¡2000 points, bootstrap resampling was used to determine either the mean

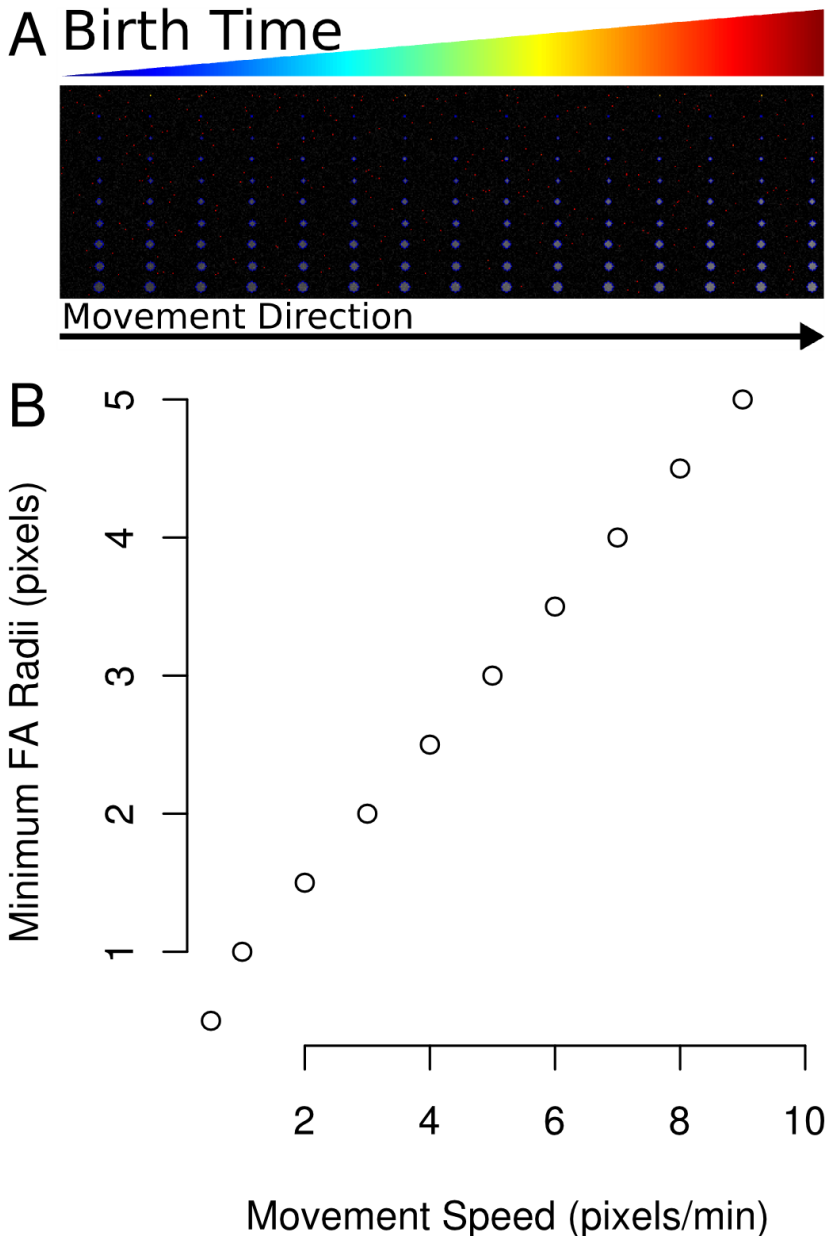

Figure 2.20: Evaluation of the tracking algorithm's ability to follow adhesions of various sizes and speeds. (A) A sample frame from the simulated adhesion motion experiment where the adhesions were moved at 1 pixel per frame. The top row of adhesions of only a single pixel could not be followed. (B) As the movement speed of the simulated adhesions increases, only larger adhesions can be reliably tracked.

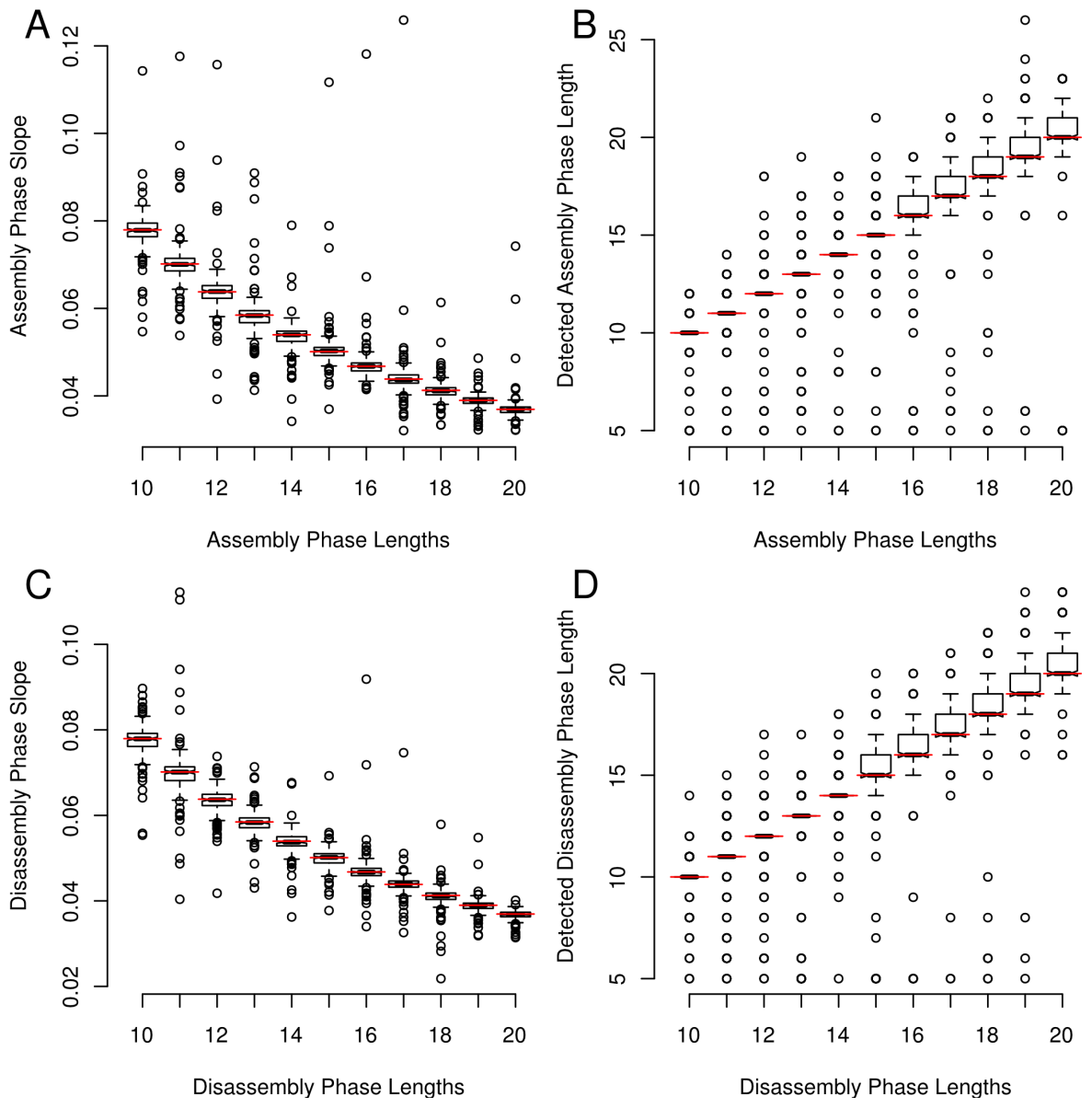

Figure 2.21: Evaluation of the rate and phase length detection algorithm using simulated focal adhesion images. (A and C) The predicted median assembly (A) and disassembly (C) rates were extracted correctly by the algorithm. (B and D) The predicted lengths of both the assembly (B) and disassembly (D) were also correctly identified by the algorithm. All the red lines indicate the expected values of the properties in each plot.

or median distribution. From these distributions the p-value was determined using the percentile method. The bootstrap method was too computationally intense to compare datasets, such as the area and axial ratio of the adhesions, with significantly more points than 2000 data points. Instead, the Wilcox Rank Sum test was used to find the p-value in these cases.

2.3.10 Software Availability

The most recent version of the software system is available from the Gomez lab website (http://gomezlab.bme.unc.edu/tools). In addition to the source code, released under the BSD license, there is a sample movie that can be used to test the success of installing the analysis system. The software has been tested on Mac OS10.5 and Ubuntu Linux 10.04.

2.4 Discussion

We have described the development of a set of computational tools suitable for the global characterization of FA spatiotemporal dynamics and assessing the results of network perturbation on adhesion properties and behavior. The S178A mutation was presented as a proof-of-concept perturbation study for the application of these tools to the analysis of complex FA phenotypes. Through this analysis, we were able to show that adhesion dynamics fall into distinct behavioral subtypes occurring in different regions of the cell, and that the S178A Paxillin mutant causes significant changes in FA assembly and disassembly. While requiring further investigation, these observations suggest a potential mechanism for the previously observed migration defects [50] and suggest that JNK, via Paxillin, may play a significant role in the control of the FA lifecycle.

The computational tools presented allow the entire FA life span to be analyzed. These tools include an automated adhesion detection, segmentation and tracking system; extracting a range of properties valuable for understanding FA development. All of these methods were tested using simulated data that replicated many of the observed experimental processes, confirming these methods are able to accurately quantify adhesion properties under controlled

conditions (see Figure 2.19, Figure 2.20, Figure 2.21 and methods). The differences detected between the wild-type and S178A mutants are robust, being preserved through a range of parameter choices for the adhesion detection limit and the minimum length of the assembly and disassembly phases. The rate at which images were taken in this work (1 sample/min) also appears to be over the sampling rate needed to accurately measure the assembly and disassembly rates of long-lived adhesions (Figure 2.17 and Figure 2.18).

Our analysis system integrates methods for automatically identifying and extracting rates of FA assembly and disassembly. We find that the assembly and disassembly rates detected using these automated methods encompass the rates determined using manual methods [39], while quantifying vastly greater numbers of adhesions. We also find that adhesions labeled with an alternate adhesion marker, FAK, also allows a similar number of adhesions to be quantified and that these adhesions are similar to those detected using fluorescently labeled Paxillin. Differences in the mean rates detected by manual versus automated searches can be attributed to several factors. First, the rates determined using manual methods originate from user-specified adhesions of interest. Such adhesions may be chosen based on specific localization properties, such as selecting only those adhesions found within particular cell regions, while the presented results do not make any distinction between adhesions present in different cellular structures a priori (though the properties of adhesions at particular locations can be determined a posteriori). In addition, due to our emphasis on observing the birth, death and taking multiple samples during the assembly and disassembly phase of an individual adhesion, our rate analysis focused on long-lived adhesions, which might have different properties than those measured in studies encompassing primarily short-lived adhesions. Finally, as our software analyzes all adhesions regardless of the brightness of the adhesion, we avoid biases that may occur through, for example, preferential selection for analysis of large or highly visible adhesions. Thus, the automated methods described here greatly extend the types of adhesions that can be readily analyzed, as well as the range of properties that can be quantified.

The spatial properties of FA birth and death suggest that FAs have distinct regions where

assembly and disassembly events are most concentrated. These assembly and disassembly regions overlap, but remain distinct. The greatest concentration of assembly events occurs within 5 μm of the cell edge. Previous studies in the same cell line indicate that this 5 μm range coincides with the end of the lamellipodia and the beginning of the lamella, where the structure of the actin cytoskeletal network changes significantly. Recently published data indicate that this transition, where stable actin structures differentiate into branched structures that exert force on the leading edge for protrusion, is determined by interactions between the cytoskeleton and adhesion proteins [56]. Further investigation will be required to more fully interpret this observation and its relation to the lamella-lamellipodium interface [57].

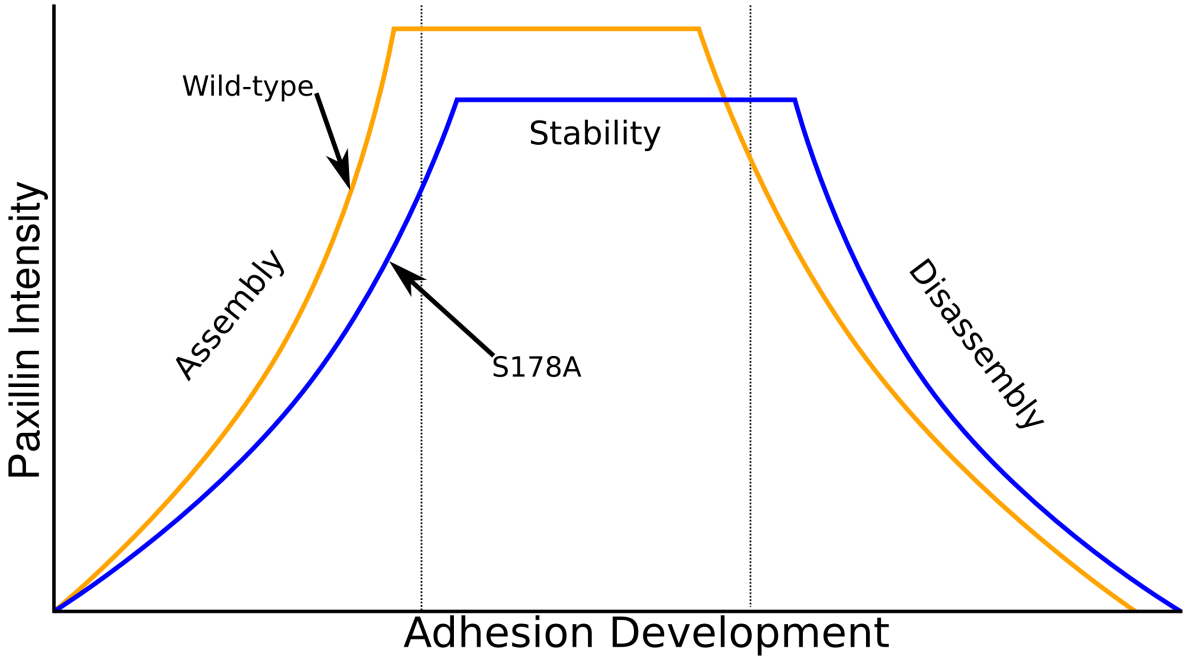

Figure 2.22: Summary of results and conceptual model of how the S178A mutant affects the adhesion life cycle. Durations and slopes are shown to scale.

Our analysis enabled us to quantify differences in FA dynamics caused by mutation of Paxillin at a JNK phosphorylation site. Both adhesion assembly and disassembly were affected. In addition to these strong perturbations, more subtle changes in FA dynamics and localization were also detected, including a decrease in adhesion size. In agreement with our results, a recent siRNA screen of FA proteins within fixed cells that included JNK knockdown

also measured decreases in adhesion size [22].

Based on our results, a summary model of the FA lifecycle in both wild-type and S178A cells is depicted in Figure 2.22. Shown to scale, the S178A mutation shows distinct effects on both the assembly and disassembly phases of FA development, but these effects are different in magnitude. Determining what FA development signals are involved in perturbing assembly, stability and disassembly is an ongoing process, but these proof of principle TIRF experiments demonstrate the capabilities of the software analysis system to make biologically significant new observations.

Chapter 3

Extensions to Focal Adhesion Analysis

The framework developed in Chapter 2 makes it possible to identify, track and quantify FA structures in living cells. These methods have provided a foundation for the development of new methods to quantify the global structure of FA organization. The FA analysis tools have been expanded through two additional projects. The first project was developed in collaboration with Zaozao Chen to identify FA structures near the cell edge without the use of a secondary marker as was used in Chapter 2 (see Section 3.1). This project also required the development of an automated method to determine the direction of cell motion without a secondary cell edge marker. The second project was developed in collaboration with James Bear's laboratory to quantify the effects of Arp 2/3 knockdown on FA (see Section 3.2). For each of these projects, I will give a brief overview of the relevant biological background and then describe the methods and results.

In addition to expanding the types of properties collected by the FA analysis system, I have also made the processing pipeline available via a web interface (see Section 3.3). The website does not require the user to download any software or have experience with a command line interface. I will describe the development of this website and show some of the interface's primary features.

3.1 Detection of Edge Adhesions and Cell Movement Direction

3.1.1 Introduction

The study of cell migration is essential for understanding a variety of processes, including wound repair, the immune response and tissue homeostasis; importantly, aberrant cell migration can result in various pathologies [35, 58]. However, the relationship between cytoskeletal dynamics, including actin network growth, contractility, and adhesion, and cell shape and migration is not fully understood.

Abl family tyrosine kinases are ubiquitous non-receptor tyrosine kinases (NRTKs) involved in signal transduction [59, 60, 61]. They can interact with other cellular components through multiple functional domains for filamentous and globular actin binding as well as through binding phosphorylated tyrosines (SH2), polyproline rich regions (SH3), DNA (Abl), and microtubules (Abl Related Gene (Arg)) [62, 63]. Abl family tyrosine kinases have also been found to regulate cell migration [63, 64]. In some cases, Abl family kinases have been reported to promote actin polymerization and migration [65] as well as filopodia formation during cell spreading [66, 67]. By contrast, in other studies, Abl was found to restrain lamellipodia extension [68, 69] or inhibit initial cell attachment to the substrate [70]. Abl family kinases have been suggested to regulate cell adhesion size and stress fiber formation [71]; Li and Pendergast recently reported that the Abl family member Arg, could disrupt CrkII-C3G complex formation to reduce β1-integrin related adhesion formation [72]. Thus, a complete understanding of how Abl family kinases regulate cell migration is lacking [63, 64].

In this study, we report that Gleevec (also called imatinib/STI571), an Abl family kinase inhibitor that is used as a chemo-therapeutic agent for leukemia, produces a profound change in the shape and migration of rat Nara bladder tumor (NBT-II) cells plated on collagen-coated substrates. To attempt to understand these changes in shape and migration, sets of EGFP-Paxillin fluorescence time-lapse images were gathered of cells treated with Gleevec and corresponding controls. The research questions related to the focal adhesions in the Gleevec

and control cells required comparisons to be made between adhesions at the leading edge, side and back portions of the cell. Since these cells would not tolerate the addition of a secondary membrane-associated fluorescent marker, new methods were developed and applied to automating the identification of adhesions in these regions.

3.1.2 Methods

To detect the cell movement direction without a cell mask signal, the location of the detected adhesions was used as a proxy. First the centroid position of each adhesion was found in each image of the time-lapse set. Then, the x and y components of the single FA centroid values were averaged, giving the adhesion centroid position. Finally, the direction and magnitude of the adhesion centroid movement was calculated between each frame of the movie and averaged over the course of the experiment to determine the overall direction of cell motion. To test the results, movement vectors were determined by hand for each set of images and compared to the automatically determined direction (Figure 3.1). There was good agreement between the automatically determined and manual direction results. This method was effective for the movies partially because none of the sample cells changed direction during the course of the time-lapse. If this were to occur, a more complicated method of combining the between frame movement direction vectors would need to be developed.

With the direction of cell movement determined, I then used the convex hull containing the identified adhesions as a surrogate for the cell edge. The adhesions in the NBTII cells used in this study generally lined the entire border of the cell, making the convex hull a good surrogate for the cell edge (Figure 3.2A). The distance from the centroid of each adhesion to the convex hull cell edge was calculated (Figure 3.2C).

With the direction of cell motion and distance from the convex hull, the adhesions were classified as either leading, side or central/trailing. To determine the position of the adhesion versus the direction of cell motion, the absolute value of the angle between the direction of cell movement and the vector formed by adhesion centroid and the centroid of each adhesion

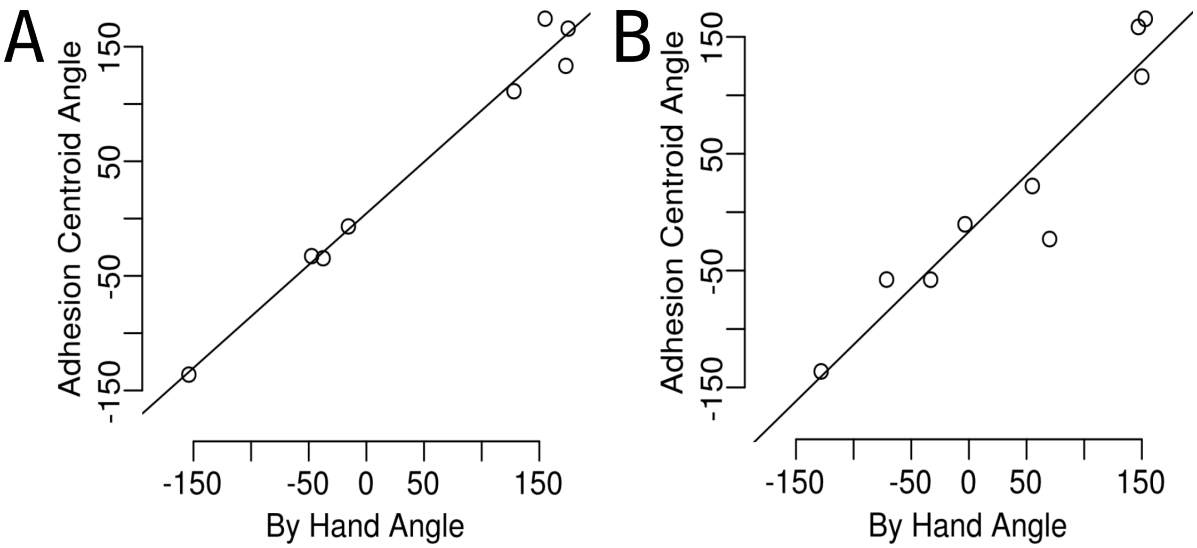

Figure 3.1: Comparison between direction of cell motion calculated manually (By Hand Angle) and automatic (Adhesion Centroid Angle) methods in control (A, n=9 time-lapse experiments) and Gleevec-treated (B, n=8 time-lapse experiments) cells.

was calculated (Figure 3.2B). This angle was near zero for adhesions close to the leading edge and became larger as the adhesion was located on the side or back of the cell. After tracking the adhesions through the rest of the movie, the average value of the convex hull distance and the angle formed with the direction of motion was determined and used to classify each adhesion as either leading, side or central/trailing (Figure 3.2D). Finally, a visualization was produced that indicates the classification of each adhesion (Figure 3.2E).

In order for this method of finding adhesions near cell edge to work correctly, the cell's adhesions must meet two criteria. First, there must be adhesions surrounding the cell edge to ensure that the convex hull does not exclude portions of the cell. Second, the cell body must not exhibit a significant number of filopodial protrusions, which would artificially extend the convex hull beyond the true cell edge. These criteria were mostly satisfied by the NBTII cells used in this study. The most problematic areas were the trailing edges of the cells, where adhesions close to the cell edge were misclassified as central (Figure 3.2C). Since the adhesions at the trailing edge of the cell were grouped with the central adhesions, I do not expect the misclassifications on the basis of edge distance to affect the results (Figure 3.2E).

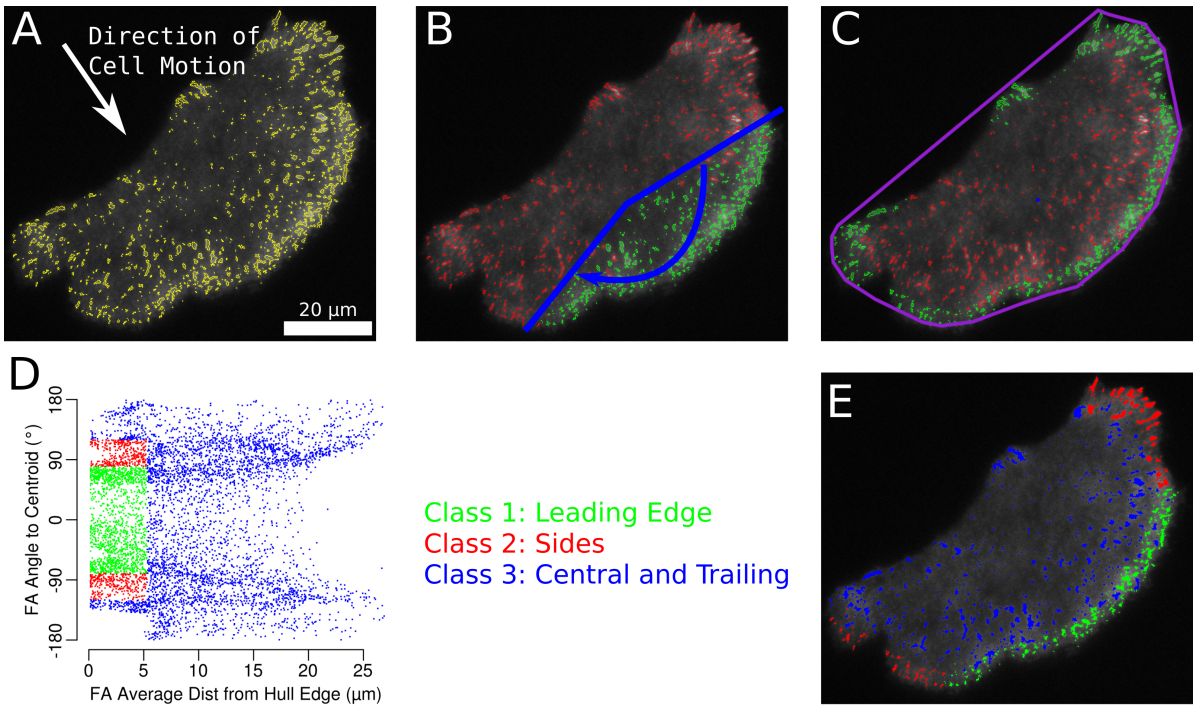

Figure 3.2: Focal Adhesion Identification and Classification Methods. (A) Sample frame from a time-lapse image sequence of EGFP-Paxillin in a Gleevec treated cell. The adhesions identified are outlined in yellow. (B) The filtering results applied to identify the leading cone of adhesions. The blue lines mark the region from -80 degrees to 80 degrees of the cell movement direction with the intersection of the two lines at the adhesion centroid. The adhesions highlighted in green are those whose average angle falls in the -80 to 80 degree threshold, while the red highlighted adhesions fall outside those cutoffs. (C) The results of filtering applied to identify adhesions near the convex hull edge. The convex hull is indicated in purple. The green adhesions are those within the 40th percentile of all average adhesion distances, while the red indicates adhesions outside the 40th percentile. (D) The distribution of adhesion angle and distance, with the corresponding classification of each adhesion in the image set. (E) Adhesions are highlighted according to the same color scheme as in part (D).

3.1.3 Results

After classifying adhesions in the control and Gleevec-treated cells as either leading, side or trailing/central adhesions, we investigated two FA properties. The first was the longevity of adhesions in the three classes; we did not find any significant differences between the longevities of the adhesions after Gleevec treatment (Figure 3.3A). The second FA property we investigated was area and significant increases in adhesion area were found in all location classes. The greatest magnitude of increase was observed in the leading adhesions, where the

average area increased by 40%, while the area only increased by 29% and 16% on the side and trailing/central adhesions, respectively. These proof-of-concept results demonstrate the utility of subdividing adhesions into classes based on their location.

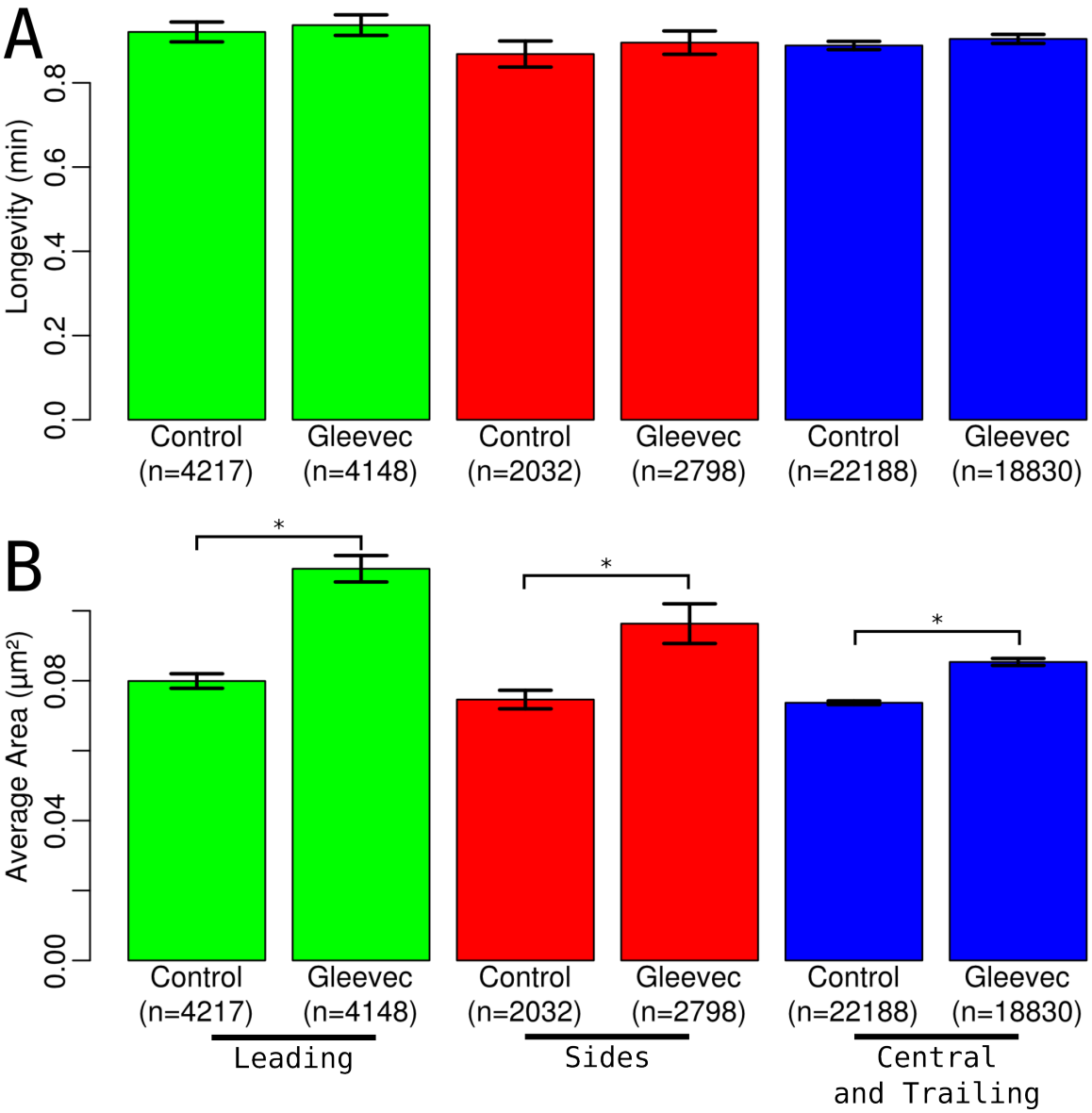

Figure 3.3: Comparison between FA Longevity and Mean Area after Gleevec Treatment. (A) The longevity of the adhesions was not affected by Gleevec treatment. (B) The average area of the adhesions was increased by treatment with Gleevec in all sections of the cell. (* $p<0.05$, t-test)

3.2 Development of Global Methods for Adhesion Direction Quantification

3.2.1 Introduction

For a cell to move in a directed fashion, it must be able to detect a difference in the external environment. The study of how cells detect the outside environment and then move in a coordinated fashion is divided into several sub-fields depending on the type of signal being detected. If the cell uses a soluble chemical factor, the migration is called chemotaxis. If the cell uses a factor attached to the surface over which the cell is migrating, then the migration is called haptotaxis. Finally, if the cell uses the mechanical properties of the substrate, such as stiffness, to determine where to migrate, the migration is called durotaxis. Understanding how eukaryotic cells sense these directional cues and respond with directed movement remains one of the central problems of modern biology.

Chemotaxis is perhaps the most well understood form of directional motility and involves a variety of signaling pathways connecting cell surface receptors to the motility machinery inside of cells [73]. Based mainly on studies of rapidly migrating amoeboid cells such as neutrophils and Dictyostelium cells, these signaling cascades are thought to trigger directional protrusions at the leading edge by controlling actin assembly pathways [74]. Haptotaxis and durotaxis are much more poorly understood but likely involve signaling events triggered by adhesive receptors such as integrins [75].

Fibroblasts are mesenchymal cells that perform a variety of tissue repair functions and respond to directional cues, such as gradients of PDGF [76]. In addition, the in vitro motility of these cells has been extensively studied. The sheet-like, protruding leading edge of fibroblasts known as the lamellipodium contains a dense array of actin filaments arranged in a dendritic meshwork [77]. Extensive experimental evidence and theoretical models of lamellipodial protrusion indicate that the polymerization of actin filaments within this meshwork drives protrusion [78]. In addition to its function in protrusion, the lamellipodium is the site of formation for most cell-matrix adhesions [37]. Integrin binding to extracellular matrix (ECM)

proteins and subsequent clustering lead to the formation of nascent focal complexes appearing continuously at the distal margin of the lamellipodium. A subset of the focal complexes mature into focal adhesions that are connected to bundled actin stress fibers.

The central pillar of the actin network found in lamellipodia is the seven-subunit Arp2/3 complex. The structure, regulation, and biochemical properties of this complex have been extensively studied in vitro (reviewed in [79]). Once activated by nucleation-promoting factors (such as SCAR/WAVE), Arp2/3 nucleates actin daughter filaments as branches off of existing mother filaments. The localization of Arp2/3 to actin filament branches in vivo [80, 77] and the functional role of this complex in lamellipodia formation in cells has been confirmed by many [81, 82, 83], but not all studies [84]. Recently, the existence of actin branches in lamellipodia has been called into question by experiments using alternate electron microscopy techniques [85].

Functional studies of Arp2/3 in vivo have been severely hampered by effects on viability observed upon loss of this complex in a variety of organisms. Genetic deletion of Arp2/3 subunits is lethal in yeast and Dictyostelium, and mouse knockouts produce preimplantation lethality [86, 87, 88]. These data led to the prevailing notion that the Arp2/3 complex is essential for viability in eukaryotes [89].

In this work, it was demonstrated that Arp2/3 is not strictly needed for eukaryotic cell viability. In mouse cells lacking the Ink4A and Arf genes, a nearly complete knockdown of Arp2/3 is possible. For the knockdown to be stable, it was necessary to target two components of the seven subunit Arp2/3 complex simultaneously. Throughout the rest of this section, the Arp2/3 knockdown cell line will be referred to as 2xKD. In addition to the knockdown of Arp2/3, a recently developed small molecule inhibitor of Arp2/3 (known as CK-666 and an inactive analog CK-686 [90]) was used to confirm the effects of the knockdown.

After developing the 2xKD cell line, a series of studies was conducted to investigate how disabling the Arp2/3 complex affects cell speed and the ability to detect chemotactic and haptotactic gradients. To test cell speed, 2xKD and NS (the control cell line, uses a non-specific

siRNA vector) cells were plated on differing concentrations of ECM components, and motility speed was measured. The results of these experiments appear in the Results section. To test the chemotactic response of the 2xKD cells, a microfluidic chamber was designed, which made it possible to create uniform quantitative gradients of Plalet-derived growth factor (PDGF). Both the 2xKD and NS cells migrated towards the PDGF source, indicating that Arp2/3 is dispensable for chemotaxis. Using the same microfluidic chamber, the haptotactic response of the 2xKD cells was tested using gradients of firbronectin, laminin, and vitronectin. Using each of these ECM components, the 2xKD cells were unable to detect the ECM component gradient, whereas the NS cells could detect and migrate up the ECM gradient. These disparate results in chemotactic and haptotactic responses inspired examination of the FAs in the 2xKD and NS cells under varying concentrations of fibronectin.

3.2.2 Results

Depletion of the Arp2/3 Complex Eliminates Cell Speed Response to Changes in ECM Concentration

Many investigators have noted that cells display a biphasic motility response when plated on different concentrations of ECM, with optimal motility occurring at intermediate concentrations [91, 92]. We tested the role of Arp2/3 and lamellipodia in this biphasic motility response. As expected, when plated on different concentrations of fibronectin (FN), NS cells displayed a biphasic motility response. However, 2xKD cells migrated at a constant, slow speed on all FN concentrations tested (Figure 3.4A). This result was confirmed with Rat2 fibroblasts treated with the Arp2/3 inhibitor CK-666 (Figure 3.4B). This loss of the biphasic motility response and the lack of cell response to haptotactic gradients led us to examine how FA structures were affected by Arp2/3 depletion.

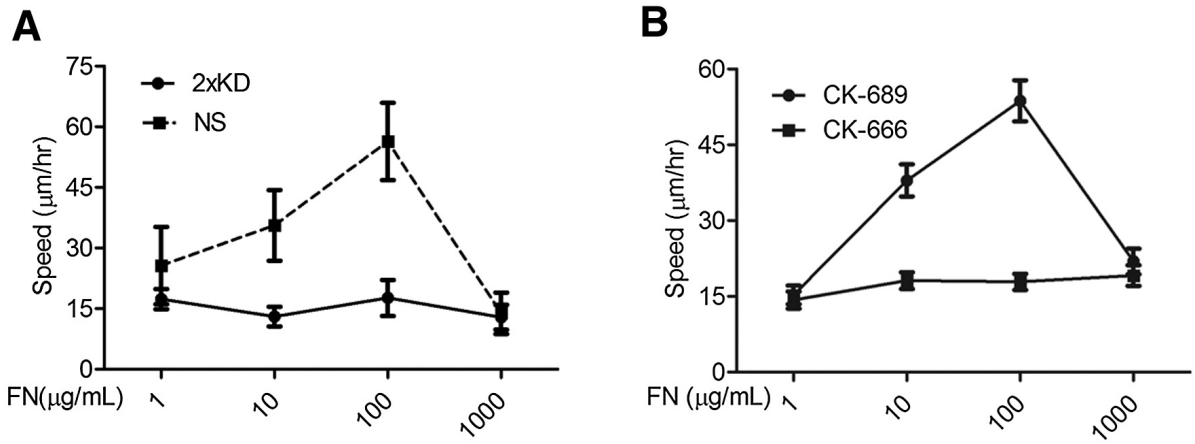

Figure 3.4: Arp2/3 Complex-Depleted Cells Cannot Respond to Concentration Changes in Extracellular Matrix(A) Single-cell speed of NS and 2xKD cells plated on different concentrations of fibronectin was plotted (N $>$ 30). Error bars represent 95% confidence intervals.

Depletion of the Arp2/3 Complex Leads to Altered Focal Adhesion Morphology and Dynamics

The defects in the ability to sense and/or respond to changes in ECM observed in the 2xKD cells suggest that cell-matrix interactions may be changed when the Arp2/3 complex and lamellipodia are absent. To address this question, we compared the distribution of focal adhesion proteins by immunofluorescence. Endogenous Paxillin (Pax), Vinculin (Vin), and FAK were all present at clearly recognizable focal adhesions in 2xKD cells (red asterisks, Figure 3.5A), although no obvious focal complexes were present in these cells due to the lack of lamellipodia. To visualize the focal adhesion dynamics, GFP-Pax was expressed in NS and 2xKD cells. Using TIRF microscopy, we observed that both cell types contained GFP-Pax-positive focal adhesions but that these two cell types tended to form adhesions in qualitatively different ways. In line with descriptions from other cell types, the NS cells generated small focal complexes at the distal margin of lamellipodia, a subset of which matured into focal adhesions. These adhesions matured in the distal to proximal direction (Figure 3.5B). In the 2xKD cells, however, the focal adhesions first appeared at the base of filopodia and reached maximal intensity quite rapidly (within 1-2 min, Figure 3.5C). Unlike in the NS cells, these adhesions grew in the proximal to distal direction. These qualitative differences in the formation of focal adhesions suggest that cells depleted of the Arp2/3 complex were utilizing

alternative pathways of adhesion assembly.

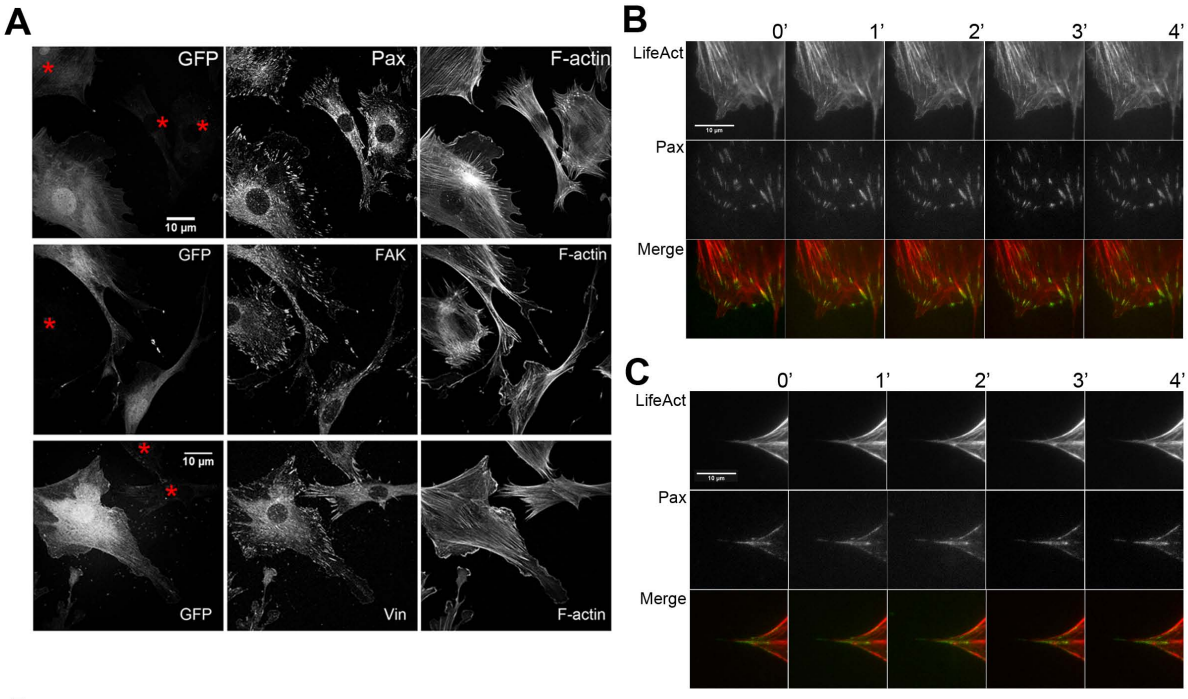

D

		Mean Area (μm²)	Mean Axial Ratio	Mean Major Axis (μm)	Mean Minor Axis (μm)	Mean Longevity (min)	Adhesions/Cell/10 min	# Adhesions	# Cells
NS	1 μg/mL FN	0.057±0.00031	2.0±0.0015	0.4±0.0007	0.2±0.0004	4.4±0.03	728.0±193.0	169735	25
	10 μg/mL FN	0.065±0.00081	2.0±0.0022	0.4±0.0013	0.2±0.0007	4.9±0.05	431.5±124.0	80552	16
	100 μg/mL FN	0.082±0.00107	1.9±0.0034	0.4±0.0020	0.2±0.0010	6.1±0.09	262.6±79.3	49154	17
2xKD	1 μg/mL FN	0.054±0.00037	2.0±0.0023	0.4±0.0008	0.2±0.0005	4.5±0.04	286.6±95.9	77917	21
	10 μg/mL FN	0.056±0.00049	2.0±0.0026	0.4±0.0010	0.2±0.0006	4.6±0.04	324.6±152.1	63260	15
	100 μg/mL FN	0.053±0.00019	2.0±0.0012	0.4±0.0004	0.2±0.0003	4.4±0.02	802.5±161.7	254105	22
Rat2	CK-689	0.057±0.00053	1.9±0.0031	0.4±0.0012	0.2±0.0007	4.7±0.07	303.1±124.1	42576	12
	CK-666	0.054±0.00048	1.9±0.0021	0.4±0.0008	0.2±0.0005	4.4±0.04	305.0±147.5	77942	20

Figure 3.5: Depletion of Arp2/3 Complex Leads to Defective Focal Adhesion Morphology and Dynamics (A) Mixed NS (expressing GFP) and 2xKD cells (marked by red asterisks) were immunostained for endogenous Paxillin (Pax), focal adhesion kinase (FAK), Vinculin (Vin), and F-actin. Scale bar, 10 μm. (B) Representative time-lapse TIRF images of an NS cell expressing GFP-Pax and LifeAct-tagRFP. (C) Representative time-lapse TIRF images of a 2xKD cell expressing GFP-Pax and LifeAct-tagRFP. (D) Table of focal adhesion parameters: NS versus 2xKD plated on 1, 10, and 100 μg/ml FN; Rat2 fibroblasts treated with CK-666 or CK-689 on 100 μg/ml FN. Numbers after the $\pm$ indicate 95% confidence intervals as determined by a t-distribution fit. See also Figure 3.7.

To quantify the parameters of the individual focal adhesions once formed in both cell types, we used a recently developed method to segment and track every focal adhesion in an unbiased manner (Figure 3.7; [93]). We analyzed the focal adhesion properties of NS

and 2xKD cells across three concentrations of fibronectin (Figure3.5D). With increasing fibronectin concentration, mean focal adhesion area and mean longevity were increased in the NS cells. Interestingly, neither of these properties varied significantly in the 2xKD cells as a function of fibronectin concentration. Mean long axis length and mean axial ratio were the same in both cell types and did not vary with fibronectin concentration. The number of adhesions per cell (per 10 min) trends in the opposite direction in NS and 2xKD cells as a function of fibronectin concentration. Control NS cells had decreased numbers of adhesions per cell with increasing fibronectin, whereas Arp2/3-depleted 2xKD cells had increased numbers of adhesions with increasing fibronectin concentration. We also examined the focal adhesions in Rat2 fibroblasts expressing GFP-Paxillin treated with the Arp2/3 inhibitor CK-666 or its inactive analog CK-689. With transient Arp2/3 inhibition, some of the same trends in focal adhesion properties were evident (and statistically significant), but these trends were much less pronounced than with RNAi-based depletion. Together these data indicate that some focal adhesion properties are unchanged by Arp2/3 depletion, whereas others are altered when Arp2/3 is depleted.

Lamellipodia Promote Global Focal Adhesion Alignment

Although the characterization of individual focal adhesion parameters is important, the ensemble pattern of adhesions is the most relevant parameter to whole-cell behavior. How cells control these ensemble or global parameters of focal adhesions is poorly understood. We observed that during spreading and after cells had fully spread, 2xKD cells had adhesions that were more radially arrayed and less aligned with each other than those of the NS cells (Figure 3.5A). One possible way adhesions could become aligned with each other is through rotation of their long axis. Although our visual impression from TIRF movies of cells expressing GFP-Paxillin strongly argued against this possibility, we tested this by plotting the average deviation in long-axis angle during the time that an individual adhesion was observed. Consistent with our visual impression, focal adhesions showed very little variation in their long-axis angle

over time in either cell type (Figure 3.6A). Thus, any change in global alignment must arise from spatially coherent formation, rather than postformation realignment.

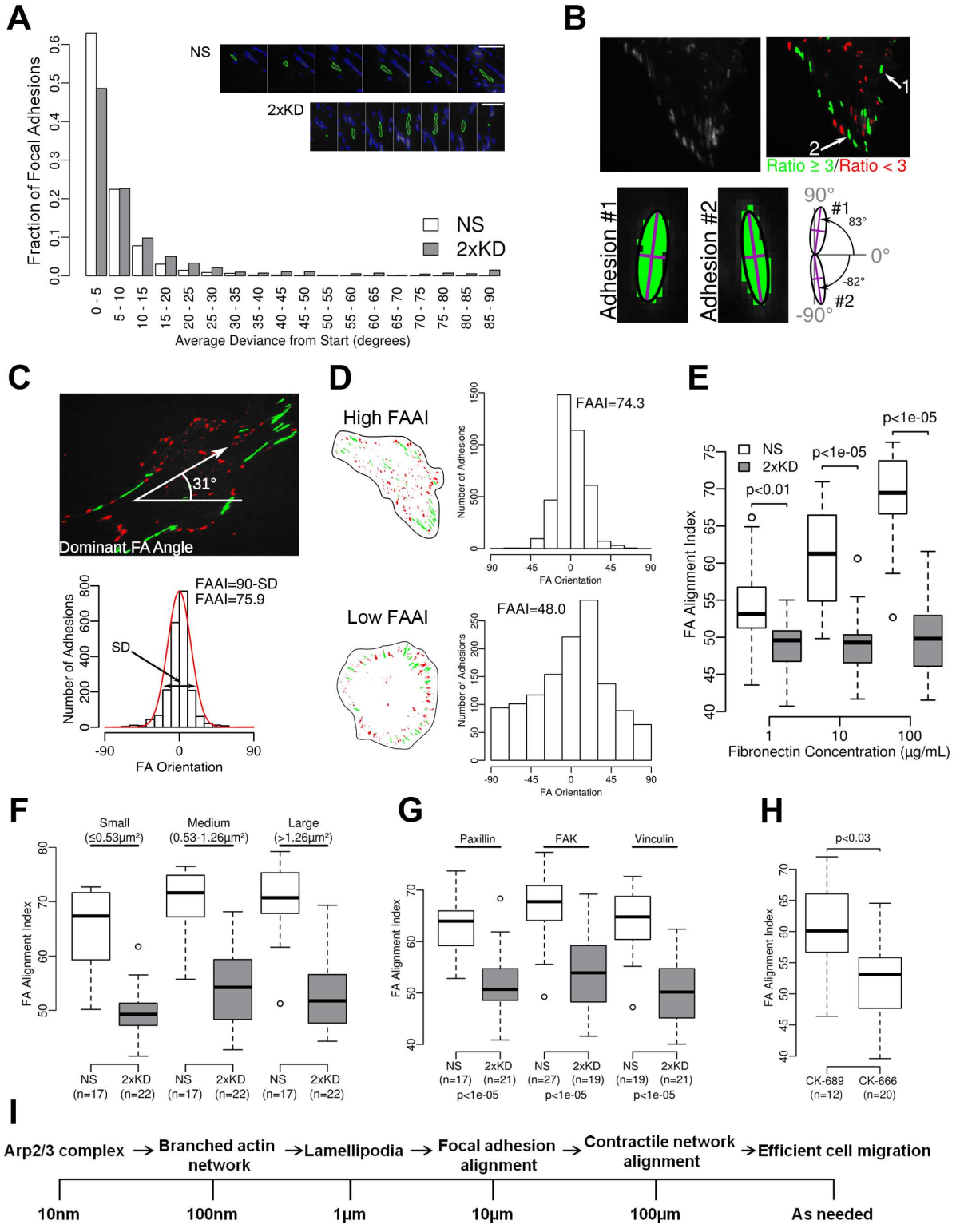

To quantify global focal adhesion alignment, we developed a method to measure the deviation of adhesion angles from the most frequent or dominant angle observed in the whole cell (see Figure 3.8 and next section). To reliably determine the angle of the individual adhesions, we limited our measurements to those adhesions with a length/width ratio of at least 3 (Figure 3.6B). By plotting the angles of all the adhesions that met this criterion, we were able to determine the most frequent or dominant focal adhesion angle by rotating the image frame of reference until the standard deviation (SD) was minimized and the peak of the distribution of angles moved close to zero (Figure 3.8B). The dominant focal adhesion angle was simply the degree to which the image had to be rotated to center the peak over zero. The Focal Adhesion Alignment Index (FAAI) is directly related to the standard deviation of this distribution; $FAAI = 90 - SD$ in order to have a higher index value correspond to more aligned adhesions (Figure 3.6C). To illustrate this measurement, a cell with high FAAI and low FAAI are shown in Figure 3.6D.

Using this metric, we quantified the FAAI of NS and 2xKD cells plated on 1, 10, and 100 μg/ml fibronectin. We observed increased alignment of adhesions across the cell (increasing

---

Figure 3.6: Arp2/3 Complex Depletion Leads to Poor Global Alignment of Focal Adhesions (A) Distribution of single focal adhesion mean deviations from their first orientation measurement starting point. The adhesions analyzed were from NS (17 cells and 3,184 adhesions) or 2xKD (22 cells and 1,132 adhesions) cells plated on 100 μg/ml fibronectin. Insets show single adhesions outlined in green over time; there are 6 min between each image. (B) Diagram showing adhesion filtering through a minimum axial ratio of 3 and two sample adhesion orientations. (C) Diagram showing the determination of dominant angle and focal adhesion alignment index (FAAI). (D) Sample single-cell cartoons showing representative high and low FAAI cells with corresponding adhesion orientation data sets. (E) FAAI of NS and 2xKD cells expressing GFP-Paxillin plated on different concentrations of fibronectin (number of cells same as in Figure 3.5D; p values for the difference between the means were calculated by bootstrapping with 10,000 replicates). (F) FAAI of NS and 2xKD cells with the adhesions grouped by size (p values for each size range$<$ 0.0005). (G) FAAI of NS and 2xKD cells expressing indicated focal adhesion markers. (n= number of cells analyzed, p values calculated same as in part E). (H) FAAI of Rat2 cells with CK-666 or CK-689. (I) Conceptual model of cell motility events across length scales. See also Figure3.8

FAAI) with increasing fibronectin concentration in the NS cells, whereas the alignment in the 2xKD cells was decreased compared to the NS cells and was constant at all fibronectin concentrations (Figure 3.6E). Because mean adhesion area showed similar trends (Figure 3.5D), we tested whether focal adhesion alignment was independent from adhesion area. To do this, we recalculated the FAAI considering only small, medium or large adhesions in the NS and 2xKD cells (Figure 3.6F). Regardless of which size adhesions we used to calculate FAAI, the same difference in alignment was observed between NS and 2xKD cells. To ensure that this result was not specific to the expression of GFP-Pax, we calculated the FAAI of NS and 2xKD cells expressing fluorescent fusions of FAK and Vinculin. With all three markers, 2xKD cells showed significantly lower FAAI compared to NS control cells (Figure 3.6G). Finally, we confirmed this result in Rat2 fibroblasts treated with the Arp2/3 complex inhibitor CK-666 and we observed decreased FAAI with Arp2/3 inhibition (Figure 3.6H). These results suggest that one of the principal functions of the lamellipodium is to promote global focal adhesion alignment.

3.2.3 Methods

Calculating the Focal Adhesion Alignment Index

To identify focal adhesions in each image of a time-lapse series, a set of segmentation methods were extended [93]. Each movie was cropped to only include one cell. Starting with the raw images from the TIRF movies (Figure 3.7A), we used a high-pass filter to minimize background noise (Figure 3.7B), and the overall distribution of pixel intensities after high-pass filtering (Figure 3.7C) was used to select a threshold for adhesion detection. For all image sets examined, we selected a threshold of the mean plus two standard deviations of the high-pass filtered pixel intensities. We then applied the threshold and connected components labeling to identify each adhesion and removed any single pixel objects identified (Figure3.7D). After identifying the adhesions, they were tracked through time using a previously published method [93], and a range of properties were collected (Figure 3.5D). All of the per adhesion

properties (mean area, axial ratio, major axis length, minor access length and longevity) were only calculated for adhesions where both a birth and death event was detected.

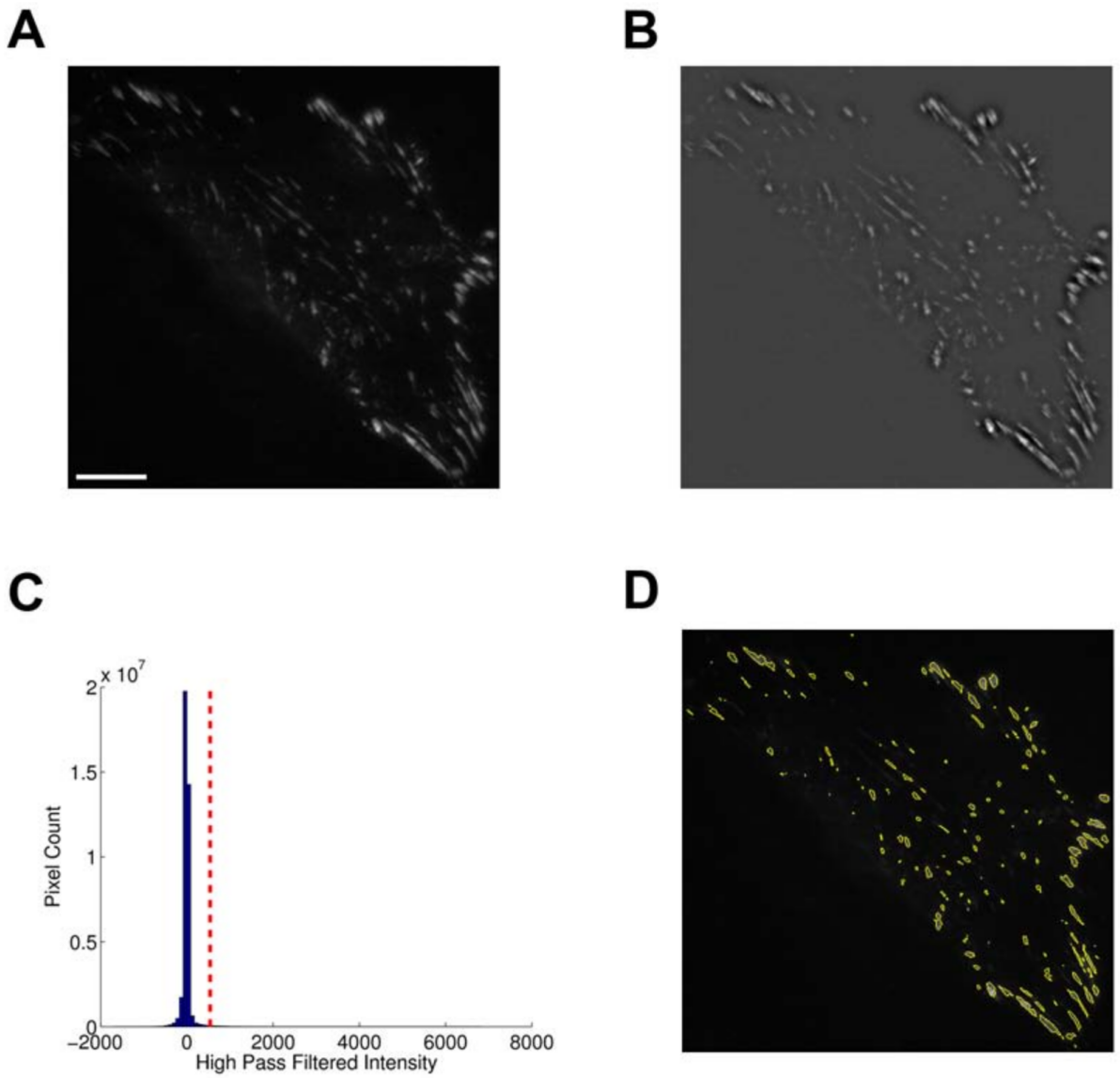

Figure 3.7: Automated Identification of Focal Adhesions. (A) TIRF image of an NS cell expressing GFP-Pax on a 100 g/ml FN-coated surface (bar = 10 μm). (B) High-pass filter applied to the image in part A. (C) Distribution of high-pass pixel intensities from the entire time-lapse image series in part A. The red dotted line indicates the focal adhesion pixel rejection threshold of the mean plus two standard deviations. (D) Locations of focal adhesions as determined by applying the threshold determined in part C to the high-pass filtered image in part B and overlaying the result on the image in part A. Each identified adhesion is outlined in yellow.

To measure the global alignment of focal adhesions across the entire cell, we developed

the focal adhesion alignment index (FAAI, Figures 3.8A and 3.8B). The index is determined by a two-step process. The first step involves collecting and filtering the adhesion angles in each image of the time-lapse, while the second step involves searching for a reference angle that minimizes the deviation between all of the adhesion angle measurements. We began the first step by segmenting the adhesions from each frame of a time-lapse movie. From this set of identified adhesions in each frame, we calculated the best-fit ellipse to each adhesion (Figure 3.8A). From this ellipse, we found the length of the major axis, the length of the minor axis and the angle the major axis of the adhesion made with the positive x axis. Angle measurement was on a scale of 90-90 to avoid the ambiguity of the 360 measurement scale (Figure 3.8A). We set the minimum ratio of the lengths of the major over minor axes to 3 as a filter to select adhesions whose orientation could be determined (Figure 3.8A). After collecting the adhesion angles with the positive x axis as the reference, the second step of calculating the index began with a search through a range of potential reference angles. The search began with the x axis as the 0 position and the calculation of the standard deviation of the adhesion angles (Figure 3.8B column 1). Then, the reference angle is increased by 0.1, the adhesion angles with the new reference axis are recalculated, and the standard deviation is measured. This search process continued until the full range (0-179.9) of potential reference angles had been sampled (see intermediate reference angles in Figure3.8B columns 2-4). The FAAI is calculated for all reference angles as follows: FAAI=90-SD(adhesion angles at a given reference angle).

We choose this formulation because it provides an intuitive interpretation of the index; high values of the FAAI indicate that the adhesions in a cell are well aligned (low standard deviation), and low values of the FAAI indicate that the adhesions are not well aligned (high standard deviation). The dominant adhesion angle is defined as the reference angle that maximizes the FAAI. In cases where there are multiple angles that maximize the FAAI, the reference angle that minimizes the absolute value of the mean adhesion angle is selected from the

A. Finding Focal Adhesion Orientations

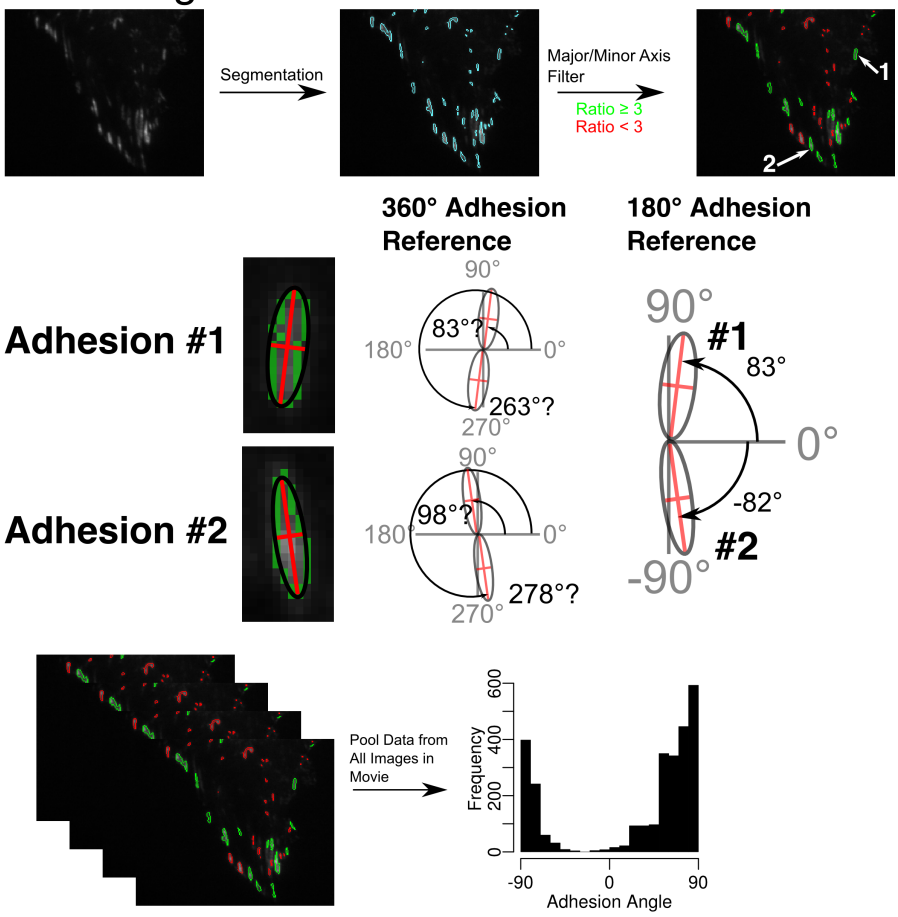

B. Dominant Focal Adhesion Alignment

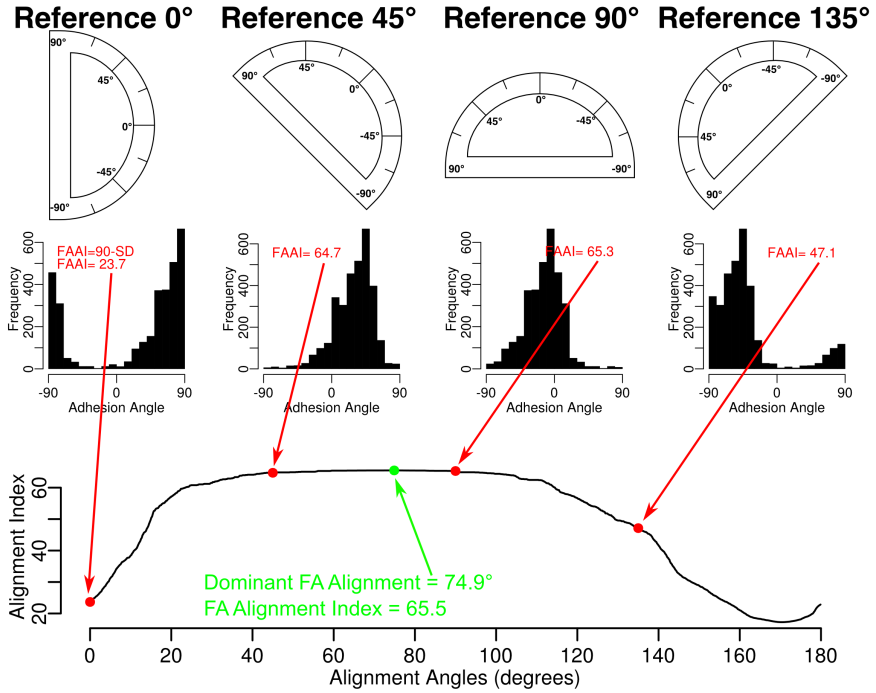

list of angles that maximize the FAAI as the dominant angle. The final number reported is the value of the FAAI at the dominant angle.

We also wanted to measure the variation through time in the angles formed by single adhesions. To measure single adhesion angle variation, we tracked the adhesions identified through each frame of the movie. From this data set of tracked adhesions, we excluded angle measurements with a major/minor length ratio less than 3 and determined each adhesion's dominant angle. We rotated each adhesion's frame of reference to match that adhesion's dominant angle and measured the mean absolute value difference between the adhesion's first measured angle and the rest of the adhesion's angle measurements.

3.2.4 Discussion

In this work, we have established a stable Arp2/3-depleted cell line that allowed us to study random and directional cell motility in the absence of lamellipodia. The depletion of the Arp2/3 complex causes striking changes in cell morphology, motility, and global focal adhesion geometry.

Spatial Organization of Cell-Matrix Adhesions and Global Cell Motility

Although focal adhesions have been intensively studied for decades, the processes that spatially organize these structures in an ensemble manner across the whole cell are poorly understood. Our results indicate that lamellipodia play a major role in bringing spatial coherence to focal adhesion formation. Without lamellipodia, focal adhesions are poorly aligned with each other, which may explain why these cells migrate slowly. An open question is how lamellipodia promote the alignment of focal adhesions. One possibility is that the retrograde

---

Figure 3.8: Derivation of Focal Adhesion Alignment Index (A) Focal adhesions were segmented and filtered to exclude adhesions with a major to minor axis ratio of less than 3 as indicated by color coding. The angle of the major axis with the positive x axis was measured and the adhesions angles throughout the time-lapse image set were pooled. (B) Sample search through the potential reference angles to determine the FAAI.

flow of actin networks in lamellipodia, which is itself spatially coherent over 0.5-5 μm length scales, could promote the alignment of the adhesions that form and mature within this flow field. However, how the alignment of focal adhesions within lamellipodia contribute to global alignment is less clear. Because the rear of the cell was once the front the cell, this alignment may reflect the history of these adhesions as born within previous lamellipodia. How cells manage to define a new axis of focal adhesion alignment upon turning will be the subject of future studies.

Our observations also provide a conceptual framework for linking events occurring at small length scales, such as the formation of branches by the Arp2/3 complex ($\sim$10 nm) to whole-cell motility at much longer length scales (100 μm) (Figure 3.6I). Branched actin networks generated by the Arp2/3 complex are the main component of the lamellipodial cytoskeleton. As we have shown in this paper, lamellipodia are critical for the alignment of focal adhesions. Cells with aligned focal adhesions will have aligned stress fibers attached to those adhesions. Because stress fibers are the main contractile structure of fibroblasts, cells with aligned focal adhesions will have more coherent contractility. We postulate that this coherent contractility will contribute directly to efficient whole-cell migration. This overall notion is consistent with our observation that a strong relationship exists between the fibronectin concentration the cells are plated on, the global alignment of focal adhesions, and their increased cell speed. Future studies will focus on testing this hypothesis in context of other 2D and 3D motility events.

3.3 Creation of a Focal Adhesion Analysis Web Application

The quantitative analysis of focal adhesion (FA) structures in motile cells commonly relies on the use of fluorescently tagged protein components and time-lapse fluorescence microscopy. Traditionally, the resulting images are analyzed using NIH ImageJ [94] or related tools, but we have recently developed a set of computer-vision algorithms designed to automate many of these analysis steps. These core methods have been documented in a prior

publication [93] and made available as an open source download; however, they require substantial expertise with the command line interface for their use. With FAAS, we have created a web application that allows users to submit time-lapse fluorescence image sets of FA proteins and have these images automatically analyzed.

The methods implemented by the analysis system have been previously used in several studies to investigate the quantitative properties of FAs in cells under various conditions. For example, adhesion static and dynamic properties were quantified with fluorescently labeled FAK, Vinculin and Paxillin [95, 96, 97]. Global, whole-cell changes to adhesion and cytoskeletal architecture when the Arp 2/3 complex is disabled have also been characterized [96]. By integrating these image analysis methods into a straightforward web application, we hope to make them more broadly accessible to the cell-imaging community.

3.3.1 Features

The primary interface is a set of webpages that allow a user to upload a stacked tiff set of images for processing. After the images are uploaded to the server, the processing pipeline is run, and the results are returned as a downloadable zip file. This results file contains all the intermediate processing steps as well as a set of visualizations. These visualizations show which regions of the cell were thresholded as adhesions and how the tracking algorithm followed single adhesions through time (Figure 3.9).

FA Properties and Visualizations

The analysis pipeline extracts and quantifies a wide range of properties. FA properties characterized in each individual image include adhesion area, marker protein intensity and the lengths of the major and minor axes. In addition to these static properties, the system also collects dynamic adhesion properties, which are quantified by recording the changes in individual adhesions between frames in the image stack. Dynamic properties currently include the FA assembly and disassembly rates [39] and the focal adhesion alignment index [96].

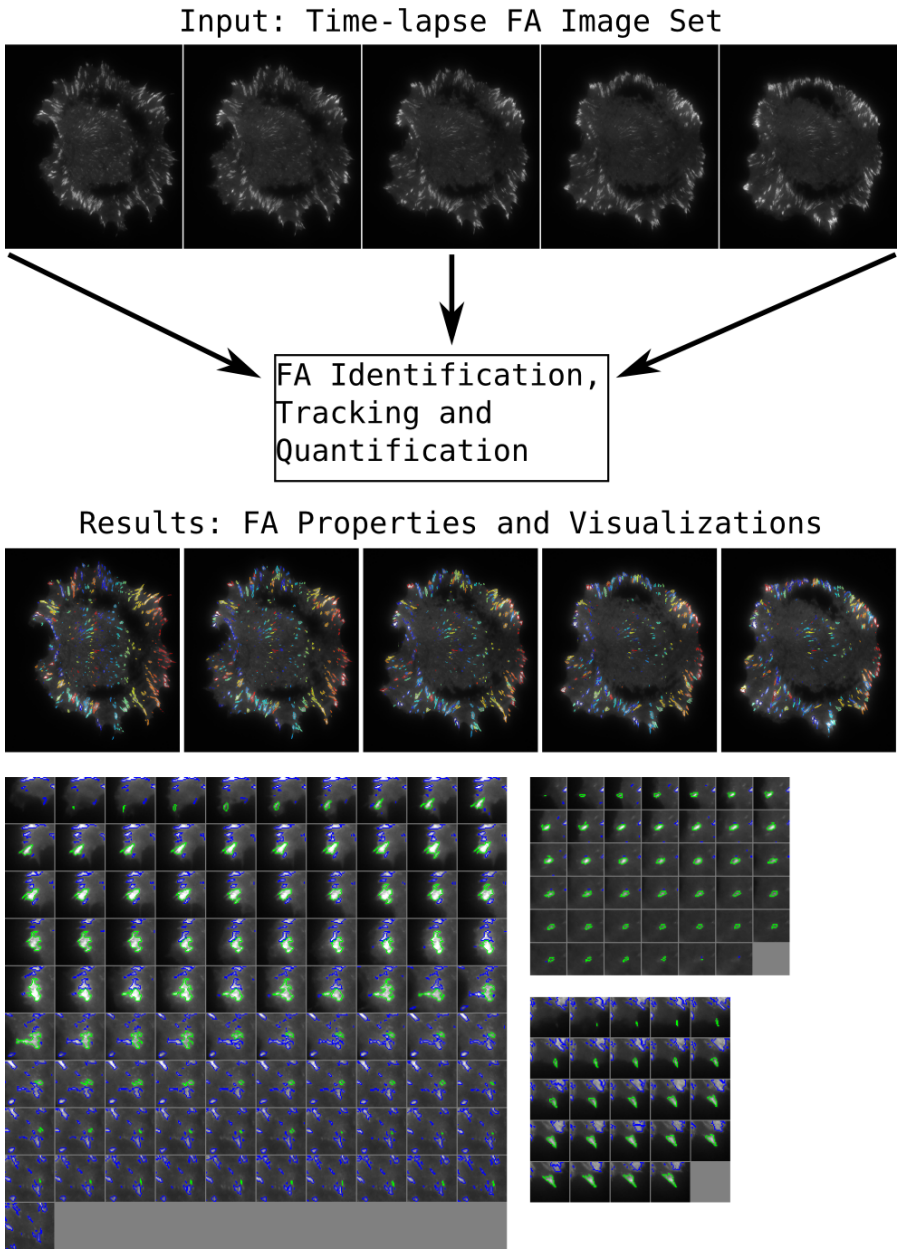

Figure 3.9: sample input images and output visualization from the focal adhesion processing pipeline. the results section shows examples from the visualizations produced by the pipeline. in the top example, the entire cell is shown, with an individual adhesion outlined and tracked through time. the bottom three examples show single adhesions, outlined in green, with other nearby adhesions outlined in blue.

All of these results are saved in CSV format, which is suitable for import into statistical or graphing software. For users only interested in static results derived from individual images, as in an analysis of a set of fixed-cell images, all the other dynamic properties can be safely ignored.

The user is also provided with two types of visualizations that show either the entire field of view or single adhesions over time. The visualization of the entire field of view is produced for every image in the submitted image set and outlines each adhesion with a unique color (Figure 3.9). This visualization can be used to verify that the adhesions were correctly detected, segmented and tracked. The second visualization type shows a single adhesion segmented and tracked through time (Figure 3.9). Provided that adhesions are present for at least 10 sequential images, this visualization allows the user to compare an individual FA's properties with the appearance of the adhesion in the original image data. This suite of automatically extracted properties and visualizations enables the user to minimize the amount of laborious manual analysis normally required to quantify FA image sets.

User Adjustable Parameters

Several of the parameters used to analyze the images can be specified when an image set is submitted for analysis. The most important of these is the threshold used to identify the regions of the image that qualify as FAs versus background. The appropriate threshold will vary depending on the type of cell imaged and the imaging conditions. To make setting this parameter easier, we have added a feature where a single image can be submitted, segmented using various thresholds and then immediately returned to the user for visual inspection of the results obtained when the threshold is varied. The user also has the option to turn off the default watershed-based segmentation that is used to split adjacent FAs and modify the minimum or maximum FA size accepted by the system. Finally, the time between images can also be specified to ensure that the calculation of the rates of assembly or disassembly are made in the correct units.

Users have the option of providing an email address when an image set is submitted. If an email address is provided, notification of the completion of the image processing pipeline, along with a link to download the results, is sent. The system can also be used without an email address, but the user must return to the web interface to check on the status of the processing. The processing time is dependent on the number of images in the set and how many adhesions are detected during processing. Using typical input data, we tested the system throughput and found that the average processing and analysis time per image, under full load, is 13 seconds. Because the system can handle four image sets at once, we expect experimental throughput to be acceptable for everyday usage.

3.3.2 Conclusion

The Focal Adhesion Analysis Server provides an automated image processing pipeline in an easy-to-use web-based application. A wide range of FA properties is automatically collected from the image sets submitted, and the results are returned in CSV formatted files. Users have the option to adjust the parameters used to process their image sets to suit their specific imaging conditions and cell types of interest.

Chapter 4

Computer Vision Based Methods for Analysis of Invadopodia in Time-lapse Microscopy.

4.1 Introduction

Metastasis is mutlistage process where cancer cells in primary tumors acquire the ability to leave the primary tumor and seed secondary tumors [98]. This multistage process begins with the migration of either single cells or groups of cells away from the site of the primary tumor and into the vasculature. To accomplish this migration, the extracellular matrix (ECM) must be degraded using matrix metalloproteinases to form paths away from the tumor site. Invasive cancer cells form specialized protein complexes called Invadopodia which actively degrade the extracellular matrix [99].

To measure degradation activity *in vitro*, quantitative imaging assays of Invadopodia behavior have been developed which use fluorescently labeled ECM to visualize regions of degradation caused by Invadopodia [100]. By combining fluorescently labeled ECM and fluorescently labelled intracellular markers of Invadopodia, such as Cortactin [101], Cofilin [102] or Actin [103], the activity of single Invadopodia can be followed through time. The time-lapse image sets produced using these methods have traditionally been analyzed using manual analysis methods which are time-consuming and potentially biased in the selection of which Invadopodia will be measured.

In order to improve the reliability of Invadopodia measurement systems, we have developed a system to automate the segmentation, tracking and quantification of Invadopodia in

time-lapse fluorescence image sets. To develop this system, we gathered time-lapse image sets of the WM2664 metastatic cancer cell line expressing LifeAct-GFP [104] forming Invadopodia in RFP labeled ECM. Since F-actin, as labeled by LifeAct, is not a conclusive marker of Invadopodia, we used the images from the labeled ECM to classify each F-actin puncta as either an Invadopodia or not based on changes in the ECM intensity over time. After classification of the puncta, we then calculate several dynamic Invadopodia properties such as longevity and the time taken to reach maximum degradation levels.

To complement the analysis conducted at the single Invadopodia level, we have also designed a system which follows Invadopodia activity at the whole cell level. This analysis uses images taken at a lower magnification (20X in our experiments) to gather a representative picture of the degradation behavior of cellular populations through time. This system was also developed using WM2664 cells expressing LifeAct-GFP and RFP labeled ECM. Using this system, we can extract the number of cells which have degraded the matrix at each imaging time point and properties of the cells with Invadopodia such as the total area degraded and the rate of degradation. Both analysis systems are available as open source packages and the single invadopodia analysis system has also been made available through the web (http://ias.bme.unc.edu).

4.2 Results

The analysis of single Invadopodia and cell populations was divided into several stages. In general, we started the analysis of either image type by developing methods to segment and track either single actin puncta or the entire cell body from image of Lifeact-GFP. After identifying either the actin puncta or cell, we then make a set of measurements of the fluorescent ECM gathered at each time point to classify the actin puncta or cell as having degraded the matrix. We then summarize properties of the identified Invadopodia or degrading cells.

To test the system and develop the appropriate thresholds for classifying single actin puncta or cells, we used several drugs with known Invadopodia activities. We used a broad

spectrum matrix metalloproteinase inhibitor, BB94, to test the system when Invadopodia degradation activity is inhibited. We also used a small molecule inhibitor of FAK, which is expected to increase Invadopodia activity. Finally, we also tested the effect of two hits from a recent fixed image screen of Invadopodia activity [23]: PP2, an inhibitor of Src Kinase, and Purvalanol A, a CdK inhibitor, both of which are expected to decrease Invadopodia activity.

4.2.1 Identification and Tracking of Lifeact-GFP Puncta

To identify Lifeact-GFP labeled puncta in WM2664 cells (Figure 4.1A), we collected a representative sample from control and BB94 treated cells. As a first step towards automating the identification of Invaodpodia, these images were manually segmented by three independent observers. A consensus segmentation was reached by majority vote from the manual segmentations, which was then used to test potential segmentation strategies and determine appropriate filters.

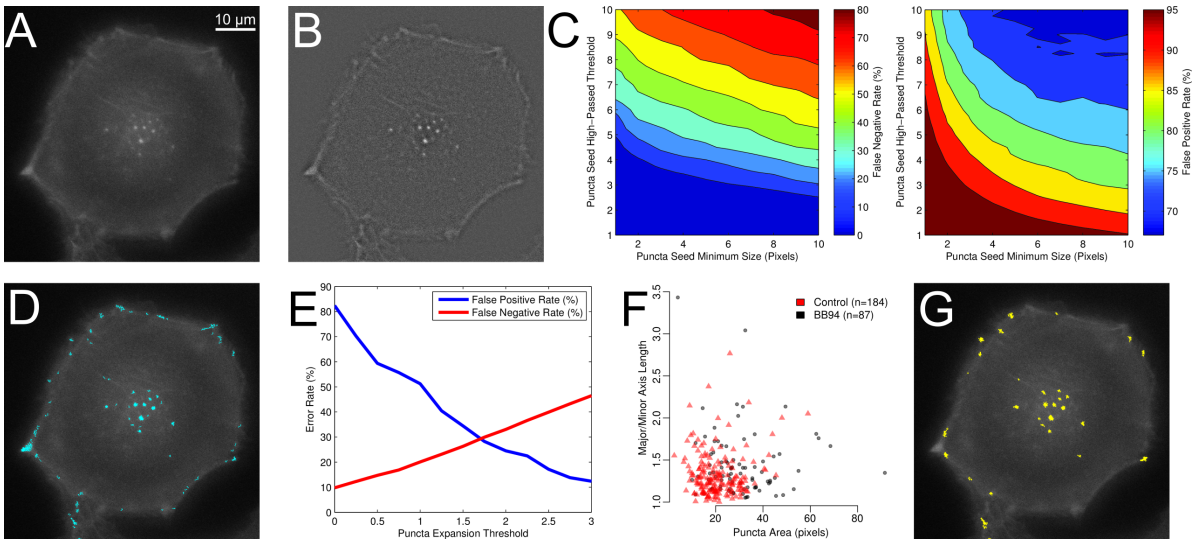

Figure 4.1: Segmentation of Puncta from Lifeact-GFP images. (A) Epifluorescence image of WM2664 cell expressing LifeactGFP. (B) Image from Part A passed through a high-pass filter. (C) Contour plots showing the detection errors for identification of puncta seeds. (D) Locations of puncta seeds accepted with minimum seed size 6 and high-passed threshold of 3. (E) Error rates on a pixel basis as a function of the puncta expansion threshold. (F) Puncta area plotted versus ratio between major and minor axes in puncta manually identified in either control or BB94 treated cells. (G) Locations of segmented Lifeact-GFP puncta based on seeding, expansion, area and major over minor axes filtering.

The first stage of the segmentation pipeline uses a high-pass filter to remove the background Lifeact-GFP signal (Figure 4.1B). Next, we determined the mean and standard deviation of the high-pass filtered pixel intensities to use as thresholds for identification of seed pixels in each puncta [96]. To test the identification of seed pixels that matched those identified through manual segmentation, we tested thresholds for the minimum seed size and number of standard deviations from the mean (Figure 4.1 C). We calculated the false positive as previously described [9]. As the puncta minimum seed size increased, the rates of false positives decreased, while the rate of false negatives increased. The same general behavior was also observed with the standard deviation threshold. We selected a minimum seed size of 6 with a standard deviation threshold of 3 (Figure 4.1D).

After identification of the puncta seeds, we also applied a second threshold that expands each of the seeds based on the local intensity of the high-pass filtered image. We tested thresholds from 0-3 standard deviation from the mean (Figure 4.1E). To assess the performance of the seed expansion procedure on identifying pixel associated with manually identified puncta, we measured the degree of overlap between the manually identified puncta and the matching computer identified puncta. As expected, as the seed expansion threshold increases, the false positive rate decreases, while the false negative rate increases. We selected a seed expansion threshold of 1.75 to balance these two factors.

Finally, we also assessed the area and ratio between the major and minor axes in the manually identified puncta (Figure 4.1F). We used the minimum and maximum values for the area and the major over minus axes ratio as filters for any objects identified after seed identification and expansion. The cell edge was also identified in the Lifeact-GFP signal using a previously published method [27]. The properties for each of the puncta identified puncta (Figure 4.1G) were then collected, which included area and the distance from the centroid of the puncta to the nearest cell edge.

Next, we tracked each puncta through the experiment, using overlap between puncta in adjacent frames to connect the segmented puncta. The majority of the identified puncta are

present for only one frame (Figure 4.2A), but there is a population of puncta that we can follow for 12 frames or more (Figure 4.2A inset). Of the puncta that live for 12 frames or more, we can quantify the average area (Figure 4.2B) and the average distance from the nearest cell edge to the centroid of the cell edge (Figure 4.2C).

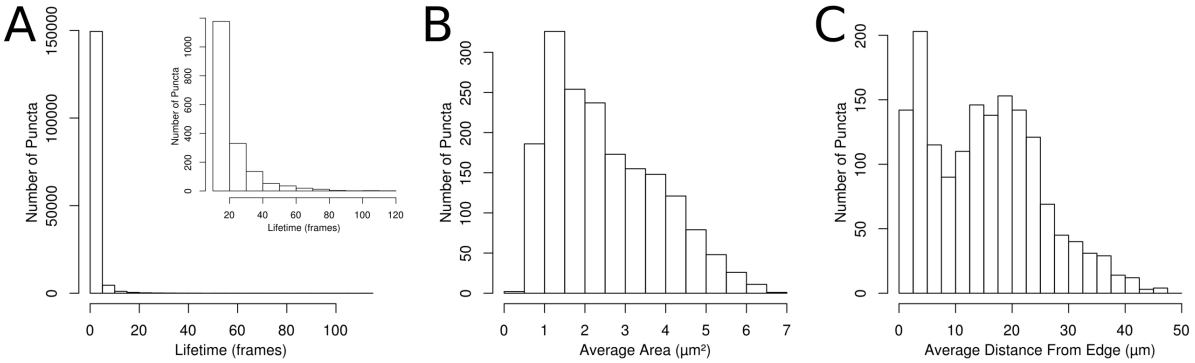

Figure 4.2: Properties of Segmented and Tracked Puncta in Control Cells (A) Histogram of the lifetime of the segmented puncta. Inset graph shows the lifetime of puncta with lifetime of 12 frames or more. (B) Histogram of the average puncta area for puncta with lifetimes over 1 hour. (C) Histogram of the distance to the nearest cell edge

4.2.2 Determination of ECM Degradation by Puncta

Degradation by individual Invadopodia *in vitro* over fluorescently labeled ECM appear as dark regions that grow as the Invadopodia degrades the ECM. In order to detect this change in the ECM, we tracked the fluorescence intensity under and in the area surrounding each detected puncta (Figure 4.3A). We collected the average ECM intensity immediately underneath each puncta and the average ECM intensity of the area in a five pixel border surrounding the puncta, exluding any area within that border occupied by another identified puncta. We take the difference between the average intensity in the surrounding ECM and the ECM underneath each puncta finding the local fluorescence difference. Puncta that have degraded the ECM will have positive values in the local fluorescence difference, while non-degrading puncta will have values near zero. We also calculate the pre-birth local fluorescence difference, which is calculated over the same pixels, but using the image immediately before the appearance of puncta. In cases where the puncta is present at the beginning of the time-lapse, we use the first image

of the ECM time-lapse. We then used the pre-birth local difference calculated at each image to correct the observed local intensity difference, giving the corrected local intensity difference.

To classify the puncta as either invadopodia or not, we analyzed the values of the local difference, pre-birth local difference and the corrected local difference. To ensure that the data from Invadopodia could be assessed, we limited our search to only those puncta present in the time-lapses for at least one hour (12 frames under our imaging protocol). The longevity filter left 2323 control, 979 DMSO treated, 294 BB94 treated, 533 FAK inhibitor treated, 83 PP2 treated and 125 Purvalanol A treated puncta. For invadopodia, we would expect the local difference and corrected local difference values to be positive (see a sample invaodpodia puncta in Figure 4.3B) and for both of these values to average around zero or negative for non-invadopodia puncta (see a sample non-invadopodia puncta in Figure 4.3C). Next, we tested whether the mean local intensity difference and the mean corrected local intensity difference were statistically different from zero using a t-test. After applying a bonferroni correction for the number of tests run, 247 control, 26 DMSO treated, 7 BB94 treated and 23 FAK inhibitor treated puncta were classified as Invadpodia. No invadopodia were detected in the PP2 or Purvalanol A treated cells. The mean local corrected difference was greater in the control, DMSO treated and FAK inhibitor treated cells as compared to the BB94 treated cells (Figure 4.3D). We manually verified that the BB94 treated puncta were false positives and excluded them from further analysis.

4.2.3 Measurement of Invadopodia Properties

Using the set of invadopodia identified in the control, DMSO treated and FAK treated invadopodia, we measured several properties. We measured both the mean area and average distance to the nearest cell edge (Figure 4.4AB). No differences were detected in the average area of invadopodia from any of the treatment groups (Figure 4.4A). The average distance

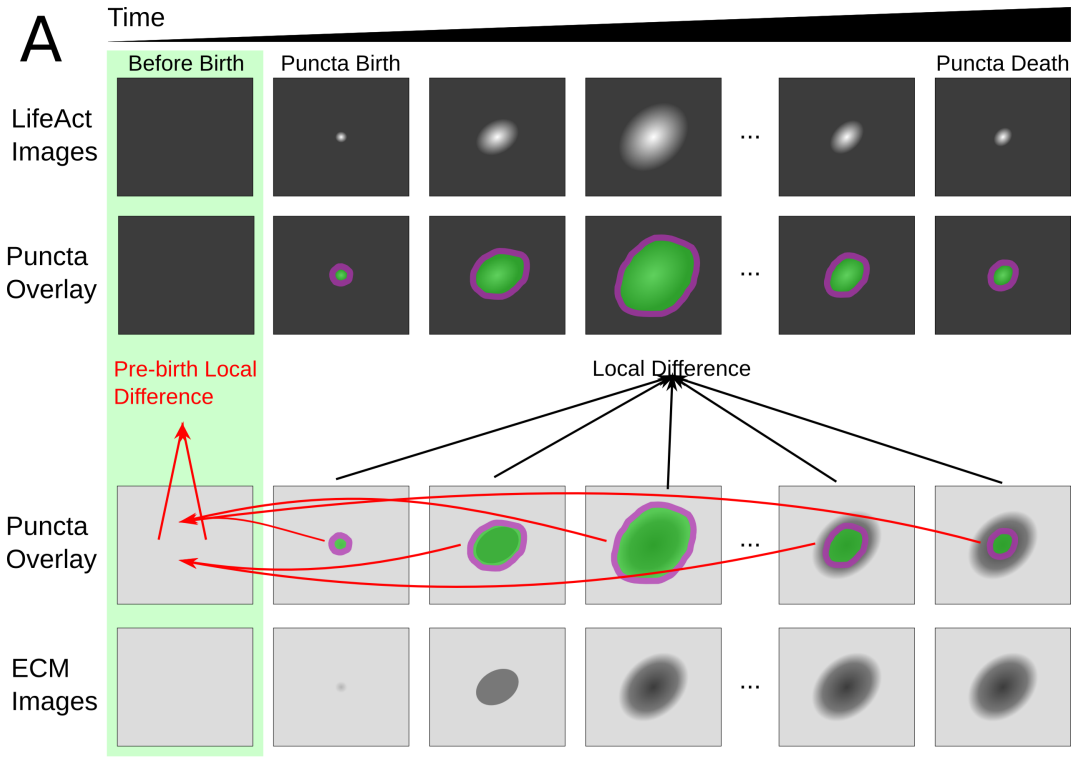
A
Time
Before Birth
Puncta Birth
Puncta Death
LifeAct Images
Puncta Overlay
Pre-birth Local Difference
Local Difference
Puncta Overlay
ECM Images

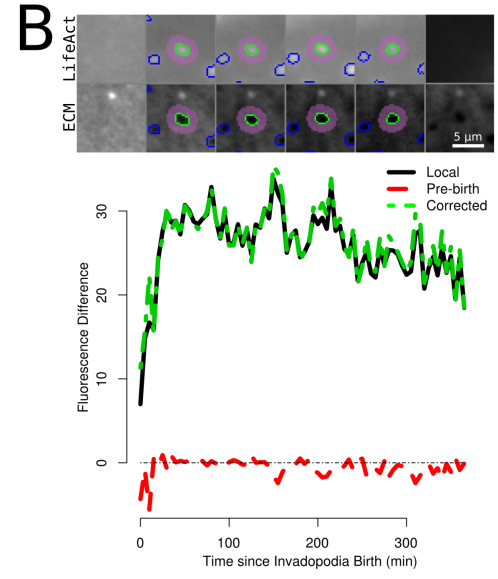
B
LifeAct
ECM
5 µm
Local
Pre-birth
Corrected
Fluorescence Difference
Time since Invadopodia Birth (min)

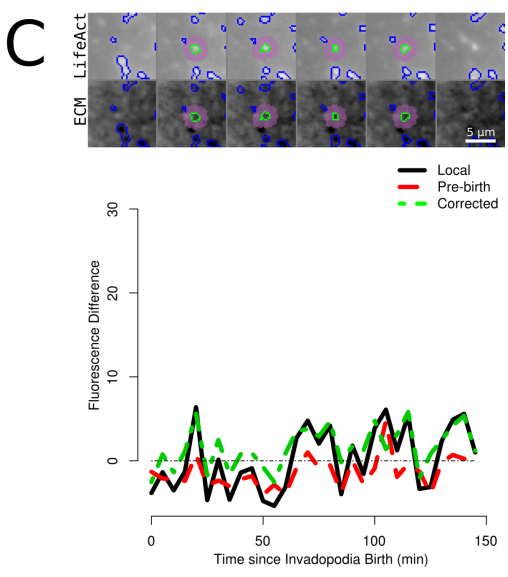
C
LifeAct
ECM
5 µm
Local
Pre-birth
Corrected
Fluorescence Difference
Time since Invadopodia Birth (min)

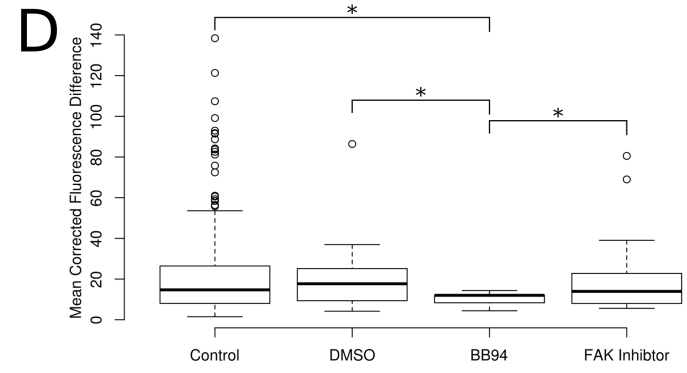
D
Mean Corrected Fluorescence Difference
Control
DMSO
BB94
FAK Inhibtor

from the cell edge decreased by 23% after treatment with DMSO and by 24% after treatment with FAK inhibitor (Figure 4.4B). We also measured the longevity of Invadopodia and found that FAK inhibitor treatment increased longevity by 45%.

We also measured the amount of time from puncta formation till the maximum of degradation level was reached. To measure this property we fit loess a smoothed curve to the local corrected difference time courses for each invadopodia. Using the smoothed values, we identified the earliest time point where the smoothed values hit 90% of the maximum. We found that this value was increased by 77% in the FAK treated cells (Figure 4.4D).

4.2.4 Identification and Tracking of Lifeact-GFP Labeled WM2664 Cells

To complement the single invadopodia analysis conducted in single cells, we have also developed a system for quantifying the ECM degradation capacity of cell populations in culture. We used WM2664 cells expression Lifeact-GFP and the same set of drug treatments to test the capabilities of the this system. After image pre-processing, we identified the cells in the Lifeact-GFP images (Figure 4.5A) using the same algorithm as was used to find the cell outline in the single Invadopodia analysis (Figure 4.5B). To minimize the number of cell clusters found we measured the areas of the single cells and multi-cell clusters found (Figure 4.5C). We then set a minimum size threshold of 1500 pixels (156 μm^2) to exclude debris and

---

Figure 4.3: Measurement of ECM degradation underneath single puncta. (A) Cartoon representation of a single puncta and the corresponding ECM underneath that degrading puncta. (B) Small multiple visualization of a single degrading puncta from a control cell and corresponding ECM intensities. The puncta is outlined in green, while the region classified as the local background is shaded purple. The first column shows the Lifeact and ECM images immediately before puncta formation and the last column shows the same areas immediately after puncta disappearance. (C) Small multiple visualization of a non-degrading puncta. (D) Boxplots of the mean local corrected difference in four of the experimental conditions. The box indicates the 25th and 75th percentiles, while the bold line indicates the median and the whiskers extend to 1.5 times the interquartile range. * indicates $p<0.05$

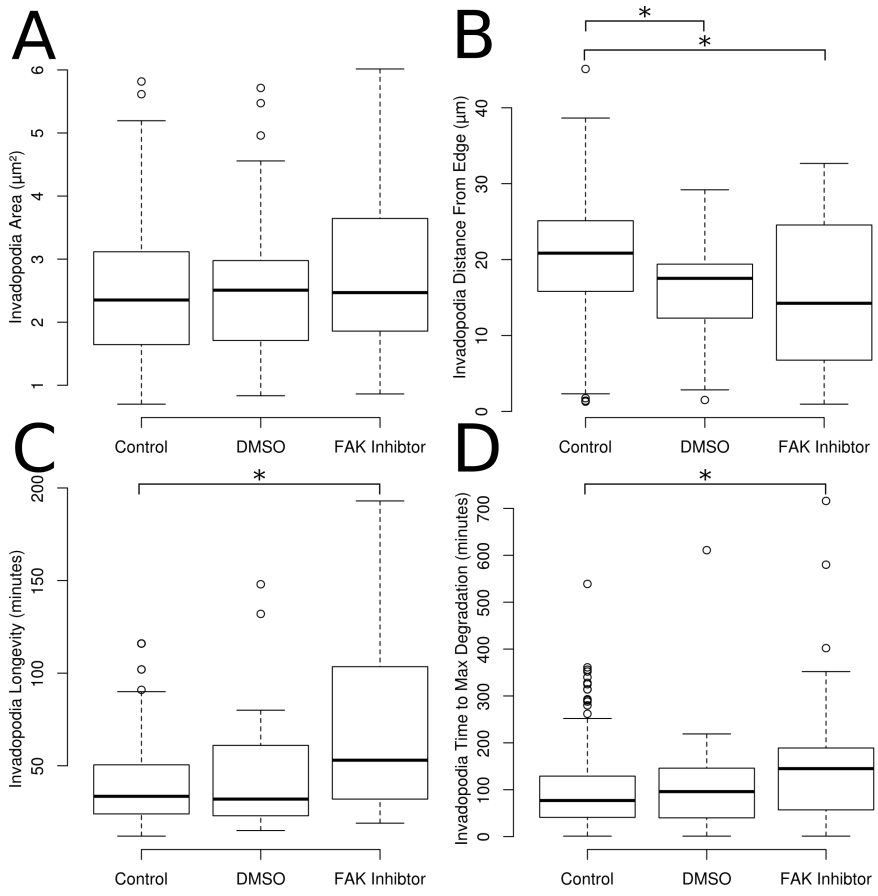

Figure 4.4: Several properties automatically extracted from the identified invadopodia. (A) The average area of Invadopodia. (B) The average distance from the cell edge of Invadopodia. (C) The longevity of Invadopodia. (D) The average time to maximum matrix degradation.

a maximum size of 20000 pixels (2087 μm^2) as filters to exclude cell clusters from further analysis. Next we tracked the cells through the experiment and found a bimodal distribution of object lifetimes (Figure 4.5D). The objects living for less than 10 hours were often non-adhered cell bodies or other debris in the field of view, so they were excluded from further analysis. Images were also taken of the fluorescent ECM (Figure 4.5E). Using the segmented cells and the intensity of the underlying matrix, we were able to observe cells degrading the matrix (Figure 4.5F).

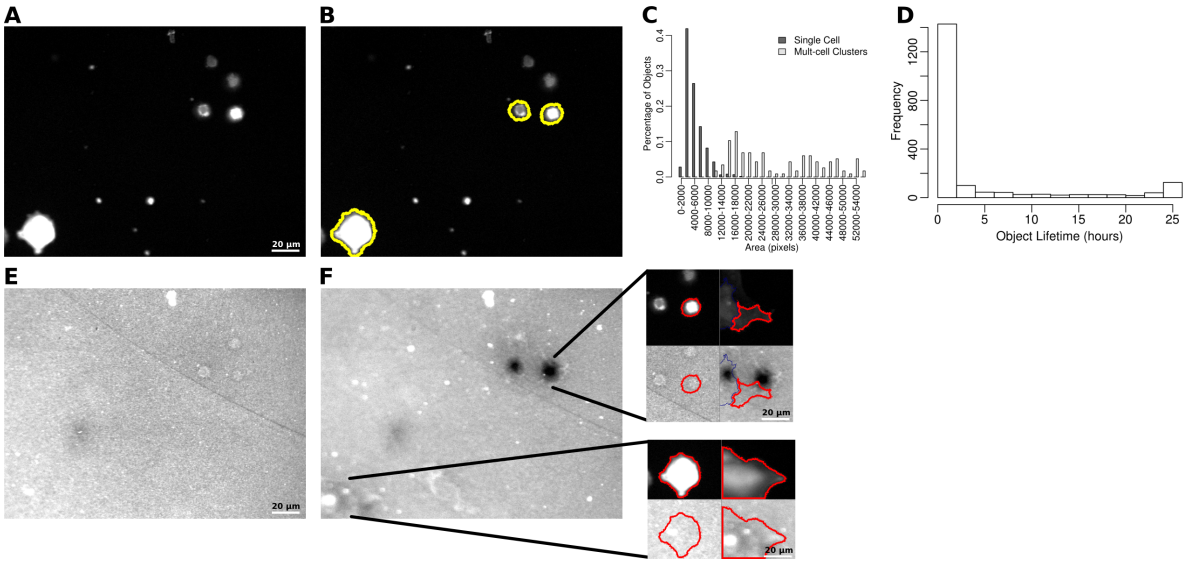

Figure 4.5: Identification of Lifeact-GFP Expressing WM2664 Cells. (A) Sample Lifeact-GFP image from a 25-hour time-lapse experiment after photobleaching and flat-field correction. (B) Same image as in part A, with the segmented cells outlined in yellow. (C) The distribution of object sizes detected based on intensity thresholding. (D) The distribution of the lifetime of objects detected in the control time-lapse image sets. (E) Sample fluorescent ECM image from the same time and field as in part A. (F) The ECM channel in the same field as in part E, at the end of the 25-hour experiment. The two sub-images show the first and last image of two cells outlined in red identified in the field. The lower portion of each sub-image shows the ECM channel immediately underneath each cell.

4.2.5 Determination of Cellular ECM Degradation

With single cells segmented and tracked through the experiment, we turned to using the fluorescent ECM images to classify cells as either degraders or non-degraders. To accomplish this, we used methods similar to the analysis of single invadopodia in the previous section (Figure 4.6A). For the identified cells in each image, we measured the average ECM intensity underneath and in a 40 pixel border around each cell, excluding any region overlapping with another cell and the corresponding regions in the prior ECM image. The average change fluorescence intensity from the prior image to current image and in the surrounding area was calculated. To allow these values to be compared across differing ECM intensity regions, we saved these values as the percentage difference between the ECM intensity underneath each puncta and the surrounding region. Thus, we would expect invading cells to have lower ECM

intensities immediately underneath the cell. We then collected time-series for each cell present for at least ten hours (example time-series in Figure 4.6B).

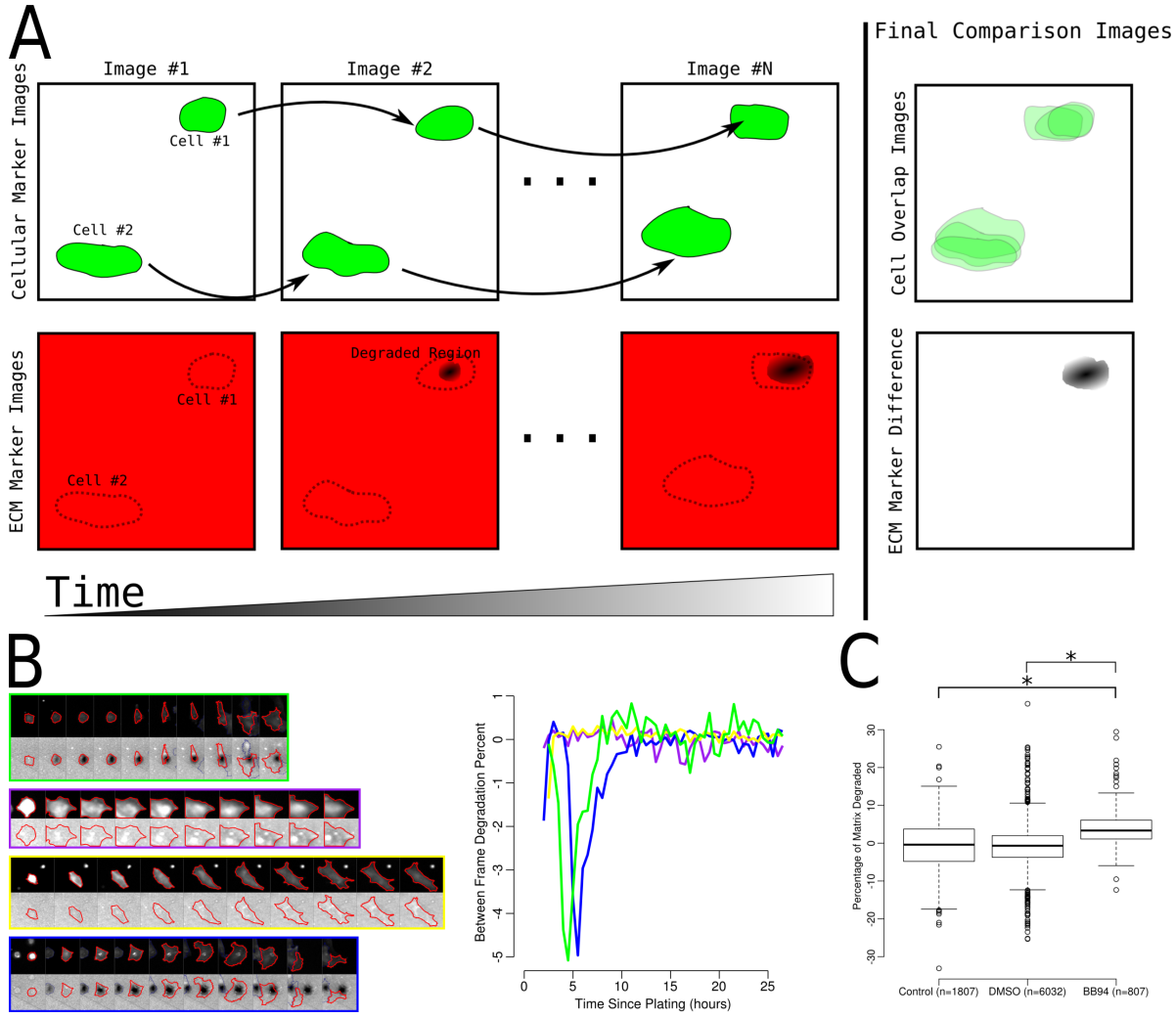

Figure 4.6: Determination of Single Cell Degrader Status. (A) Cartoon representation of two cells of which one cell degrades the matrix (Cell #1) and another non-degrading cell (Cell #2). Also shown are the overlapping areas of the cell location and the results of comparing the first and last images from the image set. (B) Example small multiple tracks of single cells through time and the corresponding measurment of the percent of matrix degraded between each image. The colors outlining each image on the left corresponds to the same color line in the plot on the right (C) Boxplots of the overall percentage of fluorescent ECM removed underneath control, DMSO treated and BB94 treated cell. * indicate $p<0.05$ via T-test

In addition to the image-by-image assessment of the percentage of the ECM removed we also assessed the overall percentage of fluorescent ECM removed by each cell (Figure 4.6C). To find the overall degradation percentage for each cell, we first determined the area of influence for each cell, by finding the amount of time the cell covered each pixel location in the field of view. Any pixel location covered for at least 2.5 hours was considered in that cell's area of influence. We then calculated the change in fluorescence intensity from the first image of the ECM time-lapse and the area surrounding the cell in the same manner as when calculating the percentage change from image to image.

With the between images and total ECM degradation percentages calculated, we classified each cell as degrading or non-degrading on a per image basis. The BB94-treatment is expected to block all matrix metalloproteinase activity, so we used the degradation percentages found in the BB94 cell as our negative control. We empirically assessed the potential cutoff values to minimize the number of false positive BB94-treated cell degrader classifications.

4.2.6 Measurement of Invading Cell Properties

With each cell classified as a degrader or non-degrader, we summarized the percentage of cells classified as degrader or non-degrader at every half hour interval during the experiment (Figure 4.7A). In general, treatment with the FAK inhibitor tended to increase the percentage of degrading cells, while Purvalanol A decreased the percentage of degrading cells. We detected only eight degrading cells under BB94 treatment and excluded those cells from further analysis. Next we measured the amount of area degraded by each cell. To find the degraded regions of the matrix, we compared the first and last images of the time-lapse, any region where the intensity had decreased by 20% was marked as degraded. We assigned these degraded areas to each cell according to the area of influence (Figure 4.7B). FAK inhibitor significantly increased the area degraded by each cell (62% increase compared to DMSO treatment), while PP2 and Purvalanol A each decreased the average area degraded (61% decrease compared to DMSO treatment). We also measured the rate of area degradation by dividing the total area

degraded by the cell lifetime (Figure 4.7C). For this property we observed similar trends to the total area degraded with FAK-inhibitor-treated cells having a higher rate of degradation (23% increase compared to DMSO treatment), while in the PP2-treated cells and Purvalanol A-treated cells there was a decrease in the rate (37% and 43% decreases compared to DMSO treatment).

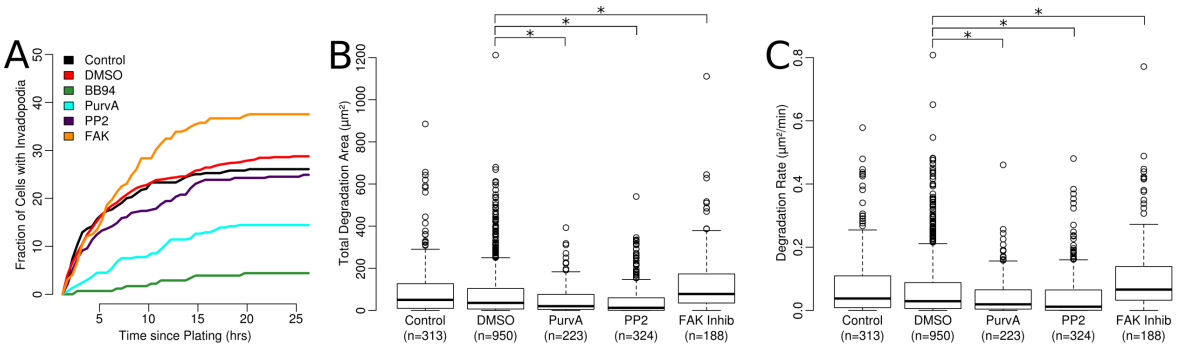

Figure 4.7: Properties of Degrading Cells (A) Percentage of cells classifed as degraders through 25 hours. Percentages are averages from several experiments(n=5 control, n=2 BB94, n=14 DMSO, n=4 PP2, n=3 Purvalanol A and n=4 FAK Inhibitor) (B, C) The total area and rate of degradation from each cell classified as an invader, * $p<0.05$ via T-test

4.3 Methods

4.3.1 Cell Culture and Imaging

WM2664 cells with stable Lifeact-GFP expression were used for all experiments. Porcine gelatin was used as the ECM for all experiments and was labeled with Alexa fluor 568 using a kit from Life Technologies (Catalog #A-10238), following all instructions. Fluorecent ECM was coated onto glass Bioptech or MatTek dishes following previously published protocol [100]. All imaging for the single Invadopodia experiments was conducted using a 60X objective with images taken once every five minutes. Imaging for the cell population experiments were conducted in a temperature and CO_2 controlled Olympus Vivaview microscope with the 20X objective. Images were taken every 30 minutes from 25 predetermined positions from each dish.

4.3.2 Image Pre-Processing

Before analyzing any of the fluorescent ECM images, the images were photobleach corrected. To ensure that the degradation of ECM was not incorrectly identified as photobleaching, only pixel outside the cell bodies were considered when photobleaching correction was applied. Next, the images were flat-field corrected. Next the single cell time-lapse images were registered (the cell population movies did not require registration). In the ECM images used for the single invadopodia analysis, the average fluorescence outside the cell bodies was set to 1000 to allow the local difference values to be compared between ECM preparations. The Lifeact-GFP images for the single invadopodia analysis were not pre-processed. The Lifeact-GFP images for the population analysis were flat-field corrected.

4.4 Discussion

We have presented a framework for the quantitative analysis of Invadopodia behavior in single cells and in cell populations over time. The system for quantifying single Invadopodia uses Lifeact-GFP to segment, track and measure the properties of Invadopodia in single cells through time. To complement this analysis system, we have also developed methods to quantify the degradation capability of cell populations through time. Both of these systems were tested using the WM2664 metastatic cancer cell line and a set of small molecule Invadopodia effector drugs. From this set of images, several dynamic quantitative Invadopodia properties were collected in an automated fashion.

We expect that the software system described here will be applicable to quantifying invadopodia structures being studied with other fluorescently tagged Invaodpodia proteins, such as Tks5 or cortactin, as well. Invadopodia proteins would need to be fluorescently tagged and be present at invadopodia during the degradation process in order to be assessed using our system. Many of these alternative tags should more reliably mark Invadopodia than the

LifeAct F-actin label used to develop the analysis system, making the single F-actin puncta classification steps outlined above less important. The cell population analysis system could also be adapted to use alternative markers cell markers such as dyes or membrane associated fluorescent markers. The analysis could also be improved by the addition of a nucleus marker, making it possible to reliably split cell clumps using a watershed segmentation. In addition to alternative Invadopodia markers or cell markers, it should also be possible to adapt the ECM quantification methods to different labeling methodologies such as dye-quenched gelatins.

The software to process the labeled puncta in single cells and in cell populations through time will be released as open source packages available through the Gomez lab website (http://gomezlab.bme.unc.edu/). In addition, the single cell analysis of individual puncta will be available on the web (http://ias.bme.unc.edu/). This website does not require the user to download or install any software to process a set of invadopodia images. These two complementary analysis systems allow the quantification of Invadopodia behavior at the single Invadopodia and single cell levels. These two analysis systems could also be readily adapted to work in the context of a high-content time-lapse screen.

Chapter 5

Conclusions and Future Directions

The analysis of FA and Invadopodia structures using Bioimage Informatic methods provide benefits over manual methods of quantifying these structures in living cells. These benefits include comprehensive, unbiased and repeatable measurment of FA and Invadopodia properties. In Chapter 2, a set of high-content image analysis approaches were described, which make it possible to identify, track and quantify properties of FA in motile cells. These methods were expanded in Chapter 3 to develop methods to locate FAs in the several cell regions and analyze the effect of Arp2/3 depletion on global FA alignment. The high-content image analysis approaches described in Chapters 2 and 3 for quantifying FA properties have expanded the number and type of properties that can be collected from FA image sets. In Chapter 4, a framework for quantification of single Invadopodia and populations of invasive cells in an *in vitro* assay was presented. These quantitative analysis methods make it possible to automatically extract the properties of single Invadopodia from time-lapse image sets and of cell population level ECM degradation. Both of these projects have resulted in publicly available open source software, which the FA and Invadopodia communittees can use to quantify new image sets. In addition, two web-based tools have been developed to allow users to use the FA and Invadopodia analysis methods without software installation.

5.1 Future Directions

5.2 Focal Adhesion Analysis

The FA analysis methods could be expanded in several ways. These improvements and additions are driven by developments in methods for probing the FA structures themselves and the protein signalling networks related to FA. Possible areas of future work involve adapting the analysis methods to FA images gathered using new methodologies, better relating FA structures to the spatial environment and integration of information about the signalling network that control FA development.

The current methods for segmentation of FA are tailored to the analysis of TIRF images, but this is not the only imaging methodology that can capture FA dynamics. Epifluorescence imaging is a simpler and more widely available imaging methodology, which can be used to observe FA dynamics. Compared with TIRF imaging, epifluorescence images suffer from lower signal to noise ratios and a higher likelyhood of fluorophore photobleaching. Extensions to the FA analysis software could alleviate these issues through additional filtering and application of photobleaching corrections. Confocal imaging can be used to gather FA image sets, increasing the spatial resolution at the cost of typically lower signal to noise ratios. I have attempted to analyze two sets of confocal FA images and developed some extensions to the segmentation methods to deal with the properties of confocal images, but these extensions need to be verified and tested using more FA image sets. The development of high-resolution imaging methodologies, such as 3D-SIM [105], STED [106] and PALM [107], have made it possible to gather biological images at higher resolution than the diffraction limit of standard microscopy. PALM has already been used to study the spacial organization of fixed FA complexes in remarkable detail [108]. If high-resolution methods can be adapted to work in migrating cells, it would be possible to dynamically observe the recruitment and localization of FA proteins to different portions of developing FA complexes. Since the methods described here treat each FA as essentially a globular object, without internal features, expand-

ing the software to deal with a dynamic variegated FA substructure would be an interesting and worthwhile challenge.

FA are inherently three dimensional structures, but the methods described in this thesis are tailored towards treating FA as two dimensional globular objects. This focus on two dimensions is a product of two dimensional imaging being the only readily available method for measuring FA dynamics. Assuming the signal to noise and resolution issues associated with measuring FA structures in three dimensions could be overcome, the methods described here could be readily adapted to work in three dimensions. The minimum-size watershed segmentation method can be adapted to work in three dimensions, as can the object overlap and centroid distance tracking methods. One significant issue that would need to be solved would be dealing with volume of data produced by three dimensional imaging methods. The Arp2/3 depletion results presented in Chapter 3, required the analysis of 272 time-lapse image sets, which would have taken approximately 2.5 days to process on the FA analysis server, assuming no other processing jobs were being run and all detection parameters were already determined. If the third dimension was added to these image sets, with 10 Z-sections per image set, the amount of hard drive and processing time would in turn be expected to by nearly a factor of 10. These issues would be need to be addressed by identification of the processing bottlenecks and development of either more efficient algorithms or conversion of the existing methods to faster implementations.

In addition to expanding the range of imaging methods that could be used with the FA analysis software, there are several types of FA properties which might help to quantify FA behavior. One area deals with with quantifying the FA spatial properties. The internal environment of the cell is highly varied with different areas within the cell experiencing a range of internal and external signals. These signals must be converted through signalling pathways to FA behavior which varies on a spatial scale, but the tools developed here only use gross morphological distinctions, such as leading or trailing, to subdivide FA analysis in a spatial manner. More sophisticated spatial clustering methods, such as K-means or hierar-

chical, could possibly discern local cellular regions where FA dynamics are being perturbed compared to the rest of the cell. Integration of these methods with either spatial activation of specific signalling cascades, such as a recently described photoactivatable RAC [109], or exposure to controlled spatial gradients of signalling molecules could help to clarify fundamental aspects of cell migration.

The FA analysis software could also be expanded to integrate the analysis of other dynamic intracellular signals. One source for gathering additional signals are biosensors that have been developed to quantify intracellular protein activity levels. The location and development of FA could be used as a marker to link biosensor activity levels across multiple experiments, analogous to how the biosensors developed in the Hahn lab were analyzed using the motion of the cell edge to link the activity of biosensors across experiments [28].

5.3 Invadopodia Analysis

The Invadopodia analysis methods are not as developed as the FA analysis methods, leaving many areas for potential improvement. Much like the FA analysis methods dependence on TIRF imaging and the associated high signal to noise ratio, the current Invadopodia analysis implementation is somewhat dependent on the LifeAct-GFP marker used to follow the puncta. If image sets tracking other invadopodia markers, such as Tsk5 or Cortactin, were collected, the existing segmentation methods could be modified to follow these markers thorough time. In addition to alternative markers, the analysis methods could also be adapted to use different ECM markers. One alternative marker of ECM degradation uses ECM labeled with a fluorescent dye that only becomes visible once degradation has occurred. This marker has the opposite behavior of the fluorescent ECM used in the current assay, so significant changes would need to be made in how assess the degradation.

Finally, with both the FA and Invadopodia analysis tools in place, a logical next step would be combine the two analysis methods to simultaneously quantify the behavior of Invadopodia and FA. The first obstacle in combining the two assays comes in gathering images of FA,

Invadopodia and the corresponding labled ECM simultaneously. Running such an assay with probes for all three needed markers, while maintaining the needed resolution and signal to noise ratio to use the current analysis systems, is challenging. If the technical barriers could be overcome, the FA and Invadopodia analysis could be combined to elucidate the complicated balance between cell motility and ECM degradation.

Bibliography

[1] B. N. G. Giepmans, S. R. Adams, M. H. Ellisman, and R. Y. Tsien, "The fluorescent toolbox for assessing protein location and function," *Science*, vol. 312, pp. 217–224, Apr. 2006. 1

[2] N. C. Shaner, P. A. Steinbach, and R. Y. Tsien, "A guide to choosing fluorescent proteins," *Nat Meth*, vol. 2, pp. 905–909, Dec. 2005. 1

[3] H. Peng, "Bioimage informatics: a new area of engineering biology," *Bioinformatics*, vol. 24, pp. 1827–1836, Sept. 2008. 1

[4] G. Danuser, "Computer vision in cell biology," *Cell*, vol. 147, pp. 973–978, Nov. 2011. 2

[5] A. Carpenter, T. Jones, M. Lamprecht, C. Clarke, I. Kang, O. Friman, D. Guertin, J. Chang, R. Lindquist, J. Moffat, P. Golland, and D. Sabatini, "Cellprofiler: image analysis software for identifying and quantifying cell phenotypes," *Genome Biology*, vol. 7, no. 10, p. R100, 2006. 2, 5

[6] A. Shariff, J. Kangas, L. P. Coelho, S. Quinn, and R. F. Murphy, "Automated image analysis for high-content screening and analysis," *Journal of Biomolecular Screening*, vol. 15, pp. 726–734, Aug. 2010. 2

[7] D. L. G. Hill, P. G. Batchelor, M. Holden, and D. J. Hawkes, "Medical image registration," *Physics in Medicine and Biology*, vol. 46, no. 3, pp. R1–, 2001. 3

[8] E. Zamir, B. Katz, S. Aota, K. Yamada, B. Geiger, and Z. Kam, "Molecular diversity of cell-matrix adhesions," *J Cell Sci*, vol. 112, no. 11, pp. 1655–1669, 1999. 3, 25

[9] A. Matov, K. Applegate, P. Kumar, C. Thoma, W. Krek, G. Danuser, and T. Wittmann, "Analysis of microtubule dynamic instability using a plus-end growth marker," *Nature Methods*, vol. 7, pp. 761–768, Sept. 2010. 3, 7, 73

[10] N. Otsu, "A threshold selection method from gray-level histograms," *Systems, Man and Cybernetics, IEEE Transactions on*, vol. 9, no. 1, pp. 62–66, 1979. 3

[11] P. L. Rosin, "Unimodal thresholding," *Pattern Recognition*, vol. 34, pp. 2083–2096, Nov. 2001. 3

[12] E. Meijering, I. Smal, and G. Danuser, "Tracking in molecular bioimaging," *Signal Processing Magazine, IEEE*, vol. 23, no. 3, pp. 46–53, 2006. 3

[13] K. Jaqaman, D. Loerke, M. Mettlen, H. Kuwata, S. Grinstein, S. L. Schmid, and G. Danuser, "Robust single-particle tracking in live-cell time-lapse sequences," *Nat Meth*, vol. 5, no. 8, pp. 695–702, 2008. 4

[14] G. Yang, A. Matov, and G. Danuser, "Reliable tracking of large scale dense antiparallel particle motion for fluorescence live cell imaging," in *Computer Vision and Pattern Recognition - Workshops, 2005. CVPR Workshops. IEEE Computer Society Conference on*, pp. 138–138, 2005. 4

[15] A. E. Carpenter, "Image-based chemical screening," *Nat Chem Biol*, vol. 3, pp. 461–465, 08 2007. 4

[16] T. R. Jones, A. E. Carpenter, M. R. Lamprecht, J. Moffat, S. J. Silver, J. K. Grenier, A. B. Castoreno, U. S. Eggert, D. E. Root, P. Golland, and D. M. Sabatini, "Scoring diverse cellular morphologies in image-based screens with iterative feedback and machine learning," *Proceedings of the National Academy of Sciences*, vol. 106, pp. 1826–1831, 02 2009. 5

[17] T. Jones, I. Kang, D. Wheeler, R. Lindquist, A. Papallo, D. Sabatini, P. Golland, and A. Carpenter, "Cellprofiler analyst: data exploration and analysis software for complex image-based screens," *BMC Bioinformatics*, vol. 9, no. 1, pp. 482–, 2008. 5

[18] C. Wahlby, L. Kamentsky, Z. H. Liu, T. Riklin-Raviv, A. L. Conery, E. J. O'Rourke, K. L. Sokolnicki, O. Visvikis, V. Ljosa, J. E. Irazoqui, P. Golland, G. Ruvkun, F. M. Ausubel, and A. E. Carpenter, "An image analysis toolbox for high-throughput c. elegans assays," *Nat Meth*, vol. 9, pp. 714–716, July 2012. 5

[19] C. Bakal, J. Aach, G. Church, and N. Perrimon, "Quantitative Morphological Signatures Define Local Signaling Networks Regulating Cell Morphology," *Science*, vol. 316, no. 5832, pp. 1753–1756, 2007. 5

[20] J. L. Rohn, D. Sims, T. Liu, M. Fedorova, F. Schck, J. Dopie, M. K. Vartiainen, A. A. Kiger, N. Perrimon, and B. Baum, "Comparative rnai screening identifies a conserved core metazoan actinome by phenotype," *The Journal of Cell Biology*, vol. 194, pp. 789–805, Sept. 2011. 5

[21] Y. Paran, M. Ilan, Y. Kashman, S. Goldstein, Y. Liron, B. Geiger, and Z. Kam, "High-throughput screening of cellular features using high-resolution light-microscopy; application for profiling drug effects on cell adhesion," *Journal of Structural Biology*, vol. 158, no. 2, pp. 233–243, 2007. 5, 10

[22] S. E. Winograd-Katz, S. Itzkovitz, Z. Kam, and B. Geiger, "Multiparametric analysis of focal adhesion formation by rnai-mediated gene knockdown," *J. Cell Biol.*, vol. 186, pp. 423–436, Aug. 2009. 5, 10, 45

[23] M. Quintavalle, L. Elia, J. H. Price, S. Heynen-Genel, and S. A. Courtneidge, "A cell-based high-content screening assay reveals activators and inhibitors of cancer cell invasion," *Sci. Signal.*, vol. 4, pp. ra49–, July 2011. 5, 72

[24] E. M. Gardiner, K. N. Pestonjamasp, B. P. Bohl, C. Chamberlain, K. M. Hahn, and G. M. Bokoch, "Spatial and temporal analysis of rac activation during live neutrophil chemotaxis," *Current Biology*, vol. 12, pp. 2029–2034, Dec. 2002. 6

[25] O. Pertz, L. Hodgson, R. L. Klemke, and K. M. Hahn, "Spatiotemporal dynamics of rhoa activity in migrating cells," *Nature*, vol. 440, no. 7087, pp. 1069–1072, 2006. 6

[26] P. Nalbant, L. Hodgson, V. Kraynov, A. Toutchkine, and K. M. Hahn, "Activation of endogenous cdc42 visualized in living cells," *Science*, vol. 305, pp. 1615–1619, Sept. 2004. 6

[27] M. Machacek and G. Danuser, "Morphodynamic Profiling of Protrusion Phenotypes," *Biophys. J.*, vol. 90, no. 4, pp. 1439–1452, 2006. 6, 26, 73

[28] M. Machacek, L. Hodgson, C. Welch, H. Elliott, O. Pertz, P. Nalbant, A. Abell, G. L. Johnson, K. M. Hahn, and G. Danuser, "Coordination of rho gtpase activities during cell protrusion," *Nature*, vol. 461, pp. 99–103, Sept. 2009. 6, 88

[29] T. J. Mitchison and E. D. Salmon, "Mitosis: a history of division," *Nat Cell Biol*, vol. 3, pp. E17–E21, Jan. 2001. 7

[30] K. Hirschberg, C. M. Miller, J. Ellenberg, J. F. Presley, E. D. Siggia, R. D. Phair, and J. Lippincott-Schwartz, "Kinetic analysis of secretory protein traffic and characterization of golgi to plasma membrane transport intermediates in living cells," *The Journal of Cell Biology*, vol. 143, pp. 1485–1503, Dec. 1998. 7

[31] C. J. Merrifield, D. Perrais, and D. Zenisek, "Coupling between clathrin-coated-pit invagination, cortactin recruitment, and membrane scission observed in live cells," *Cell*, vol. 121, pp. 593–606, May 2005. 7

[32] D. Loerke, M. Mettlen, D. Yarar, K. Jaqaman, H. Jaqaman, G. Danuser, and S. L. Schmid, "Cargo and dynamin regulate clathrin-coated pit maturation," *PLoS Biology*, vol. 7, 3 2009. 7

[33] B. Geiger, J. P. Spatz, and A. D. Bershadsky, "Environmental sensing through focal adhesions," *Nat Rev Mol Cell Biol*, vol. 10, pp. 21–33, Jan. 2009. 9

[34] D. Lauffenburger and A. Horwitz, "Cell migration: a physically integrated molecular process.," *Cell*, vol. 84, no. 3, pp. 359–69, 1996. 9

[35] A. Ridley, M. Schwartz, K. Burridge, R. Firtel, M. Ginsberg, G. Borisy, J. Parsons, and A. Horwitz, "Cell migration: Integrating signals from front to back," *Science*, vol. 302, no. 5651, pp. 1704–1709, 2003. 9, 47

[36] M. Larsen, M. L. Tremblay, and K. M. Yamada, "Phosphatases in cell-matrix adhesion and migration," *Nat Rev Mol Cell Biol*, vol. 4, pp. 700–711, Sept. 2003. 9

[37] D. J. Webb, J. T. Parsons, and A. F. Horwitz, "Adhesion assembly, disassembly and turnover in migrating cells - over and over and over again," *Nat Cell Biol*, vol. 4, no. 4, pp. E97–E100, 2002. 9, 52

[38] C. Ballestrem, B. Hinz, B. A. Imhof, and B. Wehrle-Haller, "Marching at the front and dragging behind: differential v3-integrin turnover regulates focal adhesion behavior," *The Journal of Cell Biology*, vol. 155, pp. 1319–1332, Dec. 2001. 9

[39] D. Webb, K. Donais, L. Whitmore, S. Thomas, C. Turner, J. Parsons, and A. Horwitz, "Fak–src signalling through paxillin, erk and mlck regulates adhesion disassembly," *Nature Cell Biology*, vol. 6, no. 2, pp. 154–161, 2004. 9, 13, 29, 43, 66

[40] A. Nayal, D. J. Webb, C. M. Brown, E. M. Schaefer, M. Vicente-Manzanares, and A. R. Horwitz, "Paxillin phosphorylation at ser273 localizes a git1-pix-pak complex and regulates adhesion and protrusion dynamics," *The Journal of Cell Biology*, vol. 173, pp. 587–589, 5 2006. 9

[41] N. S. Bryce, E. S. Clark, J. L. Leysath, J. D. Currie, D. J. Webb, and A. M. Weaver, "Cortactin promotes cell motility by enhancing lamellipodial persistence," *Curr Biol*, vol. 15, pp. 1276–1285, July 2005. 9, 20

[42] A. L. Mattheyses, S. M. Simon, and J. Z. Rappoport, "Imaging with total internal reflection fluorescence microscopy for the cell biologist," *Journal of Cell Science*, vol. 123, pp. 3621–3628, Nov. 2010. 9

[43] K. A. Owen, F. J. Pixley, K. S. Thomas, M. Vicente-Manzanares, B. J. Ray, A. F. Horwitz, J. T. Parsons, H. E. Beggs, E. R. Stanley, and A. H. Bouton, "Regulation of lamellipodial persistence, adhesion turnover, and motility in macrophages by focal adhesion kinase," *J. Cell Biol.*, p. jcb.200708093, 2007. 9

[44] T. Kobayashi, S.-i. Hino, N. Oue, T. Asahara, M. Zollo, W. Yasui, and A. Kikuchi, "Glycogen synthase kinase 3 and h-prune regulate cell migration by modulating focal adhesions," *Molecular and Cellular Biology*, vol. 26, no. 3, pp. 898–911, February 1, 2006. 9

[45] S. J. Franco, M. A. Rodgers, B. J. Perrin, J. Han, D. A. Bennin, D. R. Critchley, and A. Huttenlocher, "Calpain-mediated proteolysis of talin regulates adhesion dynamics," *Nat Cell Biol*, vol. 6, no. 10, pp. 977–983, 2004. 9

[46] E. Zamir, B. Geiger, and Z. Kam, "Quantitative multicolor compositional imaging resolves molecular domains in cell-matrix adhesions," *PLoS ONE*, vol. 3, p. e1901, Apr 2008. 10

[47] M. C. Brown and C. E. Turner, "Paxillin: Adapting to change," *Physiological Reviews*, vol. 84, pp. 1315–1339, 10 2004. 10

[48] R. Zaidel-Bar, C. Ballestrem, Z. Kam, and B. Geiger, "Early molecular events in the assembly of matrix adhesions at the leading edge of migrating cells," *Journal of Cell Science*, vol. 116, no. 22, pp. 4605–4613, 2003. 18

[49] R. Zaidel-Bar, M. Cohen, L. Addadi, and B. Geiger, "Hierarchical assembly of cell-matrix adhesion complexes," *Biochem. Soc. Trans*, vol. 32, pp. 416–420, 2004. 18

[50] C. Huang, Z. Rajfur, C. Borchers, M. D. Schaller, and K. Jacobson, "Jnk phosphorylates paxillin and regulates cell migration," *Nature*, vol. 424, no. 6945, pp. 219–223, 2003. 20, 24, 42

[51] K. Kimura, S. Teranishi, J. Yamauchi, and T. Nishida, "Role of jnk-dependent serine phosphorylation of paxillin in migration of corneal epithelial cells during wound closure," *Investigative Ophthalmology Visual Science*, vol. 49, pp. 125–132, 1 2008/1/1. 20

[52] Z. Huang, D.-P. Yan, and B.-X. Ge, "Jnk regulates cell migration through promotion of tyrosine phosphorylation of paxillin," *Cellular Signalling*, vol. 20, no. 11, pp. 2002–2012, 2008. 20

[53] C. Huang, K. Jacobson, and M. Schaller, "A role for jnk-paxillin signaling in cell migration.," *Cell cycle*, vol. 3, no. 1, p. 4, 2004. 24

[54] Z. Rajfur, P. Roy, C. Otey, L. Romer, and K. Jacobson, "Dissecting the link between stress fibres and focal adhesions by cali with egfp fusion proteins," *Nat Cell Biol*, vol. 4, pp. 286–293, Apr. 2002. 24

[55] L. Ji and G. Danuser, "Tracking quasi-stationary flow of weak fluorescent signals by adaptive multi-frame correlation," *Journal of Microscopy*, vol. 220, no. 3, pp. 150–167, 2005. 26

[56] P. Vallotton, S. L. Gupton, C. M. Waterman-Storer, and G. Danuser, "Simultaneous mapping of filamentous actin flow and turnover in migrating cells by quantitative fluorescent speckle microscopy," *PNAS*, vol. 101, no. 26, pp. 9660–9665, 2004. 44

[57] D. T. Burnette, S. Manley, P. Sengupta, R. Sougrat, M. W. Davidson, B. Kachar, and J. Lippincott-Schwartz, "A role for actin arcs in the leading-edge advance of migrating cells," *Nat Cell Biol*, vol. 13, pp. 371–382, Apr. 2011. 44

[58] C. M. Franz, G. E. Jones, and A. J. Ridley, "Cell migration in development and disease," *Developmental Cell*, vol. 2, pp. 153–158, Feb. 2002. 47

[59] P. L. Schwartzberg, A. M. Stall, J. D. Hardin, K. S. Bowdish, T. Humaran, S. Boast, M. L. Harbison, E. J. Robertson, and S. P. Goff, "Mice homozygous for the ablm1 mutation show poor viability and depletion of selected b and t cell populations," *Cell*, vol. 65, pp. 1165–1175, June 1991. 47

[60] B. Li, S. Boast, K. de los Santos, I. Schieren, M. Quiroz, S. L. Teitelbaum, M. M Tondravi, and S. P. Goff, "Mice deficient in abl are osteoporotic and have defects in osteoblast maturation," *Nat Genet*, vol. 24, pp. 304–308, Mar. 2000. 47

[61] V. L. Tybulewicz, C. E. Crawford, P. K. Jackson, R. T. Bronson, and R. C. Mulligan, "Neonatal lethality and lymphopenia in mice with a homozygous disruption of the c-abl proto-oncogene," *Cell*, vol. 65, pp. 1153–1163, June 1991. 47

[62] J. Zhu and J. Y. Wang, "Death by abl: A matter of location," *Current Topics in Developmental Biology*, vol. Volume 59, pp. 165–192, 2004. 47

[63] W. D. Bradley and A. J. Koleske, "Regulation of cell migration and morphogenesis by abl-family kinases: emerging mechanisms and physiological contexts," *Journal of Cell Science*, vol. 122, pp. 3441–3454, Oct. 2009. 47

[64] P. J. Woodring, T. Hunter, and J. Y. J. Wang, "Regulation of f-actin-dependent processes by the abl family of tyrosine kinases," *Journal of Cell Science*, vol. 116, pp. 2613–2626, July 2003. 47

[65] T. Stradal, K. D. Courtney, K. Rottner, P. Hahne, J. Small, and A. M. Pendergast, "The abl interactor proteins localize to sites of actin polymerization at the tips of lamellipodia and filopodia," *Curr Biol*, vol. 11, pp. 891–895, June 2001. 47

[66] P. J. Woodring, J. Meisenhelder, S. A. Johnson, G.-L. Zhou, J. Field, K. Shah, F. Bladt, T. Pawson, M. Niki, P. P. Pandolfi, J. Y. Wang, and T. Hunter, "c-abl phosphorylates dok1 to promote filopodia during cell spreading," *The Journal of Cell Biology*, vol. 165, pp. 493–503, May 2004. 47

[67] V. Radha, A. Rajanna, A. Mitra, N. Rangaraj, and G. Swarup, "C3g is required for c-abl-induced filopodia and its overexpression promotes filopodia formation," *Experimental Cell Research*, vol. 313, pp. 2476–2492, July 2007. 47

[68] K. H. Kain and R. L. Klemke, "Inhibition of cell migration by abl family tyrosine kinases through uncoupling of crk-cas complexes," *Journal of Biological Chemistry*, vol. 276, pp. 16185–16192, May 2001. 47

[69] H. Jin and J. Y. Wang, "Abl tyrosine kinase promotes dorsal ruffles but restrains lamellipodia extension during cell spreading on fibronectin," *Molecular Biology of the Cell*, vol. 18, pp. 4143–4154, Oct. 2007. 47

[70] P. J. Woodring, E. D. Litwack, D. D. O'Leary, G. R. Lucero, J. Y. Wang, and T. Hunter, "Modulation of the f-actin cytoskeleton by c-abl tyrosine kinase in cell spreading and neurite extension," *The Journal of Cell Biology*, vol. 156, pp. 879–892, Mar. 2002. 47

[71] J. G. Peacock, B. A. Couch, and A. J. Koleske, "The abl and arg non-receptor tyrosine kinases regulate different zones of stress fiber, focal adhesion, and contractile network localization in spreading fibroblasts," *Cytoskeleton*, vol. 67, pp. 666–675, Oct. 2010. 47

[72] R. Li and A. Pendergast, "Arg kinase regulates epithelial cell polarity by targeting 1-integrin and small gtpase pathways," *Current Biology*, vol. 21, pp. 1534–1542, Sept. 2011. 47

[73] K. F. Swaney, C.-H. Huang, and P. N. Devreotes, "Eukaryotic chemotaxis: A network of signaling pathways controls motility, directional sensing, and polarity," *Annu. Rev. Biophys.*, vol. 39, pp. 265–289, Apr. 2010. 52

[74] C. A. Parent, "Making all the right moves: chemotaxis in neutrophils and dictyostelium," *Current Opinion in Cell Biology*, vol. 16, pp. 4–13, Feb. 2004. 52

[75] J. P. Thiery, "Mechanisms of cell migration in the vertebrate embryo," *Cell differentiation*, vol. 15, no. 1, pp. 1–15, 1984. 52

[76] T. Wynn, "Cellular and molecular mechanisms of fibrosis," *J. Pathol.*, vol. 214, pp. 199–210, Jan. 2008. 52

[77] T. M. Svitkina and G. G. Borisy, "Arp2/3 complex and actin depolymerizing factor/cofilin in dendritic organization and treadmilling of actin filament array in lamellipodia," *The Journal of Cell Biology*, vol. 145, pp. 1009–1026, May 1999. 52, 53

[78] T. D. Pollard and G. G. Borisy, "Cellular motility driven by assembly and disassembly of actin filaments," *Cell*, vol. 112, pp. 453–465, Feb. 2003. 52

[79] E. D. Goley and M. D. Welch, "The arp2/3 complex: an actin nucleator comes of age," *Nat Rev Mol Cell Biol*, vol. 7, pp. 713–726, Oct. 2006. 53

[80] L. Cai, A. M. Makhov, D. A. Schafer, and J. E. Bear, "Coronin 1b antagonizes cortactin and remodels arp2/3-containing actin branches in lamellipodia," *Cell*, vol. 134, no. 5, pp. 828–842, 2008. 53

[81] S. M. Nicholson-Dykstra and H. N. Higgs, "Arp2 depletion inhibits sheet-like protrusions but not linear protrusions of fibroblasts and lymphocytes," *Cell Motil. Cytoskeleton*, vol. 65, pp. 904–922, Nov. 2008. 53

[82] S. L. Rogers, U. Wiedemann, N. Stuurman, and R. D. Vale, "Molecular requirements for actin-based lamella formation in drosophila s2 cells," *The Journal of Cell Biology*, vol. 162, pp. 1079–1088, Sept. 2003. 53

[83] A. Steffen, J. Faix, G. P. Resch, J. Linkner, J. Wehland, J. V. Small, K. Rottner, and T. E. Stradal, "Filopodia formation in the absence of functional wave- and arp2/3-complexes," *Molecular Biology of the Cell*, vol. 17, pp. 2581–2591, June 2006. 53

[84] A. Di Nardo, G. Cicchetti, H. Falet, J. H. Hartwig, T. P. Stossel, and D. J. Kwiatkowski, "Arp2/3 complex-deficient mouse fibroblasts are viable and have normal leading-edge actin structure and function," *Proceedings of the National Academy of Sciences of the United States of America*, vol. 102, pp. 16263–16268, Nov. 2005. 53

[85] E. Urban, S. Jacob, M. Nemethova, G. P. Resch, and J. V. Small, "Electron tomography reveals unbranched networks of actin filaments in lamellipodia," *Nat Cell Biol*, vol. 12, pp. 429–435, May 2010. 53

[86] E. Schwob and R. P. Martin, "New yeast actin-like gene required late in the cell cycle," *Nature*, vol. 355, pp. 179–182, Jan. 1992. 53

[87] K. Yae, V. W. Keng, M. Koike, K. Yusa, M. Kouno, Y. Uno, G. Kondoh, T. Gotow, Y. Uchiyama, K. Horie, and J. Takeda, "Sleeping beauty transposon-based phenotypic analysis of mice: Lack of arpc3 results in defective trophoblast outgrowth," *Molecular and Cellular Biology*, vol. 26, no. 16, pp. 6185–6196, August 15, 2006. 53

[88] M. Zaki, J. King, K. Futterer, and R. Insall, "Replacement of the essential dictyostelium arp2 gene by its entamoeba homologue using parasexual genetics," *BMC Genetics*, vol. 8, no. 1, pp. 28–, 2007. 53

[89] T. D. Pollard and J. A. Cooper, "Actin, a central player in cell shape and movement," *Science*, vol. 326, pp. 1208–1212, Nov. 2009. 53

[90] B. J. Nolen, N. Tomasevic, A. Russell, D. W. Pierce, Z. Jia, C. D. McCormick, J. Hartman, R. Sakowicz, and T. D. Pollard, "Characterization of two classes of small molecule inhibitors of arp2/3 complex," *Nature*, vol. 460, pp. 1031–1034, Aug. 2009. 53

[91] P. A. DiMilla, J. A. Stone, J. A. Quinn, S. M. Albelda, and D. A. Lauffenburger, "Maximal migration of human smooth muscle cells on fibronectin and type iv collagen occurs at an intermediate attachment strength," *The Journal of cell biology*, vol. 122, no. 3, pp. 729–737, 1993. 54

[92] S. L. Gupton and C. M. Waterman-Storer, "Spatiotemporal feedback between actomyosin and focal-adhesion systems optimizes rapid cell migration," *Cell*, vol. 125, no. 7, pp. 1361–1374, 2006. 54

[93] M. E. Berginski, E. A. Vitriol, K. M. Hahn, and S. M. Gomez, "High-resolution quantification of focal adhesion spatiotemporal dynamics in living cells," *PLoS ONE*, vol. 6, pp. e22025–, July 2011. 56, 60, 66

[94] C. A. Schneider, W. S. Rasband, and K. W. Eliceiri, "Nih image to imagej: 25 years of image analysis," *Nat Meth*, vol. 9, pp. 671–675, July 2012. 65

[95] K. Shen, C. E. Tolbert, C. Guilluy, V. S. Swaminathan, M. E. Berginski, K. Burridge, R. Superfine, and S. L. Campbell, "The vinculin c-terminal hairpin mediates f-actin bundle formation, focal adhesion, and cell mechanical properties," *Journal of Biological Chemistry*, vol. 286, pp. 45103–45115, Dec. 2011. 66

[96] C. Wu, S. Asokan, M. Berginski, E. Haynes, N. Sharpless, J. Griffith, S. Gomez, and J. Bear, "Arp2/3 is critical for lamellipodia and response to extracellular matrix cues but is dispensable for chemotaxis," *Cell*, vol. 148, pp. 973–987, Mar. 2012. 66, 73

[97] Z. Chen, E. Lessey, M. E. Berginski, L. Cao, J. Li, X. Trepat, M. Itano, S. M. Gomez, M. Kapustina, C. Huang, K. Burridge, G. Truskey, and K. Jacobson, "Gleevec, an abl family inhibitor, produces a profound change in cell shape and migration," *PLoS ONE*, vol. 8, pp. e52233–, Jan. 2013. 66

[98] C. L. Chaffer and R. A. Weinberg, "A perspective on cancer cell metastasis," *Science*, vol. 331, pp. 1559–1564, Mar. 2011. 70

[99] I. Ayala, M. Baldassarre, G. Caldieri, and R. Buccione, "Invadopodia: A guided tour," *European Journal of Cell Biology*, vol. 85, pp. 159–164, Apr. 2006. 70

[100] V. V. Artym, K. M. Yamada, and S. C. Mueller, "Ecm degradation assays for analyzing local cell invasion," in *Methods in Molecular Biology* (S. Even-Ram and V. Artym, eds.), vol. 522, pp. 211–219–, Humana Press, 2009. 70, 82

[101] V. V. Artym, Y. Zhang, F. Seillier-Moiseiwitsch, K. M. Yamada, and S. C. Mueller, "Dynamic interactions of cortactin and membrane type 1 matrix metalloproteinase at invadopodia: Defining the stages of invadopodia formation and function," *Cancer Res*, vol. 66, pp. 3034–3043, Mar. 2006. 70

[102] M. Oser and J. Condeelis, "The cofilin activity cycle in lamellipodia and invadopodia," *J. Cell. Biochem.*, vol. 108, no. 6, pp. 1252–1262, 2009. 70

[103] C. Albiges-Rizo, O. Destaing, B. Fourcade, E. Planus, and M. R. Block, "Actin machinery and mechanosensitivity in invadopodia, podosomes and focal adhesions," *J Cell Sci*, vol. 122, pp. 3037–3049, Sept. 2009. 70

[104] J. Riedl, A. H. Crevenna, K. Kessenbrock, J. H. Yu, D. Neukirchen, M. Bista, F. Bradke, D. Jenne, T. A. Holak, Z. Werb, M. Sixt, and R. Wedlich-Soldner, "Lifeact: a versatile marker to visualize f-actin," *Nat Meth*, vol. 5, pp. 605–607, July 2008. 71

[105] M. G. Gustafsson, L. Shao, P. M. Carlton, C. R. Wang, I. N. Golubovskaya, W. Z. Cande, D. A. Agard, and J. W. Sedat, "Three-dimensional resolution doubling in wide-field fluorescence microscopy by structured illumination," *Biophysical Journal*, vol. 94, no. 12, pp. 4957–, 2008. 86

[106] T. A. Klar, S. Jakobs, M. Dyba, A. Egner, and S. W. Hell, "Fluorescence microscopy with diffraction resolution barrier broken by stimulated emission," *Proceedings of the National Academy of Sciences*, vol. 97, pp. 8206–8210, July 2000. 86

[107] E. Betzig, G. H. Patterson, R. Sougrat, O. W. Lindwasser, S. Olenych, J. S. Bonifacino, M. W. Davidson, J. Lippincott-Schwartz, and H. F. Hess, "Imaging intracellular fluorescent proteins at nanometer resolution," *Science*, vol. 313, pp. 1642–1645, Sept. 2006. 86

[108] P. Kanchanawong, G. Shtengel, A. M. Pasapera, E. B. Ramko, M. W. Davidson, H. F. Hess, and C. M. Waterman, "Nanoscale architecture of integrin-based cell adhesions," *Nature*, vol. 468, pp. 580–584, Nov. 2010. 86

[109] Y. I. Wu, D. Frey, O. I. Lungu, A. Jaehrig, I. Schlichting, B. Kuhlman, and K. M. Hahn, "A genetically encoded photoactivatable rac controls the motility of living cells," *Nature*, vol. 461, pp. 104–108, Sept. 2009. 88